Tailoring the mesoscopic structure and orientation of semicrystalline and liquid-crystalline polymers : from 1D- to 2D-confinement

Yaroslav Odarchenko

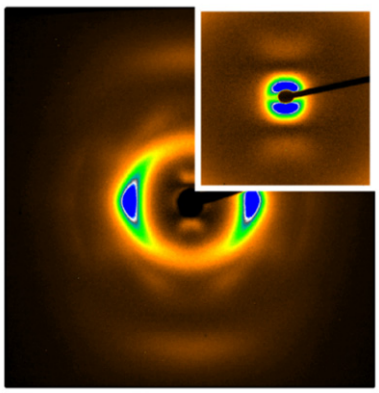

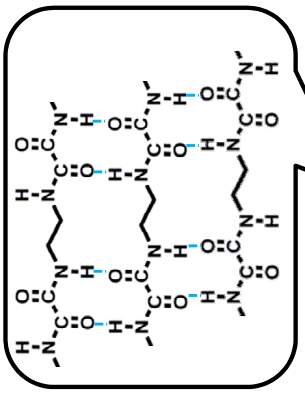

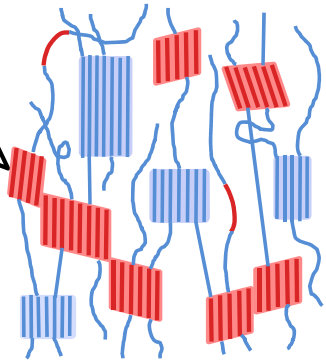

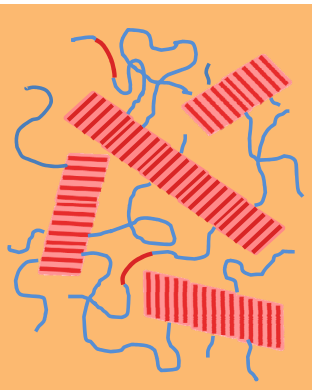

TAILORING THE MESOSCOPIC STRUCTURE AND ORIENTATION OF SEMICRYSTALLINE AND LIQUID-CRYSTALLINE POLYMERS: FROM 1D TO 2D CONFINEMENT

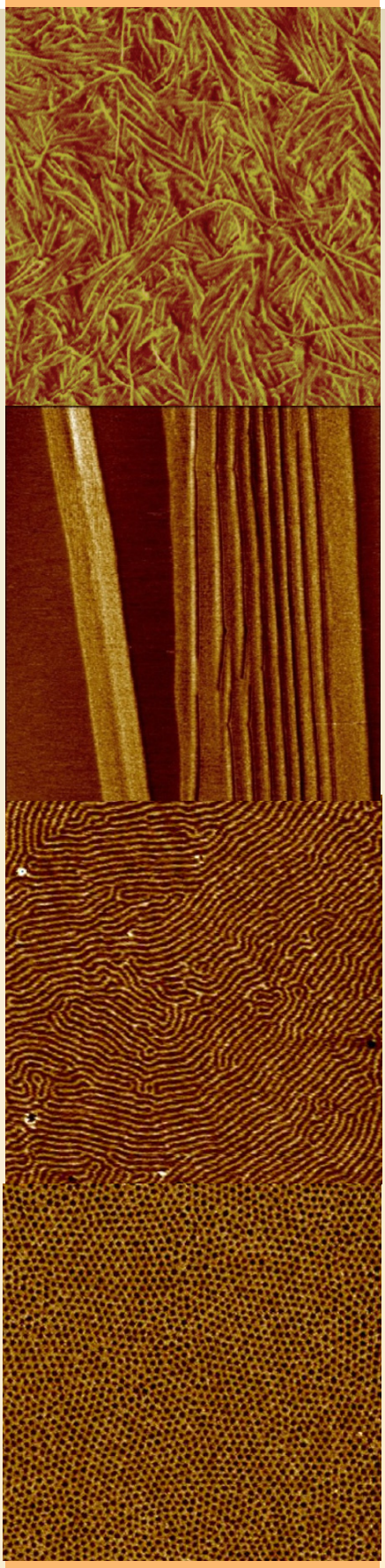

Yaroslav Odarchenko

2012

TAILORING THE MESOSCOPIC STRUCTURE AND ORIENTATION OF SEMICRYSTALLINE AND LIQUID-CRYSTALLINE POLYMERS: FROM 1D TO 2D CONFINEMENT

by
Yaroslav Odarchenko

B.S., Applied Physics and Mathematics, 2007
M.S., Applied Physics and Mathematics, 2009
Moscow Institute of Physics and Technology (State University), Moscow,
The Russian Federation

Dissertation Submitted to the Graduate Faculty
of the Université de Haute-Alsace

in Partial Fulfillment of
the Requirements for the Degree of

DOCTOR OF PHILOSOPHY

November, 2012

THÈSE

Présentée pour obtenir le titre de

DOCTEUR DE L'UNIVERSITÉ DE
HAUTE-ALSACE

Spécialité: Chimie des Matériaux
Ecole doctorale Jean-Henri Lambert (ED 494)

Par
Yaroslav ODARCHENKO

Sujet:

TAILORING THE MESOSCOPIC STRUCTURE AND ORIENTATION OF SEMICRYSTALLINE AND LIQUID-CRYSTALLINE POLYMERS: FROM 1D TO 2D CONFINEMENT

Soutenue le 15 Novembre 2012 devant le jury composé de:

Dr. Jacques PENELLE: Rapporteur
Dr. Mari Cruz GARCIA GUTIERREZ: Rapporteur
Dr. Jean-Michel GUENET: Examinateur
Dr. Lallam ABDELAZIZ: Examinateur
Dr. Dimitri A. IVANOV: Promoteur

To my mother Natalia, sister Helena and wife Olga

ACKNOWLEDGEMENTS

After having my thesis written it is time to acknowledge all those who have made it possible for me to come so far. Most cordially I am grateful to my supervisor Dr. Dimitri A. Ivanov for his encouragement and support throughout my PhD project. I really admire your perfectionism and dedication to research. Also, special thanks for sharing your scientific knowledge and teaching me how to write papers or other scientific proceedings as well as how to give an effective presentations. It is always a pleasure for me to work with you. Besides this I would like to express my deep gratitude to Prof. Sergei Chvalun for making all this possible by introducing me to my current supervisor.

I am thankful to my colleagues, past and present, for being always open and always willing to help. Especially, I am deeply indebted to Dr. Martin Rosenthal who helped me to analyze the synchrotron data and for his amazing ability to never give up finding the solutions. In particular, I would like to thank Dr. Denis Anokhin for advising with structure modeling and Dr. Jaime J. Hernandez for the fruitful discussions and sharing the night shifts at the synchrotron. I will never forget the great moments we had during our missions to the ESRF, DESY and BNL and many things I learned from you all!

In addition, I want to express my gratitude to Dr. Wim Bras, Dr. Giuseppe Portale and Dr. Daniel H. Merino from the DUBBLE beamline (BM26) as well as Dr. Manfred Burghammer, Dr. Emanuela Di Cola and Dr. Richard Davies from the micro-focus beamline (ID13) at the ESRF (Grenoble) for providing measuring time and scientific support. With great pleasure I also want to thank Dr. Jan Perlich from the BW-4 beamline (DESY, Germany) as well as Dr. Vesna Stanic and Dr. Elaine DiMasi (BNL, USA) for the support with experiments in grazing set-up and a cosy family atmosphere at the beamline.

A large portion of my dissertation is based on the materials kindly granted by Dr. Jingbo Wang and Dr. Ahmed Mourran from the DWI Institute (Aachen Technical University, Germany) directed by Prof. Martin Moeller as well as Dr. Niels J. Sijbrandi from the Prof. Pieter J. Dijkstra's group at the University of Twente (Holland). I stay thankful for their collaboration.

My colleague Dr. Valeriy Luchnikov and his wife deserve special attention for their support throughout all these 3 years in setting up the bureaucracy issues and organization of the pleasant spare time. And some others who have allowed me to wade through institute regulations and procedures are Fabienne, Natalina, Louisa and Stephan. Thank you!

When I worked hard on my PhD project it was always nice to have a small pause. I say “Thank you” to my friends David Doblas, Kulaga Emilia, Nicolas Ducruet, Nelly Hobeika, Wajdi Heni, Dr. Arnaud Spangenberg, Fabrice Stehlin, Mohammad Rajab and others from my institute and elsewhere for sharing the office with me, going out to the concerts and other cultural events as well as playing football and learning french.

My mother has always put my sister’s and my interests before hers. Mom, I am very grateful for your altruism and for all those great opportunities that you provided me with. During my PhD work my family got bigger by two new members: my beautiful wife Olga and my adorable nephew David. Olga, thank you for the presence on my side, your care and patience, especially, during the writing of this manuscript. I am thankful to my sister for believe in me and to my brother in law, Sergiy, for our great getaways. I remain eternally appreciative to all of them for their unconditional love and support.

I am grateful to the members of my jury for reading this manuscript. Also I would like to acknowledge the French Ministry of Education, Research and Technology for financial support (M.E.R.T. bursary).

Yaroslav

TABLE OF CONTENTS

GLOSSARY

List of abbreviations, acronyms and symbols

Materials

PE	polyethylene
PP	polypropylene
PEO	poly(ethylene-oxide)
PDES	poly(di-*n*-ethylsiloxane)
PDPS	poly(di-*n*-propylsiloxane)
PTFE	poly(tetrafluoroethylene)
PEEA	poly(ether-ester-amide)
P2VP	poly(2-vinylpyridine)
P4VP	poly(4-vinylpyridine)
PHB	polyhydroxybutyrate
PU	polyurethane
PS	polystyrene
PVDF	poly(vinylidene fluoride)
PTHF	polytetrahydrofuran

Techniques

WAXS	Wide-Angle X-ray Scattering
SAXS	Small-Angle X-ray Scattering
GIWAXS	Grazing Incidence Wide-Angle X-ray Scattering
GISAXS	Grazing Incidence Small-Angle X-ray Scattering
TEM	Transmission Electron Microscopy
SAED	Selected-Area Electron Diffraction
SEM	Scanning Electron Microscopy
AFM	Atomic Force Microscopy
SPM	Scanning Probe Microscopy
POM	Polarized Optical Microscopy
DSC	Differential Scanning Calorimetry
TGA	Thermal Gravimetric Analysis
FTIR	Fourier Transform Infrared Spectroscopy

Other general abbreviations

ESRF	European Synchrotron Radiation Facility
DESY	Deutsches Elektronen Synchrotron
HASYLAB	Hamburg Synchrotron Laboratory
BNL	Brookhaven National Laboratory
NSLS	National Synchrotron Light Source

Other notations

HS	hard segment
SS	soft segment
LC	liquid crystal
BCP	block copolymer
TPE	thermoplastic elastomer
L_c	thickness of a lamellar crystal

L_B	long period
1D	one dimensional
2D	two dimensional

CHAPTER 1. GENERAL CONSIDERATIONS

In this chapter, a brief introduction to self-assembly of various polymer systems is given. The routes to induce spatial confinement employed in this work are described in the first section. The second section includes basic principles of polymer melting/crystallization phenomena. The third section is focused on the phase separation and crystallization in the block/segmented copolymers with crystallizable blocks. In particular, the role of H-bonding in the structure formation of segmented copolymers is underlined. The fourth section is about the columnar mesophase ordering for the case of long-chain molecules. The possibility to form complex hierarchical structures by the liquid-crystalline - semicrystalline block copolymers is presented in the fifth section. The last part contains the general aims of this work and gives the outline of the thesis.

1.1. Self-assembly under spatial confinement

Controlling the micro-structure of organic materials is crucial for a variety of their practical applications such as photonics, biomedicine, or the rapidly growing field of organic electronics.[1] Recent studies have shown a possibility to design the polymer structure on the nanoscale using self-assembly under the conditions of spatial confinement. Although in theory the minimization of the free energy is the main driving force in the self-assembly phenomena, in reality the interplay between the different processes such as crystallization, microphase separation or phase transition can strongly affect formed self-organized structures resulting in systems being out of thermodynamic equilibrium.

When the self-assembly takes place on the scale of several nanometers (*e.g.* the size of phase-separated domains in a typical block copolymer) the polymer morphology can become influenced by this spatial constraint. Therefore, the materials with at least one of dimensions at the nanoscale can exhibit a significantly different organization and physical properties as compared to their bulk analogues.

1.1.1. Routes of inducing the spatial confinement

There are different ways to tailor polymer self-assembly under spatial confinement. The main approaches used in this work are depicted in **Figure 1.1**. Thus, one can covalently bond a crystallizable segment to a non-crystallizable segment whereby the latter will serve as an amorphous matrix (cf. **Figure 1.1**A). One-dimensional (1D) ribbon-like crystals formation was reported for example for the case of segmented block copolymers with uniform crystallizable segments.[2–4] Another promising route consists in employing patterned substrates[5–7] (2D) or nanoporous templates[8–10] (1D) with a defined pore diameter (see **Figure 1.1**B). The orientation of both liquid-crystalline (LC) and crystalline soft-matter systems can be sometimes efficiently controlled by varying the surface roughness,[6,11,12] the pore size[13,14] or by modifying the surface wetting conditions[15]. Importantly, in the spatially-restricted domains the primary nucleation can switch from heterogeneous to homogeneous, as it was shown for isotactic polypropylene (iPP) embedded in nanoporous alumina by Duran *et al*. This approach allowed not only to control the crystallization kinetics but also the overall degree of crystallinity.[16] The crystallization under spatial confinement such as cylindrical cavities can result in the unusual polymorph formation, as it was observed for poly(vinylidene fluoride) (PVDF) exhibiting polar γ-phase nanorods formed on the supporting film consisting of nonpolar α-phase crystals.[10] Due to advances in synthetic chemistry a great variety of phase-

separated morphologies (i.e. cylinders, lamella, spheres, etc.) can be nowadays easily prepared by means of supramolecular approach.[17–20] For example, by selectively complexing a low-molecular weight mesogen, 3-pentadecylphenol (PDP), with P4VP block of the PS-b-P4VP block copolymer via non-covalent bonds one can obtain a LC-matrix with desired shape and domain size, which are strongly dependent on the degree of complexation (**Figure 1.1**C).[19] The non-covalent bonding in such supramolecular comb-coil diblock copolymers is thermally reversible, which is contrasted to the conventional block copolymers (linear or comb-coil diblock copolymers). The described supramolecular approach greatly facilitates the design of novel systems due to its flexibility and leads to richer phase diagrams. Noteworthy, if one of the blocks in a LC-containing block copolymer (BCP) has ability to crystallize as in the case of poly(ethylene-oxide) (PEO), the crystallization behaviour will be a function of the LC-segment content.[21]

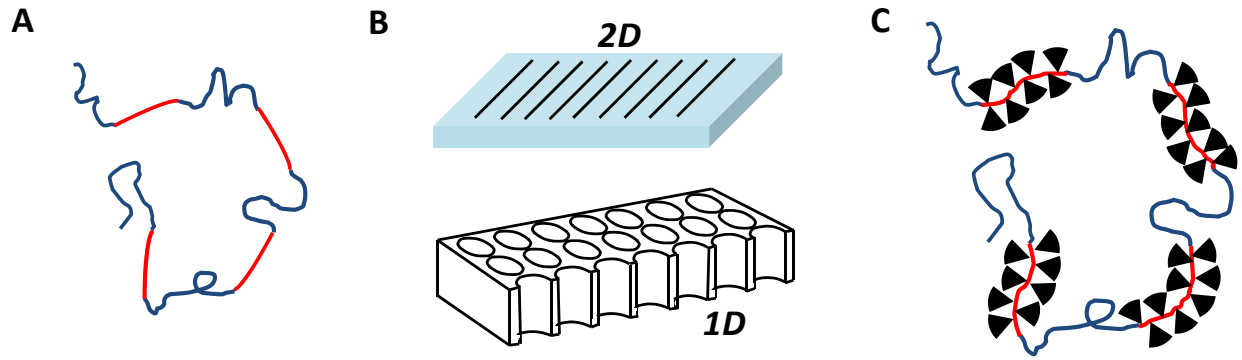

Figure 1.1. Approaches for tailoring the morphology of self-assembled systems by means of spatial confinement. (A) Covalently-bonded incompatible polymer segments, one of which is crystallizable and the other- amorphous. (B) Use of patterned substrates and nanoporous templates. (C) Supramolecular comb-coil diblock copolymers fabricated via non-covalent binding of low-molecular mesogen that exhibit LC-ordering.

Further in the text, the principles and theoretical basis of the most important phenomena in self-assembly of the different polymer systems will be discussed.

1.2. Polymer crystallization

Polymer crystallization is one of the most extensively studied examples of supramolecular self-assembly, which by historical reasons has not deserved the right to be called so.[22,23] It is well documented that polymer crystallization is a complex multistage process that considerably alters the physical and mechanical properties of the material. From the thermodynamic point of view, a crystal forms from the polymer melt below the melting point,

T_m, when it has a lower Gibbs free energy, G (cf. **Figure 1.2**). Although still being the subject of debate, the classical view of this process presents the extended-chain configuration of the crystal as state of the lowest possible free energy existing below the equilibrium melting temperature (see red line on **Figure 1.2**). One of the complications in the thermodynamic description of polymer crystals is that one has to distinguish the equilibrium melting temperature, T_m^0, of a perfect crystal formed by infinitely long stems from the normally measurable value T_m, which depends on the actual morphology of material.

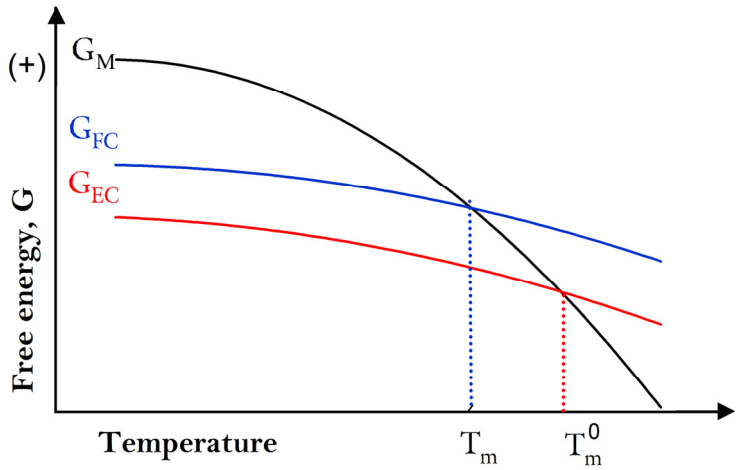

Figure 1.2. Gibbs free energy versus temperature for the polymer melt (M), folded-chain (FC) and extended-chain (EC) crystals.

When taking into account the constrains imposed by the entangled polymer chains it comes out that in most cases the molecules adopt the thermodynamically unfavorable but kinetically preferred folded-chain configuration in the crystal.[24] This leads to depression of T_m, as well as to a huge temperature hysteresis, *i.e.* the polymer melts and solutions usually crystallize at a temperature T_c, which is much lower than T_m^0 and even T_m. Therefore, the actual lamellar thickness (fold length) obtained at a certain crystallization temperature is determined by the population of crystals growing faster at this temperature, which is not necessarily, and even not at all, the thermodynamically most stable ones.

By definition, the value of ΔG, *i.e.* in our case the thermodynamic driving force for crystallization from the liquid state to a folded-chain crystal at T_c, can be expressed as:

$$\Delta G = \Delta H - T\Delta S \qquad (1.1)$$

where ΔH is the enthalpy change while ΔS denotes the entropy change. At T_m^0 the change of the Gibbs free energy due to the phase transition is zero, therefore

$$T_m^0 = \frac{\Delta H}{\Delta S} \tag{1.2}$$

Substituting Eq. (1.2) into (1.1) and assuming that the thermodynamic state functions *S* and *H* are weakly dependent on temperature, one obtains:

$$\Delta G = \frac{\Delta H(T_m^0 - T)}{T_m^0} \tag{1.3}$$

In the other words, the driving force of crystallization ΔG is proportional to the degree of supercooling, $\Delta T = T_m^0 - T_c$:

$$\Delta G = \frac{\Delta H \Delta T}{T_m^0} \tag{1.4}$$

As can be seen from Eq. (1.4), at a constant ΔG and supercooling higher values of ΔH bring about higher T_m^0.

1.2.1. Gibbs-Thomson equation

As pointed out by G. Strobl[25], the folded-chain crystals are metastable systems owing to their small size in the chain direction and typically melt much below the equilibrium melting temperature T_m^0 (cf. **Figure 1.2**). As a result, the surface free energy plays a significant role in defining the thermal behavior of such objects: the surface-to-volume ratio in this case is extremely high. Because of the surface free energy, σ, the Gibbs energy value for the folded-chain crystals is higher in comparison to the macroscopic phases satisfying the notion of Gibbs (see **Figure 1.2**).

The expression for the ΔG-value of a finite-size crystal (**Figure 1.3**) is the following:

$$\Delta G_{crystal}(T) = 2xy\sigma_e + 2l(x+y)\sigma - xyl\Delta G_f^{\infty}(T) \tag{1.5}$$

At the melting point of the crystal,

$$\left(\Delta G_{crystal}\right)_{T_m} = 0 \tag{1.6}$$

By assuming that $xy \gg l(x+y)$, which is the case for thin lamellae with large lateral dimensions, $\sigma_e \gg \sigma$, which is valid for most polymers, Eq. (1.5) can be rewritten as:

$$\Delta G_f^{\infty}(T_m) = 2\sigma_e / l \tag{1.7}$$

For an infinitely thick crystal at T_m^0, one gets:

$$\Delta G_f^{\infty}(T_m^0) = \Delta H_f^{\infty}(T_m^0) - T_m^0 \Delta S_f^{\infty}(T_m^0) \tag{1.8}$$

and consequently

$$\Delta S_f^{\infty}(T_m^0) = \Delta H_f^{\infty}(T_m^0)/T_m^0 \tag{1.9}$$

The Gibbs free energy of the same infinite crystal at T_m is given by:

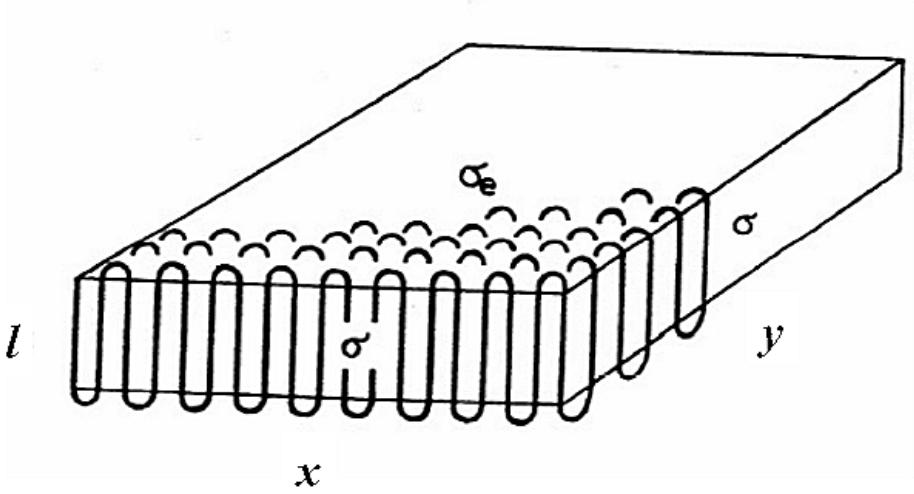

Figure 1.3. Scheme of a single polymer crystal. Symbol *l* stands for the fold length of the lamella; *x* and *y* are the lateral dimensions, σ_e and σ are the surface energies associated with the fold and lateral surfaces, respectively.

$$\Delta G_f^{\infty}(T_m) = \Delta H_f^{\infty}(T_m) - T_m \Delta S_f^{\infty}(T_m) \tag{1.10}$$

Considering that

$\Delta H_f^{\infty}(T_m) = \Delta H_f^{\infty}(T_m^0)$, *i.e.* the weak temperature dependence of the enthalpy is discarded, and

$\Delta S_f^{\infty}(T_m) = \Delta S_f^{\infty}(T_m^0)$ for high T_m's,

it can be shown that:

$$\Delta G_f^{\infty}(T_m) = \Delta H_f^{\infty}(T_m^0) - T_m \Delta S_f^{\infty}(T_m^0) \tag{1.11}$$

$$\Delta G_f^{\infty}(T_m) = \Delta H_f^{\infty}(T_m^0)[1 - \frac{T_m}{T_m^0}] \tag{1.12}$$

Comparing Eqs. (1.7) and (1.12), one obtains the following expression:

$$2\sigma_e / l = \Delta H_f^{\infty}(T_m^0)[1 - \frac{T_m}{T_m^0}] \tag{1.13}$$

The latter can be transformed in the conventional Gibbs-Thomson equation as follows:

$$T_m = T_m^0 \left[1 - \frac{2\sigma_e}{l \Delta H_f^{\infty} T_m^0}\right] \tag{1.14}$$

Since T_m^0 can hardly be determined by direct experiments this equation suggests one of convenient ways to estimate the values of T_m^0 as well as the surface energy σ_e. These quantities are obtained by plotting the experimental melting points T_m vs $1/l_c$ where the value of σ_e can be computed from the slope, and the intercept gives the value of T_m^0. In the past, SAXS and sometimes TEM were employed to determine the lamellar thickness l_c, whereas T_m is usually obtained by DSC. It is noteworthy that complications in using this

method may arise for instance due to thickening of the crystals during high-temperature annealing.

The knowledge of T_m^0 is crucial for understanding the physics of the polymer structure formation (e.g., the regime of crystallization). By comparing the equilibrium melting temperature of a polymer with the melting temperature of the corresponding shorter chains (oligomers) important morphological and structural information can be sometimes extracted. As was mentioned above direct determination of the equilibrium melting temperature is virtually unfeasible due to the molecular weight distribution, morphological constraints and kinetic limitations for the high molecular weights. To solve this problem one should refer to extrapolative methods. In the next section, we will consider the thermodynamics of fusion for the classical example of *n*-alkanes, which is believed to reflect some features of the linear polyethylene crystallization. The homologous series of *n*-alkanes are assumed to have strictly uniform chain length.

1.2.2. Fusion of monodisperse n-alkanes

Depending on the chain length, the alkanes exhibit extended or folded chain crystals. In particular, paraffins with the length equal to or lower than $C_{192}H_{386}$ form exclusively extended-chain crystallites when crystallized from the melt[26], whereas $C_{216}H_{434}$ shows a folded or extended-chain crystallites, depending on the crystallization temperature[27]. In the case of crystallization from diluted solution similar situation is found for $C_{214}H_{430}$, which forms two types of crystallites at different crystallization conditions.[28,29] At lower molecular weights only extended-chain crystals were observed. Hence our analysis will be restricted to extended-chain crystals, or relatively short alkanes.

According to Flory and Vrij the molar free energy of a chain with *n* repeating units at certain temperature can be written as[30]

$$n\Delta G_n = n\Delta G_u(T) + \Delta G_e(T) - RT\ln n \qquad (1.15)$$

where $\Delta G_u(T)$ is the free energy of fusion of a repeating unit in the limit of infinite chain length at temperature *T*, $\Delta G_e(T)$ denotes the end-group contribution which is assumed to be independent of *n*; $RT\ln n$ represents additional contribution to the entropy of fusion due to destroying of end-pairing upon melting (cf. **Figure 1.4**).

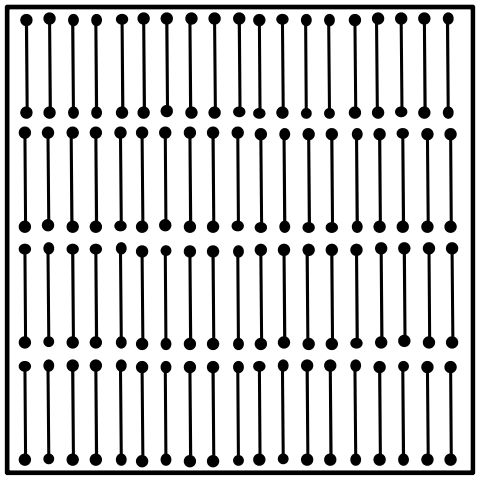

Figure 1.4. Schematic representation of low-molecular crystals. The vertical straight lines represent the ordered sequence conformation which are juxtaposed in successive layers of the crystalline lattice.[31]

The temperature dependence of ΔG_u and ΔG_e can be taken into account by performing a Taylor series expansion around the equilibrium melting temperature. By expanding ΔG_u to the second order gives:

$$\Delta G_u(T) = \Delta G_u - \Delta S_u[T - T_m^0] - \left(\Delta C_p/2T_m^0\right)[T - T_m^0]^2 \tag{1.16}$$

In this equation ΔG_u and ΔS_u correspond to the values at the equilibrium melting temperature. Setting $\Delta T = T_\mathrm{m}^0 - T$ and keeping in mind that at T_m^0, $\Delta G_u = 0$ and $\Delta S_u = \Delta H_u/T_m^0$, Eq. (1.16) transforms to:

$$\Delta G_u(T) = \Delta H_u \Delta T/T_m^0 - \Delta C_p(\Delta T)^2/2T_m^0 \tag{1.17}$$

By expanding ΔG_e to the first order one obtains:

$$\Delta G_e(T) = \Delta G_e - \Delta S_e[T - T_m^0] \tag{1.18}$$

which reduces to:

$$\Delta G_e(T) = \Delta H_e - T\Delta S_e \tag{1.19}$$

where ΔH_e and ΔS_e are the enthalpy and entropy of melting of the end-groups, respectively. Noteworthy that both ΔG_u and ΔG_e could be expanded to as high an order as required, however, the second- and first-order expansions, that are used here, are satisfactory for our purposes. By substituting Eqs. (1.19) and (1.17) into Eq. (1.15) the free energy of melting can be obtained as:

$$n\Delta G_n = n\left[\Delta H_u \Delta T/T_m^0 - \Delta C_p(\Delta T)^2/2T_m^0\right] + \Delta H_e - T\Delta S_e - RT\ln n \tag{1.20}$$

At the melting point of a paraffin, $\Delta G_n = 0$ and $T = T_m$. The expression can be rearranged as:[30]

$$\frac{n\Delta H_u \Delta T}{R} - \frac{n\Delta C_p(\Delta T)^2}{2R} - T_m T_m^0(\ln n) = \frac{T_m^0(T_m \Delta S_e - \Delta H_e)}{R} \tag{1.21}$$

Therefore, the melting temperature of the *n*-alkanes can be approximated to:

$$T_m^0 \cong \frac{0.5n\left(2\Delta H_u \Delta T - \Delta C_p (\Delta T)^2\right)}{T_m(\Delta S_e + R\ln n) - \Delta H_e} \tag{1.22}$$

One of the ways to check the validity of the Flory-Vrij analysis is to compare the calculated melting temperatures with the ones obtained experimentally. A summary of the melting temperatures reported for all of the *n*-alkanes is shown in **Figure 1.5**.[32] The solid curve corresponds to the calculated values of T_m plotted against *n* for the paraffin homologues up to C_{400}. For this calculation T_m^0 was taken to be 145.5 °C. Despite the slight deviation for the big *n* values the theory gives a satisfactory representation of the *n*-alkane melting temperatures.

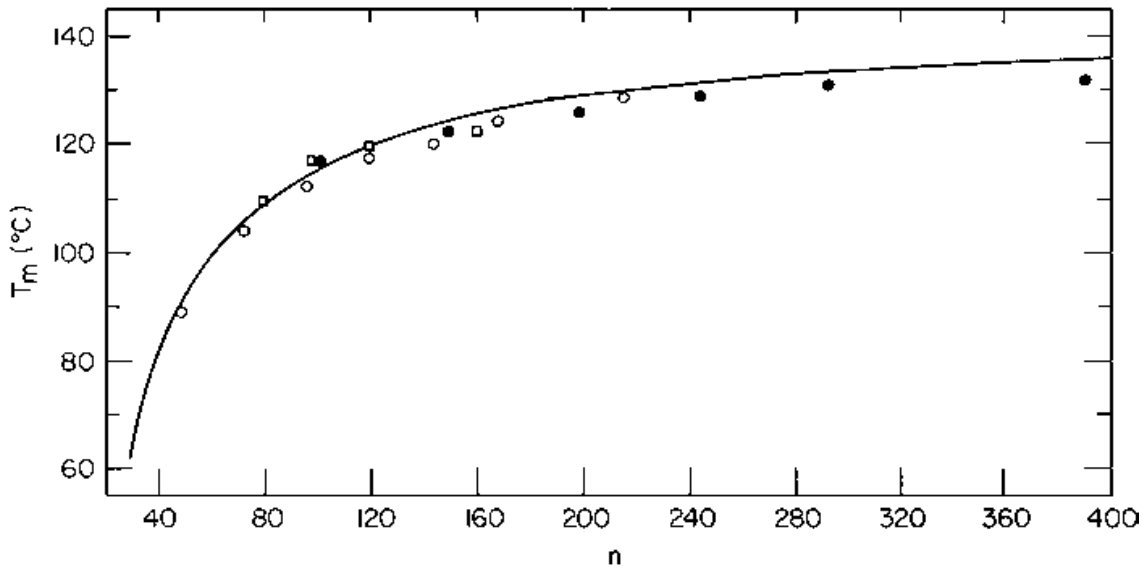

Figure 1.5. Melting temperature of *n*-alkanes as a function of chain length. Solid curve calculated from Flory–Vrij analysis.[30] Experimental results: closed circles - Ungar *et al.*[26]; open circles - Flory and Vrij[30], Lee and Wegner[27]; open squares - Takamizawa *et al.*[33].

In the next section, we will discuss the role of different processes such as crystallization and microphase segregation that accompany the structure formation in the systems such as segmented copolymers with uniform hard segments, main-chain liquid crystals and liquid-crystalline (LC) – semicrystalline BCPs.

1.3. Structure formation in block copolymers

Block copolymers with different chain architectures (see **Figure 1.6**) have been attracting attention during the last decades due to their ability to self-assemble at the nanometer scale.[34,35,36] The microphase separation owing to the repulsive interaction between the

constitutive blocks attached to each other leads to formation of polymer morphology consisting of periodic domains (**Figure 1.7**). The periodicity, size and symmetry of the domains can be tuned by changing the molecular parameters, the fact that renders the BCPs promising for various nanotechnological applications (e.g., electronics,[36,37,38] membranes,[38,39] drug-delivery,[40] etc.). For copolymers composed of two amorphous blocks without any specific interactions, two parameters χN and f define the phase diagram. The χ-parameter is the Flory-Huggins interaction parameter, N is the total polymerization degree of the copolymer and f is the volume fraction of one block. The phase diagram of this system has been well described theoretically. **Figure 1.7** schematically shows the self-assembled structures formed by the polyisoprene-polystyrene diblock copolymer.[41]

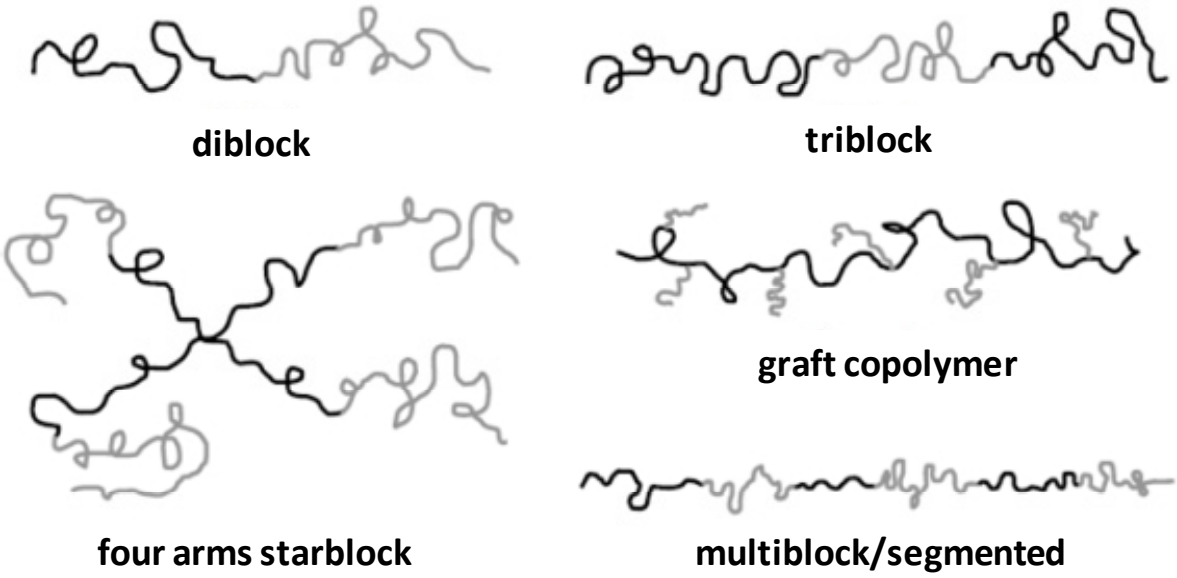

Figure 1.6. Various block copolymer architectures.[42]

It should be noted that rigorous application of the mean-field theories developed for the diblock copolymers is limited for the cases when one block is crystallizable.

Further in the text, the structure of the copolymer systems with crystallizable blocks and blocks with H-bonds forming units will be considered in detail. Different nanoconfinement geometries created by the block/segmented copolymers will be pointed out.

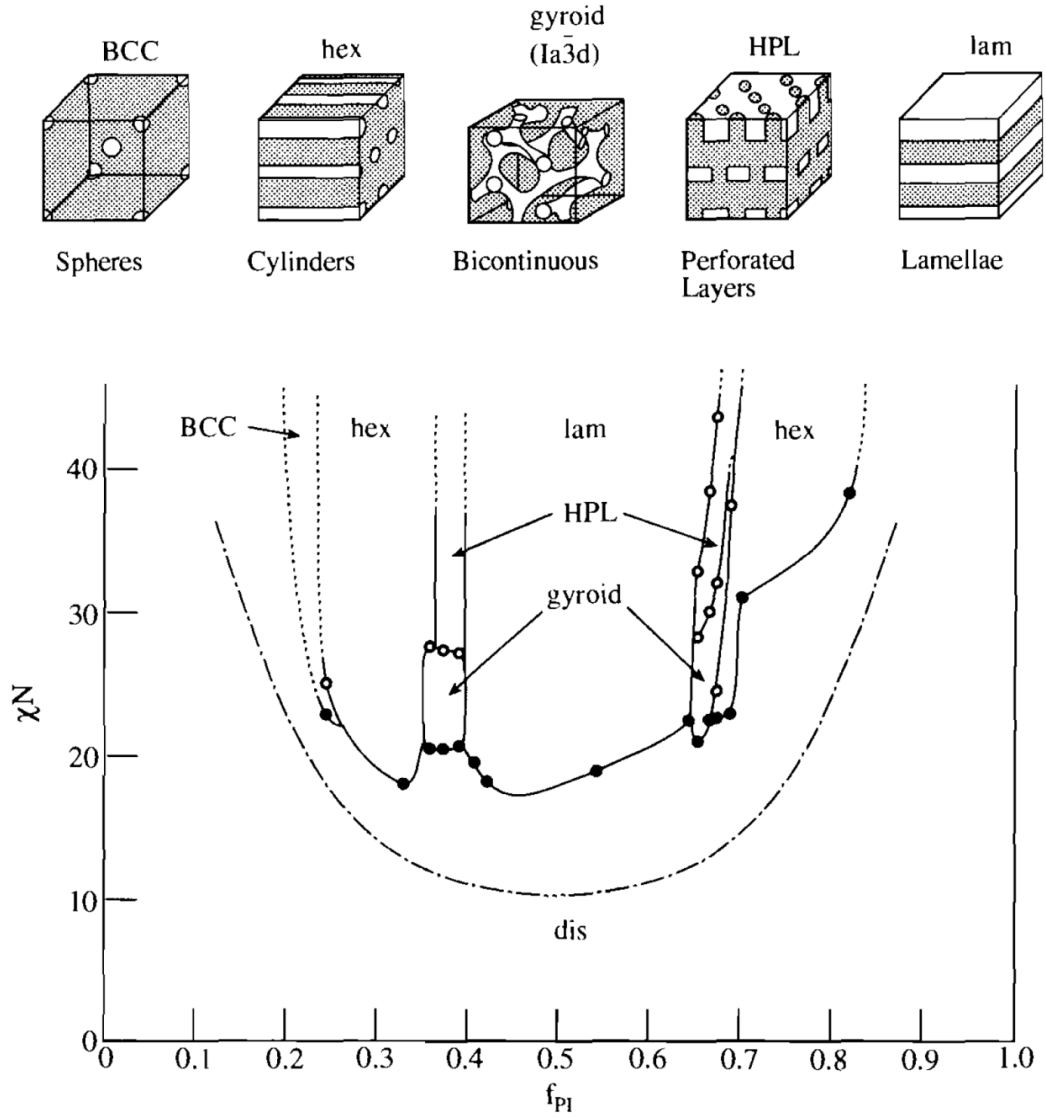

Figure 1.7. Phase diagram for poly(isoprene-styrene) diblock copolymer.[41]

1.3.1. Semicrystalline block copolymers

As mentioned above, the spatially confined domains can be easily created within the phase-separated diblock copolymer morphology. The semicrystalline block copolymers containing one crystallizable block is an important family of BCPs, for which hierarchical ordering and competition between microphase separation and crystallization on different length scales are observed.[43,44,45] The semicrystalline block can crystallize in the nanoconfined environment, whereby the crystallization mechanism is mainly controlled by the BCP morphology, crystallization behavior of the semicrystalline block and glass transition of the amorphous block. Depending on the interplay between these factors, two confinement regimes with different crystallization mechanisms are typically observed, i.e. the so-called

hard and soft confinement.[44,46] Thus, the crystallization can remain confined within the micro-phase separated regions either when the amorphous segment is glassy ($T_{ODT} > T_g > T_c$) or for strongly microphase separated blocks (large values of χ).[21,38] This situation is termed "hard confinement regime". In contrast, if the amorphous block is in the rubbery state at the crystallization temperature ($T_{ODT} > T_c > T_g$) or if the driving force of the microphase separation is weak, the block copolymer structure can be ruptured by the crystallization process resulting in the so-called "break-out crystallization".[47,45] The latter case is termed "soft confinement regime". In the hard-confinement regime various nanoconfined environments such as spheres, cylinders or lamellae (cf. **Figure 1.7**) can be associated to heterogeneous or homogeneous nucleation mechanisms. Thus, Loo *et al.* have reported for polyethylene (PE) in poly(vinyl cyclohexane) matrix homogeneous nucleation with first-order kinetics (n=1) for the isolated morphologies (sphere, cylinders) and heterogeneous nucleation with n>1 for gyroid and lamellar structures.[48] Moreover, for the hexagonal BCP morphology TEM micrographs revealed PE ribbon-like crystals running along the cylinder axis,[49] while for the BCP lamellar phase the PE crystals were randomly oriented.[48] In the case of poly(ethylene oxide) confined in 1D cylindrical domains within the glassy amorphous polystyrene (PS) matrix the orientation of the PEO crystals was tailored by the crystallization temperature T_m.[50] The ***c***-axis of PEO crystal gradually changed from random at T_m < -30 °C to inclined with respect to the cylinder axis and finally became perpendicular at $T_m \geq 2$ °C as was concluded from the X-ray data (**Figure 1.8**). Noteworthy, in the soft confinement regime the crystallization is characterized by conventional sigmoidal kinetics independently of the copolymer morphology.[45,51]

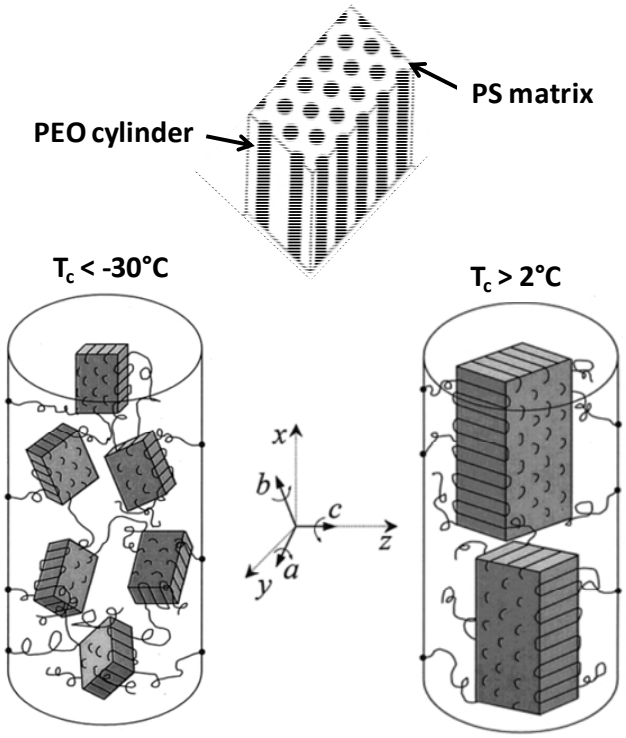

Figure 1.8. Temperature-dependent orientation of the poly(ethylene oxide) crystals confined within the 1D nanocylinders formed by poly(ethylene oxide)-b-polystyrene/polystyrene blend.[50]

1.3.2. Segmented copolymers

Segmented copolymers with alternating soft and hard segments combine the physical characteristics of conventional elastomers (e.g. vulcanized natural rubber) with the processing characteristics of thermoplastics. Polymers based on ester or ether groups with a low glass transition temperature are often used as flexible soft segments (SSs), while the hard segments (HSs) can be either polymers or short chains containing carbamate (urethane), urea or amide groups. A sketch of the segmented copolymer morphology comprising fast crystallizable HSs is depicted in **Figure 1.9**. As a result of the phase-separated morphology the HSs form rigid domains (A) uniformly dispersed or highly interconnected (B) in the SS matrix (D), depending on the relative segments ratio. These domains act as physical cross-links providing stiffness and strength to the material. Such segmented copolymers can be processed from solution or by heating the materials above the vitrification point (in case of amorphous HSs) or melting point (in case of semicrystalline HSs).

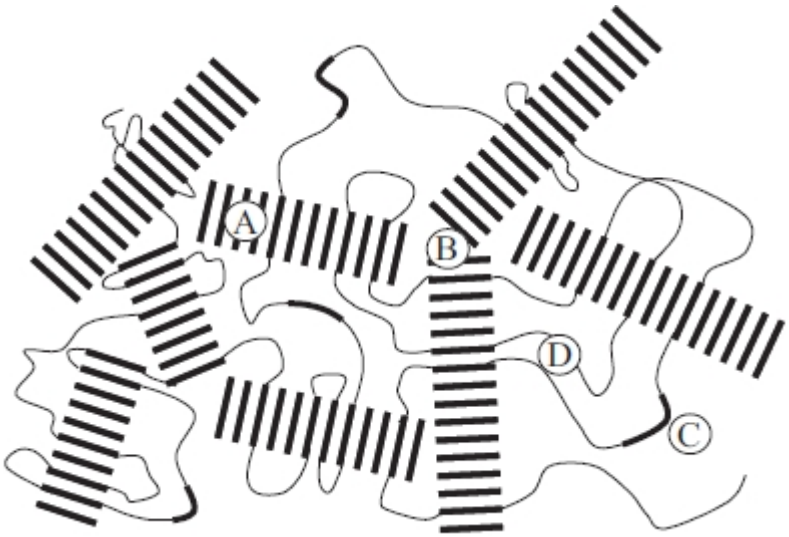

Figure 1.9. Schematics of a typical morphology of a segmented block copolymer with crystallizable HSs. (A) crystalline HS domain, (B) junction of crystalline lamellae, (C) amorphous HS and (D) amorphous SS phase.[52]

In general, the extent of phase separation depends on the chemical nature, weight fractions, polydispersity and molecular weight of the hard and soft macromonomers.[53–57] Also, the phase separation between the segments can be enhanced by crystallization of the hard segment, as can be learned from the work by Schneider and Sung[55] on polyether/polyester based polyurethanes (PUs) where semicrystalline HS (symmetric 2,6 toluene diisocyanate (TDI)) exhibits a higher degree of microphase separation than the corresponding material with amorphous HS (asymmetric 2,4 TDI).

Obviously, the morphology of copolymers with crystallizable segments strongly depends on the HS/SS weight ratio.[58–61] When HS/SS<1 the soft segment forms a continuous phase and materials show elastomeric behaviour, whereas the HS-rich polymers (HS/SS>1) with the hard segment forming continuous phase are characterized by higher modulus and lower elastic deformation typical of thermoplastics. It is a common observation that the HS exhibits lamellar crystals which are able to form larger spherulitic superstructures at high HS content similar to the ones observed for semicrystalline homopolymers.[58,60] In addition to lamellar structures, ribbon-like crystals with a high aspect ratio comprised of non-folded chains have also been reported for the segmented copolymers with low HS contents.[3,62,63]

Recently, a special type of segmented copolymers with strictly uniform HSs was synthesized.[56,64,65] In comparison to materials with non-uniform HSs, the copolymers comprising monodisperse hard blocks demonstrate an almost complete phase separation and therefore possess a much broader thermal service window along with improved ultimate

mechanical properties.[53,56] Thus, even at HS concentrations as low as 3 wt% the adipic acid tetraamide segmented copolymer shows a distinct phase-separated morphology and hence good mechanical properties.[63] Independently of the chemical nature (aromatic or aliphatic) the HSs are short (several nanometers) and they cannot fold during crystallization.

The presence of hydrogen bonds contributes to the solubility δ according to the so-called "three-dimensional" solubility parameter proposed by Hansen[66],

$$\delta^2 = \delta_d^2 + \delta_h^2 + \delta_p^2 \tag{1.23}$$

where δ_d, δ_h, δ_p are the solubilities owing to dispersion (van der Waals or London) forces, H-bonds or permanent dipole interactions, respectively. Noteworthy, for the urethane moiety the contribution of the δ_h to δ can be as high as 68%.[67]

The Flory-Huggins interaction parameter χ is connected to the solubility parameter via the following equation:

$$\chi = \frac{v(\delta_1 - \delta_2)^2}{RT} \tag{1.24}$$

where δ_1 and δ_2 are the solubility parameters of species 1 and 2, ν is the molar segmental volume of species 1 and 2 (assumed to be identical here), R is the universal gas constant, and T is temperature in degrees K. Therefore, it is clear that the hydrogen bonding has an important implication on the phase segregation of block/segmented copolymers. Yilgör showed for series of the PDMS containing segmented copolymers with the H-bonds forming urea and urethane HSs that the mechanical properties and thermal stability are directly linked to the strength of intermolecular hydrogen bonding in the HSs.[67] Commonly, the issues of microphase separation and hydrogen bonding are not easily distinguishable in segmented thermoplastic elastomers of commercial importance.

1.4. Main-chain liquid-crystalline polymers

Liquid crystals (LCs) are naturally self-organized systems. In comparison to the crystalline state of matter, LC phases show improved processing characteristics, easier control of alignment and self-healing of structural defects. The unique combination of order and mobility makes them suitable for numerous practical applications such as light emitting diodes,[68] photovoltaic cells,[69,70] and field effect transistors.[71] In the discussion that follows we will concentrate on the polymer LCs.

Typically, polymers exhibit LC mesophases when mesogenic moiety is incorporated in the backbone chain or attached to the side by flexible linkage. In most cases, the mesogenic parts

are calamitic (rod-like) or discotic (disk-like). Nevertheless, there is a large group of main-chain LC polymers which do not have any mesogenic units in their chemical structure. In this case, the column represents a single conformationally disordered polymer chain, arranged on a 2D lattice.

Goran Ungar[72] classified the macromolecules, which can form hexagonal columnar mesophases into the three main types (**Figure 1.10**):

1. Flexible linear macromolecules (polyethylene at high pressure,[73,74] polytetrafluoroethylene,[75,76] *etc.*);

2. Flexible branched (comb-like) macromolecules (alkyl-polysiloxanes,[77,78] polysilanes,[79,80] polyphosphazenes,[78,81] *etc.*);

3. Rigid macromolecules with flexible side-chains (cellulose derivatives[82] and *n*-alkyl substituted poly(L-glutamate)[83]).

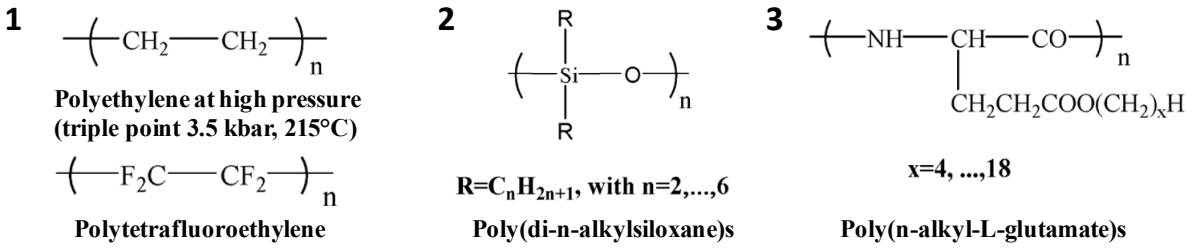

Figure 1.10. Examples of polymers forming a hexagonal mesophase according to classification of G. Ungar.[72]

For the second group, the amphiphilic nature of polymer is thought to be responsible for the LC behavior. Indeed, the inorganic backbone is flexible and polar while the side chains represent various apolar substituents. The columns are characterized by the long-range lateral order and short-range order along the columnar axis. In the mesophase, the main polymer chain is placed along the columnar axis as shown in **Figure 1.11** for a poly(di-*n*-propylsiloxane) (PDPS).

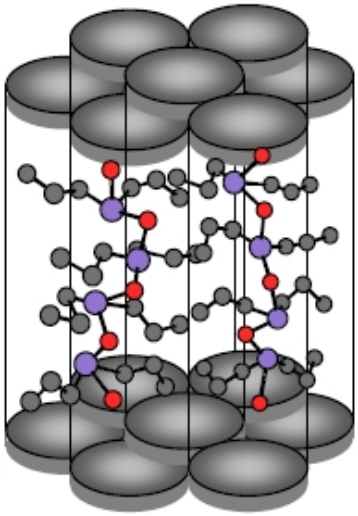

Figure 1.11. Scheme of the columnar hexagonal packing for the poly(di-*n*-propylsiloxane).

The role of confinement on the LC domains alignment and phase transition in main-chain LCs was studied by Defaux *et al.*[6,84] Two mesomorphic morphologies in the thin PDPS films were observed (**Figure 1.12**): the lamellar ribbons with the backbones lying in the film plane and cylindrites with a circular symmetry where polymer chains are oriented perpendicular to the substrate. Furthermore, while crystallizing from the LC phase, the gross morphological features did not change and the PDPS α-phase crystals formed via epitaxial growth on the parent mesophase.

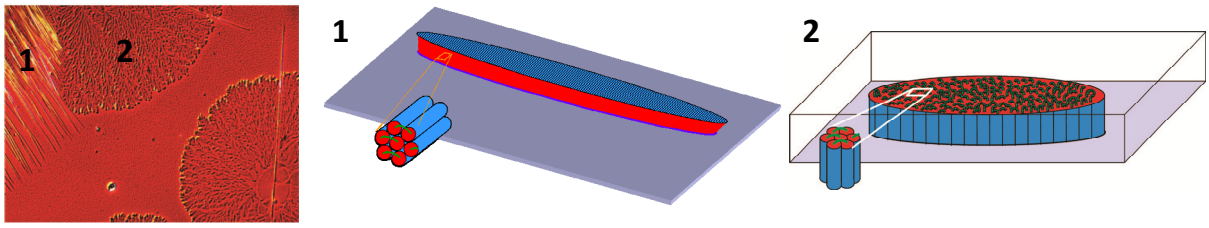

Figure 1.12. Optical image of mesomorphic morphologies in thin PDPS films: (1) lamellar ribbons and (2) cylindrites.

1.5. Confined crystallization in liquid-crystalline (LC) - semicrystalline block copolymers

To induce orientation in block copolymers, various approaches have been developed such as the use of electric[85]/magnetic[86] fields, solvent evaporation methods,[87] minimization of the interfacial tension,[88] surfactant-assisted orientation,[89] and others. Another promising way to control the orientation and morphology of BCPs is a confinement imposed by surrounding

liquid-crystalline phase. The LC ordering can be introduced via covalent bonding[21,90–92] or via supramolecular self-assembly.[17,93] In the latter case, a mesogen is selectively complexed with one segment of the block copolymer to render it liquid crystalline via non-covalent bonds such as hydrogen bonding, ionic or charge-transfer interactions.[17,19,94–96] Ikkala *et al.*[17,19] showed that the polymeric complexes composed of poly(styrene-b-4-vinylpyridine) (PS-P4VP) and alkylphenol or amphiphilic surfactants have similar micro-structure as side-chain liquid-crystalline block copolymers. Chuang *et al.*[96] used wedge-shaped benzoic acid to complex with PS-P4VP, they found that in the bulk, the global block copolymer morphology can be tuned from lamellae to cylinders, and to tetragonally perforated layer by simply adjusting the amount of the ligand, whereas the morphology of the P4VP-ligand complex changed from smectic phase to disordered columnar phase and to ordered columnar phase.

In the liquid-crystalline (LC) - semicrystalline BCPs, hierarchically-ordered structures are expected with the characteristic length scale of the LC ordering comprised between 1 and 10 nm and that of the confined domains from 10 to 100 nm. Unlike the amorphous-crystalline BCPs, no systematic studies on the structure formation in liquid-crystalline (LC) – semicrystalline block copolymers have been conducted so far. Recently, Zhou *et al.*[21] showed that the crystallization behavior of a semicrystalline block such as PEO was controlled by the weight fraction of the LC segment in the side chain liquid crystalline (LC) - semicrystalline BCP (**Figure 1.13**). Thus, if the LC weight fraction is less than 50%, PEO crystallizes in the "LC lamellae in PEO lamellae" structure at normal undercoolings, while for high LC contents (LC>50%) PEO crystallizes only at very large undercoolings and forms the "PEO cylinders in LC matrix" structure.

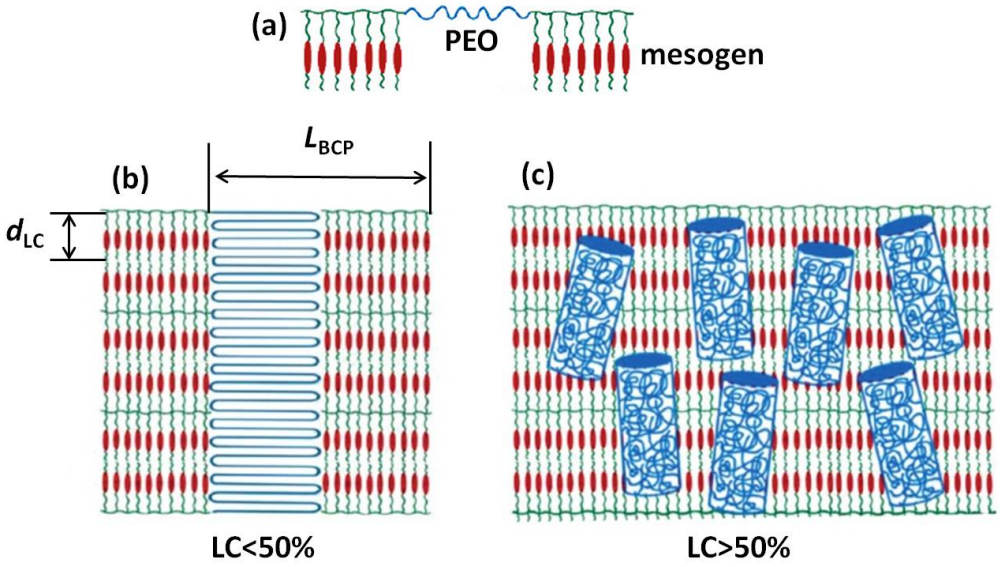

Figure 1.13. Schematic representation of the hierarchic morphologies for (a) LC-PEO-LC triblock copolymer: (b) "LC lamellae in PEO lamellae" and (c) "PEO cylinders in LC matrix".[21]

1.6. Aims of the work and outline

In the present thesis, various polymer systems including segmented copolymers with crystallizable units, main-chain LC macromolecules and liquid-crystalline – semicrystalline BCPs will be described. The aim of the study is to understand the role of different processes such as crystallization, microphase separation and phase transition in the structure formation under confinement.

The main experimental techniques applied in my work are briefly described in **Chapter 2**. The relevance of the used techniques to investigate the semicrystalline and LC polymer structures is specifically addressed. In particular, a combination of direct- and reciprocal-space experimental techniques has been used to characterize the orientation and morphology of the materials.

In **Chapter 3** the 1D-confinement of the crystallization process is studied for poly(ether-ester-amide)s. Their morphology consists of fiber-like nano-crystals randomly dispersed in the soft polymer matrix. The micro-structural parameters of the copolymers were addressed by simultaneous small- and wide-angle X-ray scattering. It is shown that the crystals have strictly identical thickness, which is close to the contour length of the hard segment.

Chapter 4 relates the mechanical properties of the copolymers to the structure of the hard segment. To this end, uniaxially-oriented samples are analyzed. The strain hardening induced by crystallization of the soft segment results in break stress and break strain which are approximately 75% higher when the PTHF (soft block) length is increased from 1000 to

2900. The effect of strictly monodisperse hard segments reflects in a fast and complete crystallization, and, most strikingly, in independence of the crystal thickness from the thermal history. The role of the hydrogen bonds which are parallel to the long dimension of the crystals on the mechanical properties of the materials is discussed.

Chapter 5 deals with the spatial confinement induced either by impregnation of polymers in porous nano-templates or by specially prepared nanostructured substrates. For the case of the main-chain LC polymers, we show that orientation of columnar mesophases strongly depends on the length of the alkyl side chains for thin deposited films as well as on the pore size of the nano-templates.

In **Chapter 6**, the LC ordering of liquid-crystalline - semicrystalline diblock copolymers (P2VP-PEO) complexed with a wedge-shaped mesogen confines the PEO crystallization. Different confinement environments will be generated and studied as a function of the degree of complexation.

The thesis is concluded with a brief summary of the main results.

1.7. References

(1) *Encyclopedia of Nanoscience and Nanotechnology*; Nalwa, H. S., Ed.; American Scientific Publishers, 2004.

(2) Niesten, M. C. E. J.; Harkema, S.; Heide, E. V. D.; Gaymans, R. J. *Polymer* **2001**, *42*, 1131–1142.

(3) Versteegen, R. M.; Kleppinger, R.; Sijbesma, R. P.; Meijer, E. *Macromolecules* **2006**, *39*, 772–783.

(4) Sijbrandi, N. J.; Kimenai, A. J.; Mes, E. P. C.; Broos, R.; Bar, G.; Rosenthal, M.; Odarchenko, Y.; Ivanov, D. A.; Dijkstra, P. J.; Feijen, J. *Macromolecules* **2012**, *45*, 3948–3961.

(5) Wittmann, J. C.; Smith, P. *Nature* **1991**, *352*, 414–417.

(6) Defaux, M.; Vidal, L.; Möller, M.; Gearba, R. I.; Dimasi, E.; Ivanov, D. A. *Macromolecules* **2009**, *42*, 3500–3509.

(7) Smith, H. I.; Flanders, D. C. *Applied Physics Letters* **1978**, *32*, 349.

(8) Masuda, H.; Fukuda, K. *Science (New York, N.Y.)* **1995**, *268*, 1466–8.

(9) Steinhart, M.; Wendorff, J. H.; Wehrspohn, R. B. Chemphyschem : a European journal of chemical physics and physical chemistry **2003**, 4, 1171–6.

(10) García-Gutiérrez, M.-C.; Linares, A.; Hernández, J. J.; Rueda, D. R.; Ezquerra, T. a; Poza, P.; Davies, R. J. *Nano letters* **2010**, *10*, 1472–6.

(11) Berreman, D. W. *Le Journal de Physique Colloques* **1979**, *40*, C3–58–C3–61.

(12) Lee, B. W.; Clark, N. A. *Science* **2001**, *291*, 2576–80.

(13) Shin, K.; Woo, E.; Jeong, Y. G.; Kim, C.; Huh, J.; Kim, K. *Macromolecules* **2007**, *40*, 6617–6623.

(14) Steinhart, M.; Zimmermann, S.; Göring, P.; Schaper, A. K.; Gösele, U.; Weder, C.; Wendorff, J. H. *Nano letters* **2005**, *5*, 429–34.

(15) Steinhart, M.; Senz, S.; Wehrspohn, R. *Macromolecules* **2003**, *36*, 3646–3651.

(16) Duran, H.; Steinhart, M.; Butt, H.-J.; Floudas, G. *Nano letters* **2011**, 0–4.

(17) Ikkala, O.; Brinke, G. ten; ten Brinke, G. *Science* **2002**, *295*, 2407–9.

(18) Ruokolainen, J.; Makinen, R.; Torkkeli, M.; Makela, T.; Serimaa, R.; Ten Brinke, G.; Ikkala, O. *Science* **1998**, *280*, 557–560.

(19) Valkama, S.; Ruotsalainen, T.; Nykänen, A.; Laiho, A.; Kosonen, H.; ten Brinke, G.; Ikkala, O.; Ruokolainen, J. *Macromolecules* **2006**, *39*, 9327–9336.

(20) Zhu, X.; Beginn, U.; Möller, M.; Gearba, R. I.; Anokhin, D. V. D. V.; Ivanov, D. A. *Journal of the American Chemical Society* **2006**, *128*, 16928–37.

(21) Zhou, Y.; Ahn, S.; Lakhman, R. K.; Gopinadhan, M.; Osuji, C. O.; Kasi, R. M. *Macromolecules* **2011**, *44*, 3924–3934.

(22) Wunderlich, B. Macromolecular Physics, Vol 2. Crystal Nucleation, Growth, Annealing; Academic Press: London, 1976.

(23) Geil, P. H. *Polymer single crystals*; Wiley-Interscience, 1963.

(24) Hoffman, J. D.; Laurintzen, J. Journal of Research of The National Bureau of Standards **1961**, A 65, 297.

(25) Strobl, G. The Physics of Polymers: Concepts for Understanding Their Structures and Behavior; 2nd ed.; Springer, 1997.

(26) Ungar, G.; Stejny, J.; Keller, A.; Bidd, I.; Whiting, M. C. *Science (New York, N.Y.)* **1985**, *229*, 386–9.

(27) Lee, K.; Wegner, G. Makromolekulare Chemie-Rapid Communications **1985**, 6, 203–208.

(28) Kloos, F.; Go, S.; Mandelkern, L. *Journal of Polymer Science: Polymer Physics Edition* **1974**, *12*, 1145–1162.

(29) Leung, W. M.; St. John Manley, R.; Panaras, A. R. *Macromolecules* **1985**, *18*, 760–771.

(30) Flory, P. J.; Vrij, A. *J. Am. Chem. Soc.* **1963**, *85*, 3548–3553.

(31) Mandelkern, L.; Alamo, R. G.; Dorset, D. L. *Acta chimica Hungarica* **1993**, *130*, 415–439.

(32) Mandelkern, L.; Prasad, A.; Alamo, R. G.; Stack, G. M. *Macromolecules* **1990**, *23*, 3696–3700.

(33) Takamizawa, K.; Ogawa, Y.; Oyama, T. *Polymer Journal* **1982**, *14*, 441–456.

(34) Ho, R.-M.; Chen, C.-K.; Chiang, Y.-W. *Macromolecular Rapid Communications* **2009**, *30*, 1439–1456.

(35) Krausch, G.; Magerle, R. *Advanced Materials* **2002**, *14*, 1579–1583.

(36) Stoykovich, M. P.; Nealey, P. F. *Materials Today* **2006**, *9*, 20–29.

(37) Kim, H.-C.; Park, S.-M.; Hinsberg, W. D. *Chemical reviews* **2010**, *110*, 146–77.

(38) Park, C.; Yoon, J.; Thomas, E. L. *Polymer* **2003**, *44*, 6725–6760.

(39) Wisse, E.; Spiering, A. J. H.; van Leeuwen, E. N. M.; Renken, R. A. E.; Dankers, P. Y. W.; Brouwer, L. A.; van Luyn, M. J. A.; Harmsen, M. C.; Sommerdijk, N. A. J. M.; Meijer, E. W. *Biomacromolecules* **2006**, *7*, 3385–95.

(40) Lips, P. a M.; van Luyn, M. J. a; Chiellini, F.; Brouwer, L. a; Velthoen, I. W.; Dijkstra, P. J.; Feijen, J. *Journal of biomedical materials research. Part A* **2006**, *76*, 699–710.

(41) Khandpur, A. K.; Foerster, S.; Bates, F. S.; Hamley, I. W.; Ryan, A. J.; Bras, W.; Almdal, K.; Mortensen, K. *Macromolecules* **1995**, *28*, 8796–8806.

(42) Hamley, I. W. *The physics of block copolymers*; Oxford Science Publications: New York, 1998.

(43) Huang, P.; Zhu, L.; Guo, Y.; Ge, Q.; Jing, A. J.; Chen, W. Y.; Quirk, R. P.; Cheng, S. Z. D.; Thomas, E. L.; Lotz, B.; Hsiao, B. S.; Avila-Orta, C. a.; Sics, I. *Macromolecules* **2004**, *37*, 3689–3698.

(44) Zhu, L.; Mimnaugh, B. R.; Ge, Q.; Quirk, R. P.; Cheng, S. Z. D.; Thomas, E. L.; Lotz, B.; Hsiao, B. S.; Yeh, F.; Liu, L. *Polymer* **2001**, *42*, 9121–9131.

(45) Loo, Y.-L.; Register, R. a.; Ryan, A. J. *Macromolecules* **2002**, *35*, 2365–2374.

(46) Nandan, B.; Hsu, J.; Chen, H. Journal of Macromolecular Science, Part C: Polymer Reviews **2006**, 46, 143–172.

(47) Xu, J.-T.; Fairclough, J. P. a.; Mai, S.-M.; Ryan, A. J.; Chaibundit, C. *Macromolecules* **2002**, *35*, 6937–6945.

(48) Loo, Y.-L.; Register, R. a.; Ryan, A. J.; Dee, G. T. *Macromolecules* **2001**, *34*, 8968–8977.

(49) Loo, Y.-L.; Register, R. A.; Adamson, D. H. *Journal of Polymer Science Part B: Polymer Physics* **2000**, *38*, 2564–2570.

(50) Huang, P.; Zhu, L.; Cheng, S. Z. D.; Ge, Q.; Quirk, R. P.; Thomas, E. L.; Lotz, B.; Hsiao, B. S.; Liu, L.; Yeh, F. *Macromolecules* **2001**, *34*, 6649–6657.

(51) Nojima, S.; Nakano, H.; Ashida, T. *Polymer* **1993**, *34*, 4168–4170.

(52) Cella, R. Journal of polymer science part C-Polymer Symposium **1973**, 727–740.

(53) Harrell, L. L. *Macromolecules* **1969**, *2*, 607–612.

(54) Godovsky, Y. K.; Yanul, N. A.; Bessonova, N. P. *Colloid & Polymer Science* **1991**, *269*, 901–915.

(55) Schneider, N. S.; Sung, C. S. P. *Polymer Engineering and Science* **1977**, *17*, 73–80.

(56) Ng, H. N.; Allegrezza, A. E.; Seymour, R. W.; Cooper, S. L. *Polymer* **1973**, *14*, 255–261.

(57) Takahara, A.; Tashita, J.; Kajiyama, T.; Takayanagi, M.; MacKnight, W. J. *Polymer* **1985**, *26*, 987–996.

(58) Sheth, J. P.; Xu, J.; Wilkes, G. L. *Polymer* **2003**, *44*, 743–756.

(59) Samuels, S.; Wilkes, G. Journal of polymer science part C-Polymer Symposium **1973**, 149–178.

(60) Eustache, R.-P. Fakirov, S., Ed.; Wiley-VCH: Weinheim, 2005; pp. 263–280.

(61) Lohmar, J.; Meyer, K.; Goldbach, G. Makromolekulare Chemie-Macromolecular Chemistry And Physics **1988**, 189, 2053–2065.

(62) Sauer, B. B.; Mclean, R. S.; Gaymans, R. J.; Niesten, M. C. J. E. *Journal of Polymer Science: Part B: Polymer Physics* **2003**, *42*, 1783–1792.

(63) Biemond, G.; Feijen, J.; Gaymans, R. J. *Journal of applied polymer* **2007**.

(64) Niesten, M. C. E. J.; Feijen, J.; Gaymans, R. J. *Polymer* **2000**, *41*, 8487–8500.

(65) Van Der Schuur, M.; Gaymans, R. J. *Journal of Polymer Science Part A: Polymer Chemistry* **2006**, *44*, 4769–4781.

(66) Rosen, S. L. *Fundamental Principles of Polymeric Materials*; 2nd ed.; Wiley-Interscience: New York, 1993; p. 88.

(67) Yilgor, E.; Yilgor, I. *Polymer* **2001**, *42*, 7953–7959.

(68) Seguy, I.; Jolinat, P.; Destruel, P.; Farenc, J.; Mamy, R.; Bock, H.; Ip, J.; Nguyen, T. P. *Journal of Applied Physics* **2001**, *89*, 5442.

(69) Schmidt-Mende, L.; Fechtenkötter, A.; Müllen, K.; Moons, E.; Friend, R. H.; MacKenzie, J. D. *Science (New York, N.Y.)* **2001**, *293*, 1119–22.

(70) Lehmann, M.; Kestemont, G.; Gómez Aspe, R.; Buess-Herman, C.; Koch, M. H. J.; Debije, M. G.; Piris, J.; de Haas, M. P.; Warman, J. M.; Watson, M. D.; Lemaur, V.; Cornil, J.; Geerts, Y. H.; Gearba, R. I.; Ivanov, D. A. *Chemistry - A European Journal* **2005**, *11*, 3349–3362.

(71) Dimitrakopoulos, B. C. D.; Malenfant, P. R. L. **2002**, 99–117.

(72) Ungar, G. *Polymer* **1993**, *34*, 2050–2059.

(73) Bassett, D. C.; Turner, B. *Nature* **1972**, *240*, 146–148.

(74) Ungar, G.; Keller, A. *Polymer* **1980**, *21*, 1273–1277.

(75) Lovinger, A. J.; Furukawa, T.; Davis, G. T.; Broadhurst, M. G. *Polymer* **1983**, *24*, 1225–1232.

(76) Weeks, J. J.; Eby, R. K.; Clark, E. S. *Polymer* **1981**, *22*, 1496–1499.

(77) Godovsky, Y. K.; Makarova, N. N.; Papkov, V. S.; Kuzmin, N. N. *Die Makromolekulare Chemie, Rapid Communications 6*, 443–450.

(78) Godovsky, Y. K.; Papkov, V. S. **1989**.

(79) Lovinger, A. J.; Schilling, F. C.; Bovey, F. A.; Zeigler, J. M. *Macromolecules* **1986**, *19*, 2657–2660.

(80) Frey, H.; Out, G. J. J.; Moeller, M.; Greszta, D.; Matyjaszewski, K. *Macromolecules* **1993**, *26*, 6231–6236.

(81) Kojima, M.; Kluge, W.; Magill, J. H. *Macromolecules* **1984**, *17*, 1421–1425.

(82) Yamagishi, T.; Fukuda, T.; Miyamoto, T.; Takashina, Y.; Yakoh, Y.; Watanabe, J. *Liquid Crystals* **1991**, *10*, 467–473.

(83) Watanabe, J.; Ono, H.; Uematsu, I.; Abe, A. *Macromolecules* **1985**, *18*, 2141–2148.

(84) Ivanov, D. A. In *Polymer Science:A Comprehensive Reference*; K, M.; M, M., Eds.; Elsevier B.V.: Amsterdam, 2012; Vol. 1, pp. 227–258.

(85) Morkved, T. L.; Lu, M.; Urbas, A. M.; Ehrichs, E. E.; Jaeger, H. M.; Mansky, P.; Russell, T. P. *Science* **1996**, *273*, 931–933.

(86) Grigorova, T.; Pispas, S.; Hadjichristidis, N.; Thurn-Albrecht, T. *Macromolecules* **2005**, *38*, 7430–7433.

(87) Kim, S. H.; Misner, M. J.; Xu, T.; Kimura, M.; Russell, T. P. *Advanced Materials* **2004**, *16*, 226–231.

(88) Ryu, D. Y.; Shin, K.; Drockenmuller, E.; Hawker, C. J.; Russell, T. P. *Science (New York, N.Y.)* **2005**, *308*, 236–9.

(89) Son, J. G.; Bulliard, X.; Kang, H.; Nealey, P. F.; Char, K. *Advanced Materials* **2008**, *20*, 3643–3648.

(90) Hammond, M. R.; Mezzenga, R. *Soft Matter* **2008**, *4*, 952.

(91) Schneider, A.; Zanna, J.-J.; Yamada, M.; Finkelmann, H.; Thomann, R. *Macromolecules* **2000**, *33*, 649–651.

(92) Yang, J.; Piñol, R.; Gubellini, F.; Lévy, D.; Albouy, P.-A.; Keller, P.; Li, M.-H. *Langmuir : the ACS journal of surfaces and colloids* **2006**, *22*, 7907–11.

(93) Albrecht, K.; Mourran, A.; Zhu, X.; Markkula, T.; Groll, J.; Beginn, U.; de Jeu, W. H.; Moeller, M. *Macromolecules* **2008**, *41*, 1728–1738.

(94) Chen, H.-L.; Lu, J.-S.; Yu, C.-H.; Yeh, C.-L.; Jeng, U.-S.; Chen, W.-C. *Macromolecules* **2007**, *40*, 3271–3276.

(95) Chao, C.; Li, X.; Ober, C. *Pure and applied chemistry* **2004**, *76*, 1337–1343.

(96) Chuang, W.-T. W.; Sheu, H. H.-S.; Jeng, U.-S.; Wu, H.-H.; Hong, P.-D.; Lee, J.-J. *Chemistry of Materials* **2009**, *21*, 975–978.

CHAPTER 2. EXPERIMENTAL

This chapter introduces the main experimental techniques employed in this work. These include direct-space techniques such as Polarized Optical Microscopy (POM), Atomic Force Microscopy (AFM), Scanning Electron Microscopy (SEM) as well as reciprocal-space techniques such as Electron Diffraction, Wide- and Small-Angle X-ray scattering using the conventional and micro-focus beam. The complementarity and adequacy of these techniques to studies of semicrystalline and liquid-crystalline polymers will be specifically addressed. The technical part is followed by a section describing characterization of the nanoporous templates used to induce the orientation in the thin polymer films.

2.1. Differential Scanning Calorimetry (DSC)

Differential Scanning Calorimetry (DSC) is the most common thermal analysis technique employed in polymer science. The method of the so-called heat-flux DSC relies on the difference in heat fluxes between a sample and reference as a function of temperature. This difference appears when the heat is absorbed or released by the sample due to thermal events such as melting, crystallization, chemical reactions, polymorphic transitions, vaporization and others. Specific heat capacity and its changes during transitions, which are not associated with enthalpy variation such as the glass transition, can be also determined by this technique.

The main advantage of DSC is that it is a fast and convenient tool to measure the temperatures and transition enthalpies in order to determine the phase diagram of the system and to study the kinetics of transitions as a function of heating/cooling rates or as a function of time.

A Mettler-Toledo DSC 1, Perkin Elmer Pyris 1 and Netzsch DSC 404 instruments were used in this work. The calibrations were done with the standard samples of pure metals such as In and Zn; the sample chamber was kept under a constant flux of nitrogen. Inside a sealed aluminum pan, typically samples of 5-10 mg was used for measurements. Special care was taken as to the choice of the thermal history of the samples and heating rates to be used.

2.2. Direct space techniques: microscopy

2.2.1. Polarized Optical microscopy (POM)

Optical microscopy is a routine tool for investigation of the semicrystalline and liquid-crystalline (LC) morphology. In transmission geometry, the light from the condenser lens passes through the sample. Then the image is magnified by the system of objective lens. According to the Rayleigh criterion, the resolution in visible light is limited to 0.5 μm. In polarized optical microscopy (POM) the birefringence of the material is used to discriminate the different morphological features.

In this work, POM observations have been carried out with the help of an Olympus BX51 Microscope equipped with Olympus DP70 digital color camera.[1] The camera employs a single-chip charge-coupled device (CCD) sensor with Bayer RGB primary color filtration. The two-thirds-inch CCD chip incorporates 1.45 million effective pixels, which can be piezo-shifted during image acquisition to obtain a maximum effective resolution of 12.5 mega

pixels. The time and interval variables can be changed with the camera-user interface, which allows a series of images to be captured. The microscope was used in both reflection and transmission mode. To study the phase transitions of the semicrystalline/LC materials as a function of temperature the microscope was equipped with a Mettler heating stage.[2]

2.2.2. Atomic Force Microscopy (AFM)

Since the invention of Scanning Tunneling Microscope (STM) by G. Binning *et al.* in 1981, a series of different modifications of Scanning Probe Microscopes (SPMs) has been developed. Among the large family of the SPMs, the most popular technique is Atomic Force Microscopy (AFM). The AFM success is due to the relatively simple handling, high magnification (the resolution can be at the nanometer scale), rather rapid measurements, no particular exigency for the sample preparation, possibility of imaging at different conditions as high temperature, controlled atmosphere and pressure. Taking into account these capacities, AFM represents itself as an efficient alternative to optical and electron microscopy. Furthermore, nowadays AFM is not limited to topography visualization, but provides access to roughness, adhesion, mechanical, electric and magnetic properties.

The basic principle and major components of AFM are illustrated in **Figure 2.1** (left). For imaging, a sharp tip assembled at the extremity of a miniature cantilever rasters the sample surface. When the tip approaches the surface it feels either repulsive or attractive forces of physical (or chemical) nature. These forces on the order of nano-Newtons cause the horizontal and vertical deflections of the cantilever which are transmitted to a position-sensitive photo-diode using a laser beam bouncing from the cantilever backside. A piezo-electric scanner allows performing the scan of the sample surface in the sub-nanometer range by moving along x and y-axes. The height values recorded at each point are converted to the topographic image matrix or other format. It is noteworthy, for very flat specimens with periodic lattice, e.g. mica, the true atomic resolution could be in principle achievable.[3] AFM can be used in different modes such as contact mode, Tapping-mode or non-contact mode.

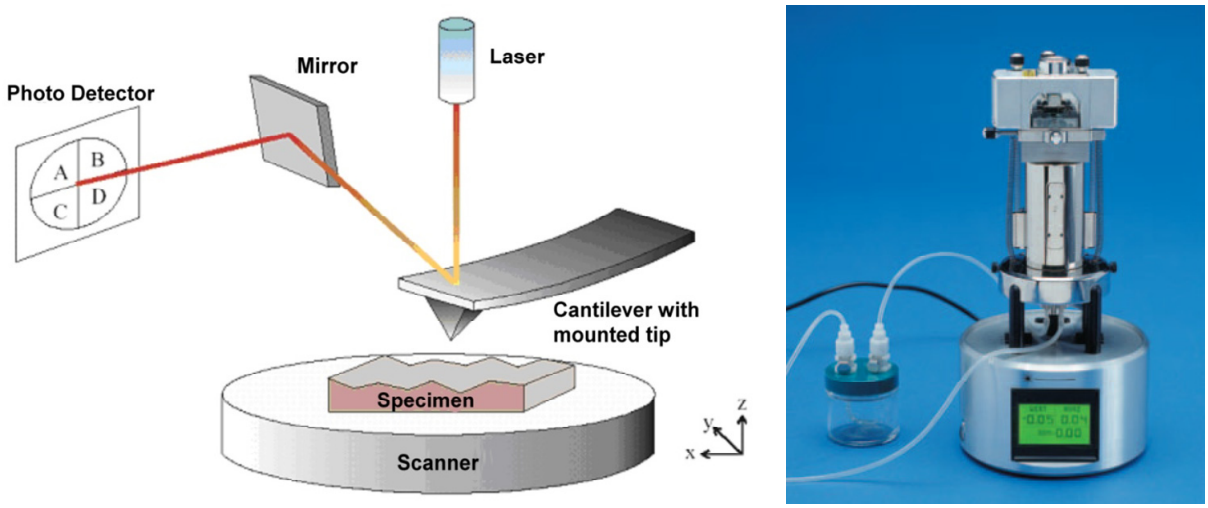

Figure 2.1. Scheme with the principal components of AFM method (right) and the MultiMode (Bruker AXS) microscope (left).

For soft-matter samples, the contact mode is not very useful as it often results in the sample deformation/destruction. Therefore, an intermittent-contact also known as Tapping-Mode (TM-AFM) is more suitable and was used throughout in our experiments. This method was developed in the early 90's by Digital Instruments company in order to extend AFM measurement capacity on the polymeric and biological samples. In TM-AFM the probe is oscillated above the sample surface close to its resonance frequency, and hence the contact with the sample is very short and the forces exerted on sample are mainly normal to its surface. Three different signals can be monitored simultaneously during imaging: topography, phase and amplitude. For proper scanning, the tip should have sufficient vibration energy to overcome the attractive tip-sample forces, in other words, to prevent it to be stuck, for instance, in a thin water layer covering the specimen surface. It was found that the TM-AFM phase signal is sensitive to property changes of the material such as composition, friction, adhesion and viscoelasticity.

In the present work, TM-AFM measurements were performed using a commercial MultiMode instrument equipped with a Nanoscope IV controller (Bruker AXS[4]) shown in **Figure 2.1**. The probes were standard commercial rectangular shape silicon cantilevers produced by Nanosensors with typical force constant of 21-98 N/m and resonant frequencies of 146-236 kHz.

2.2.3. Transmission Electron Microscopy (TEM) and Selected-area Electron Diffraction (SAED)

The scheme of a Transmission Electron Microscope can be represented as a three-lens system, i.e. a combination of an objective lens, intermediate lens and projector lens. The principle of the image formation through them is depicted in **Figure 2.2**a-b. The condenser lenses used in the illumination system are not shown in the sketch. The objective lens generates a diffraction pattern in the back focal plane by the scattered electrons and combines them to form an image in the image plane. Therefore, the TEM is capable to combine the imaging mode with the diffraction mode. In direct space, only the bright field imaging mode was used in which the image of a thin sample is formed by the unscattered electrons passing through the film without diffraction, the diffracted electrons being stopped by the objective aperture (**Figure 2.2**a). The image contrast is entirely owing to the electrostatic charge density variations in the sample. For the reciprocal space observations (selected area diffraction mode), the second aperture determines the area of which the diffraction is obtained (**Figure 2.2**b). The diffraction pattern can give information on the atomic structure of the sample. The passage between two modes is easily achieved by varying the strength of the intermediate lens.

SAED is similar to X-ray diffraction but has a disadvantage to be destructive for many organic systems such as bis-oxalamide based pre-polymers, which were studied in this work. An example of the beam damage for the case of a needle-like as bis-oxalamide crystal is presented in **Figure 2.3**. It can be seen that its shape has become curvy under the beam, and the corresponding diffraction pattern starts to be visibly modified, *i.e.* the peaks broaden in the azimuthal direction due to deformation of the sample. It is noteworthy that in order to detect the transmitted beam the thickness of an organic sample can hardly exceed 100 nm.

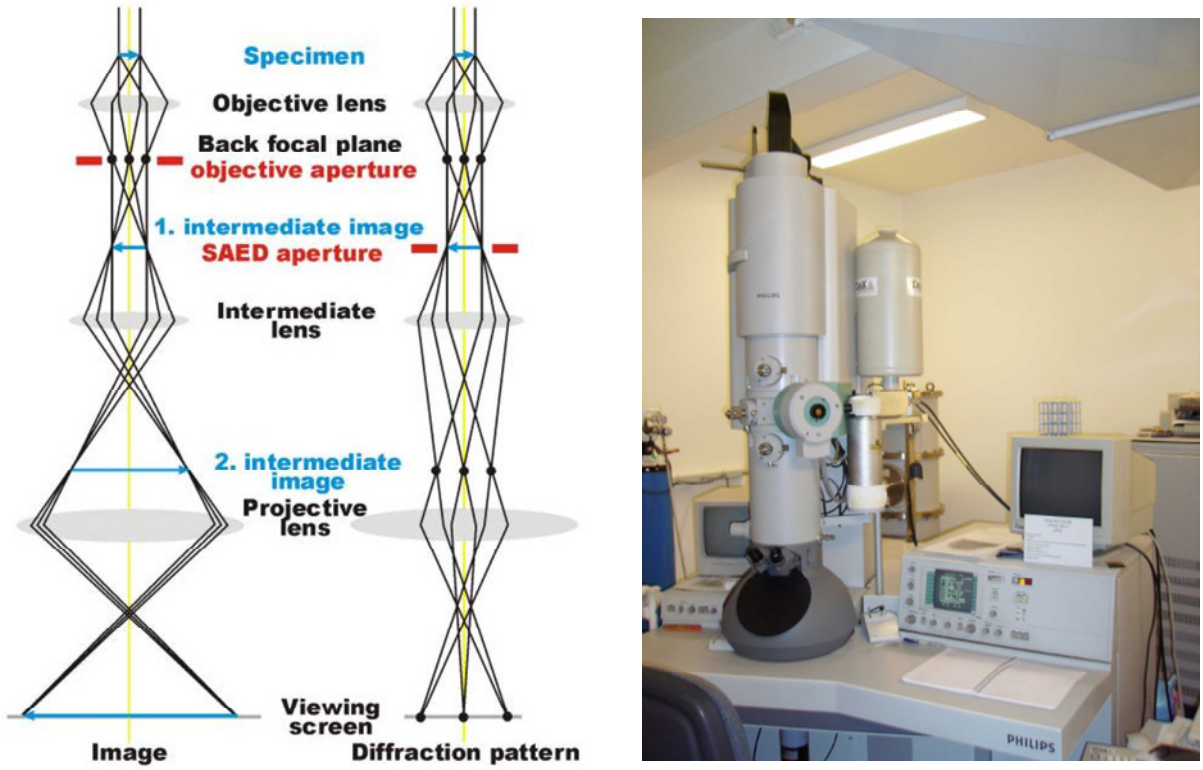

Figure 2.2. Optical scheme of a transmission electron microscope. (a) Imaging mode. (b) Selected area diffraction mode.[5] (c) Photo of Philips CM200 TEM.

In this study the experiments were performed with a Philips CM200™ Transmission Electron Microscope (cf. **Figure 2.2**c) equipped with a lanthanum hexaboride filament. The acceleration voltage was 200 kV. The samples were prepared by precipitation from toluene on a glass slide followed by floating the sample in 1% hydrofluoric acid aqueous solution. The samples were collected on the gold TEM-grids.

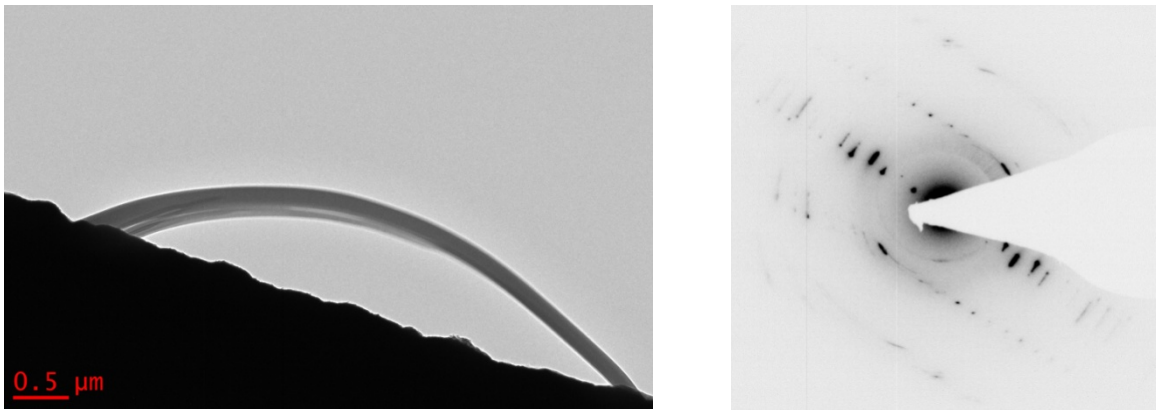

Figure 2.3. Bright field image of Gly-Oxa$_2$4-Gly pre-polymer deposited on a gold TEM-grid (left) and corresponding SAED pattern (right).

2.2.4. Scanning Electron Microscopy (SEM)

In Scanning Electron Microscope the accelerated electrons are focused on a narrow spot on the sample surface to be analyzed. The interaction between the sample and the electron beam generates secondary electrons of a low energy that are subsequently amplified and detected. The intensity of the signal is relevant to the nature of the material and the sample topography. The image of the surface is obtained by rastering it with the beam.

The FEI Quanta 400™ microscope outfitted with a tungsten filament was used.[6] The measurements were carried out at the acceleration voltage of 30 kV. The samples were coated with gold by high-vacuum evaporation to ensure conductivity of the surface.

2.3. Reciprocal space techniques: X-Ray scattering

The advantages of reciprocal-space X-ray scattering measurements are usually attributed to the rapidity of the measurements (modern detectors can operate on the millisecond scale), possibility to address bulk samples and to the in-situ monitoring of the sample structure. Last but not least, the X-ray techniques are known to be rather universal, and not exigent in terms of the sample preparation.

In this work, X-ray diffraction experiments were performed using our home facility (SAXS/WAXS system), as well as synchrotron radiation sources at the European Synchrotron Radiation Facility (ESRF, Grenoble) and the National Synchrotron Light Source (NSLS, Brookhaven National Laboratory, Upton, USA).

2.3.1. Wide- and Small-Angle X-ray Scattering (SAXS/WAXS) using synchrotron radiation

Schematic representation of a synchrotron is shown in **Figure 2.4**.[7] In contrast to conventional in-house X-ray machines for which the X-rays are produced by decelerating electrons in the anode material e.g. copper, the synchrotron radiation is generated by deflecting the trajectory of relativistic electrons in a static magnetic field.

Thus, the electrons emitted by an electron gun are first accelerated in a linear accelerator (linac) and subsequently guided in an accelerator ring (booster) to reach their final energy. The latter is approximately 6 GeV for the ESRF and 2.5 GeV for NSLS. When the final energy is achieved the electron pulses are injected in the large storage ring, where they circulate under high vacuum for several hours. Whilst moving in the storage ring the electrons pass through different types of magnets: bending magnets, wigglers and undulators.

The wigglers are focusing magnets used to maintain the cross-sectional shape of the electron beam. The synchrotron radiation is produced in the bending magnets and undulators by changing the electrons trajectory. The emitted photons leaving the storage ring at specific places are guided to the tangentially aligned beamlines. The latter consist of three main parts comprising the optics, experimental and control sections (see **Figure 2.5**).

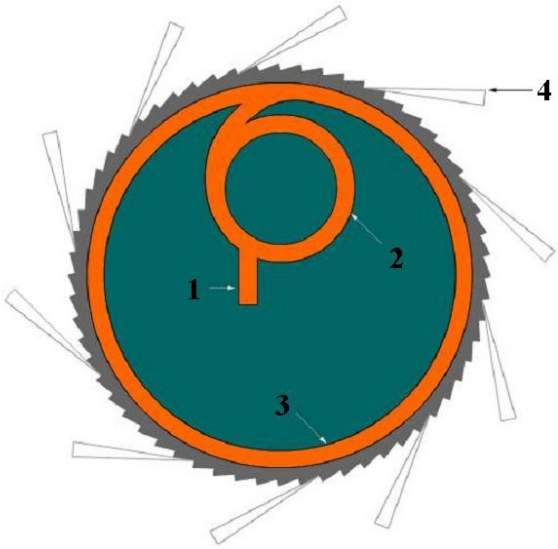

Figure 2.4. Main parts of a reference synchrotron: 1. linear accelerator; 2. accelerator ring; 3. storage ring; 4. beamline.

In the optical hutch the synchrotron beam is tailored for the experimental conditions in energy, flux and size. Then the "shaped" beam is transferred to the experimental hutch, where the sample environment and data collecting systems are situated.

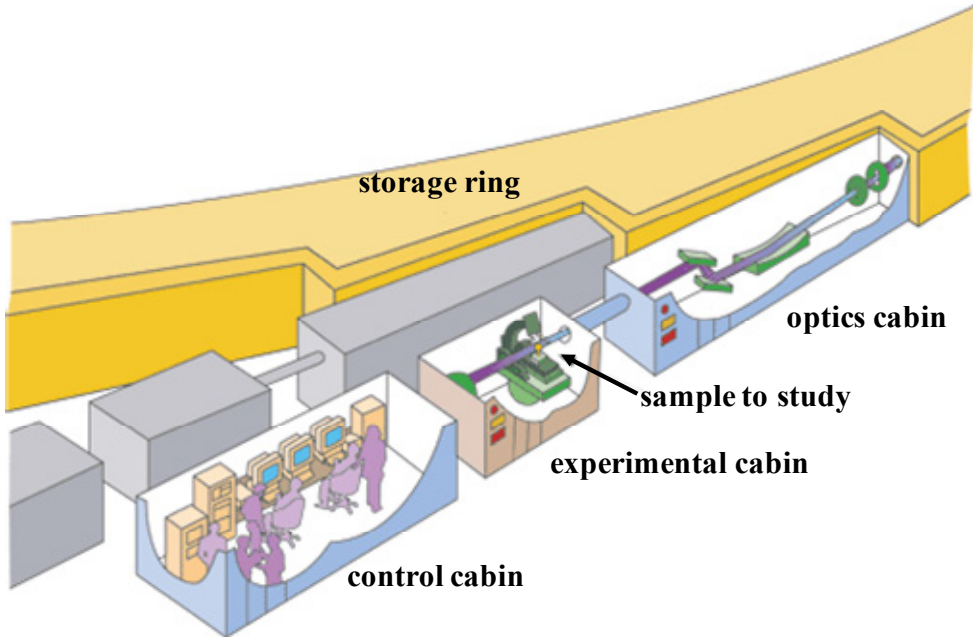

Figure 2.5. Cartoon of the layout of a common beamline at the ESRF.[7]

BM26B at the ESRF

The X-ray beam at the BM26B beamline[7] (cf. **Figure 2.6**a) is generated by a bending magnet. Once produced, the X-ray beam travels through a first slit of a Si (111) double-

crystal monochromator, followed by a meridionally focusing mirror, two further slits, before reaching the sample at about 47 meters from the source.

The *FReLoN 2000*™ CCD camera fabricated by the ESRF Instrument Support Group has dimensions of 10.2x10.2 cm^2 and spatial resolution of 50 μm. It was mainly used for WAXS measurements. Recently, a new generation ultralow-noise Pilatus 1M™ (16.9 x 17.9 cm^2)/Pilatus 300K-W™ (25.4 x 3.4 cm^2) detectors from Dectris, with the counting rate of more than $2 \cdot 10^6$ photons/sec/pixel and pixel size of 172 x 172 μm,^{2} have became available. The Pilatus 300K-W camera can be mounted in front of the scattered beam, above the entry of the SAXS tube, allowing simultaneous acquisition of the small- and wide-angle patterns (**Figure 2.6**a). Since different setups were used in our work, they will be discussed in more detail in the experimental part of the corresponding chapters.

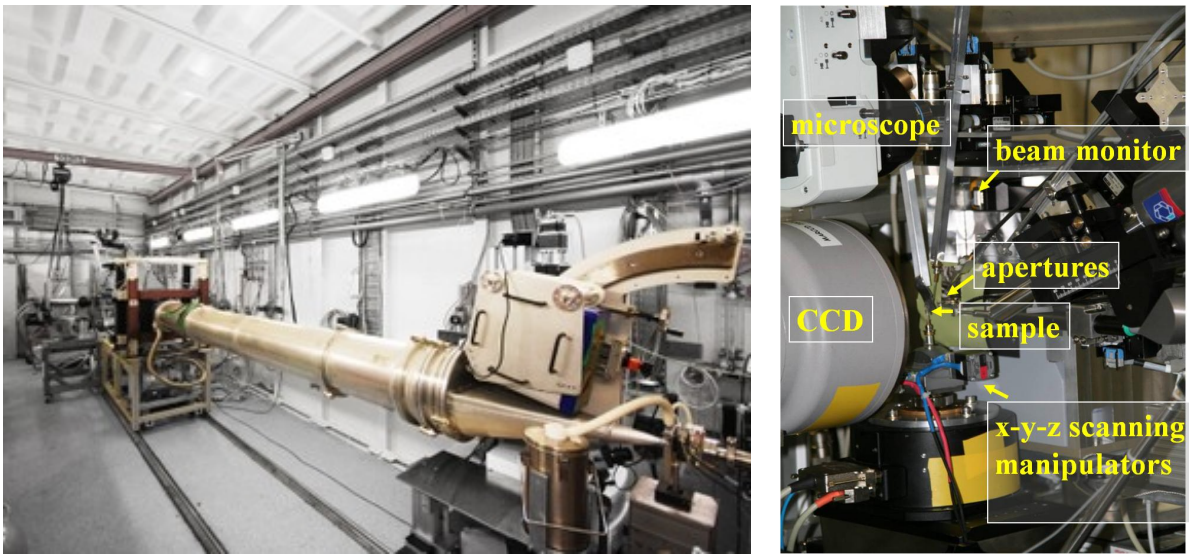

Figure 2.6. Experimental hutch at the BM26B beamline showing the installation for SAXS/WAXS simultaneous acquisition (left) and the setup for the microfocus scanning WAXS measurements at the ID13 beamline (right) at the ESRF.

ID13 at the ESRF

The ID13 micro-focus beamline[7] (cf. **Figure 2.6**b) is characterized by a high brilliance due to the undulator source of the X-ray beam. The monochromatic X-ray beam is focused first by beryllium lenses. The crossed-Fresnel optics in combination with an extremely long focusing distance (up to 50 m) allows to obtain a high flux together with a small-divergence beam focused down to the sub-micron range along both axes.

For the scanning experiments, an x-y piezo motor can be used. It is noteworthy that since the lateral motion of the specimen requires high precision, the movable sample stage has to be extremely light and small to prevent overshooting during the stepwise motion.

An on-axis optical microscope installed downstream the sample is employed to navigate on the sample (see **Figure 2.6**b). Such setup makes it possible to obtain diffraction patterns of particular morphological features observed in the in-situ OM. The experiments were conducted with a *FReLoN*™ fast CCD with a pixel size of 50x50 μm^2 (not rebinned) and a 16-bit readout placed downstream the sample at variable distances allowing to select the desired scattering range for the experiment.

X6B beamline at the NSLS

This beamline is dedicated to the X-ray scattering, reflectivity and diffraction of soft- and bio-materials.[7,8] The energy of the X-rays generated with a bending magnet ranges from 6.5 to 19 keV. The optical system incorporates a channel-cut Si (111) monochromator located at a distance of 10 m from the source. The Rhodium-plated toroidal mirror located at *ca.* 11.3 m downstream subtends approximately 4.5 mrad horizontally and 0.33 mrad vertically for 1:1 focusing on the sample.

Our group was mainly working in GISAXS/GIWAXS setups using a Bruker Smart 1000™ CCD camera. Temperature measurements were carried out with an INSTEC heating stage HCS402 configured with a STC200 temperature controller operated under a liquid nitrogen flow. The views of the GIWAXS setup and sample stage are given in **Figure 2.7**.

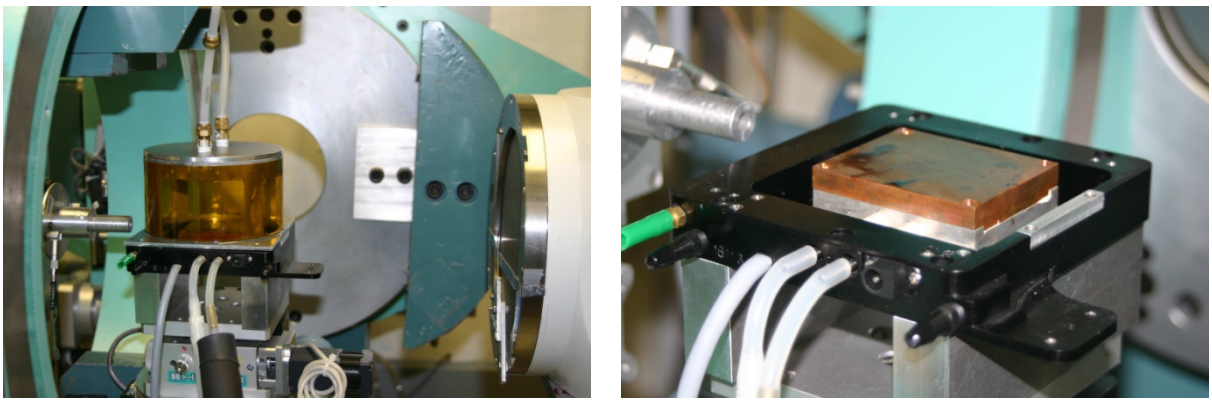

Figure 2.7. View of the GIWAXS setup (left) and sample stage (right) at the X6B beamline, NSLS, USA.

2.3.2. SAXS/WAXS system at the IS2M

An in-house custom-built SAXS/WAXS machine equipped with a Rigaku MicroMax™-007 HF[9] copper rotating anode is shown in **Figure 2.8**. The measurements were typically performed at 40 kV and 30 mA.

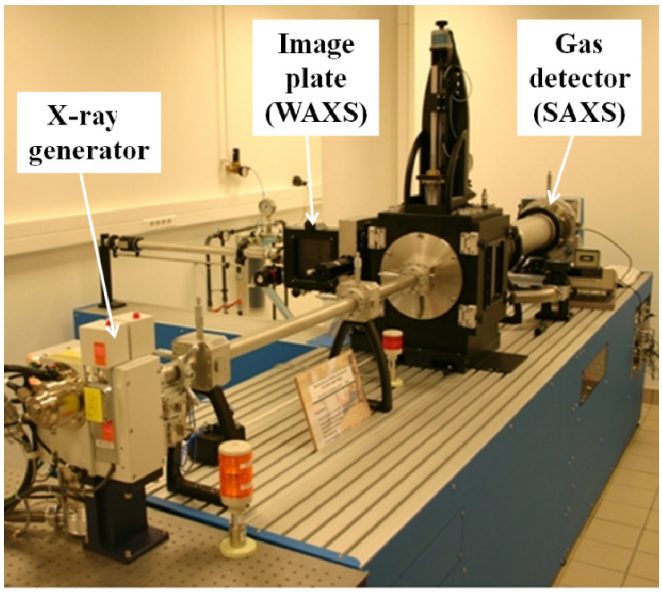

Figure 2.8. In-house SAXS/WAXS system with an image plate in wide-angles and a gas detector in small-angles region.

The optical system represents the high performance adjustable confocal mirrors Osmic™ VariMax™ and three pinholes. The first two pinholes define the beam size and divergence, and the third one cuts off the parasitic scattering. The resulting beam size was about 200 µm.

To collect the wide-angles patterns the X-ray sensitive Fuji image plate with a 100x100 µm^2 pixel size was used. The hole in the center of the image plates allows performing simultaneous SAXS and WAXS experiments. SAXS data were recorded with a gas-filled 2D multi-wire detector. A photodiode is mounted on the beamstop to perform the absolute intensity measurements.

All the SAXS/WAXS measurements were carried out in transmission under vacuum. A Linkam heating stage connected to a temperature controller and a liquid nitrogen pump allows changing specimen temperature in relatively broad range. The home-made sample holders were developed to study the structure of specimens in different geometries.

2.4. Materials

With regard to the systems studied in the frame of this work, one has to mention segmented poly(ether-ester-amide) (PEEA) copolymers, main-chain liquid-crystalline polymers belonging to the family of poly(di-*n*-alkylsiloxanes) and liquid-crystalline/semicrystalline block copolymers formed through complexation of poly (2-vinylpyridine-b-ethylene oxide) (P2VP-PEO) with a wedge-shaped ligand, 4′-(3′′,4′′,5′′-tris(octyloxy) benzamido) propanoic acid. The details of synthesis and sample preparation for each of these materials will be given in the corresponding chapter. Though, in this section we

will focus only on the nanoporous templates used to study the structure formation under conditions of 1D confinement.

2.5. Characterization of the Nanoporous Templates

Commercially-available alumina membranes with the nanometer pore sizes were supplied by Whatman and Smart Membranes.[10] The SEM images show the well-defined honeycomb pore structure of the template with three pore sizes of 35, 80 and 200 nm (cf. **Figure 2.9**). However, the SAXS experiments probing the bulk structure can disclose the difference in the pore ordering for various membranes. 2D SAXS pattern from membrane with 80 nm pores shows multiple oriented scattered maxima in **Figure 2.10**a. 1D equatorial intensity profile obtained by integration of 2D diffractogram was indexed suggesting hexagonal packing of the pores with the inter-pore distance of 106 nm (cf. **Figure 2.10**b). The diffuse scattering on 2D SAXS pattern from membrane with the big pore size (200 nm) gives evidence of significantly weaker pores correlation in comparison to that of the template with 80 nm pores (**Figure 2.10**c).

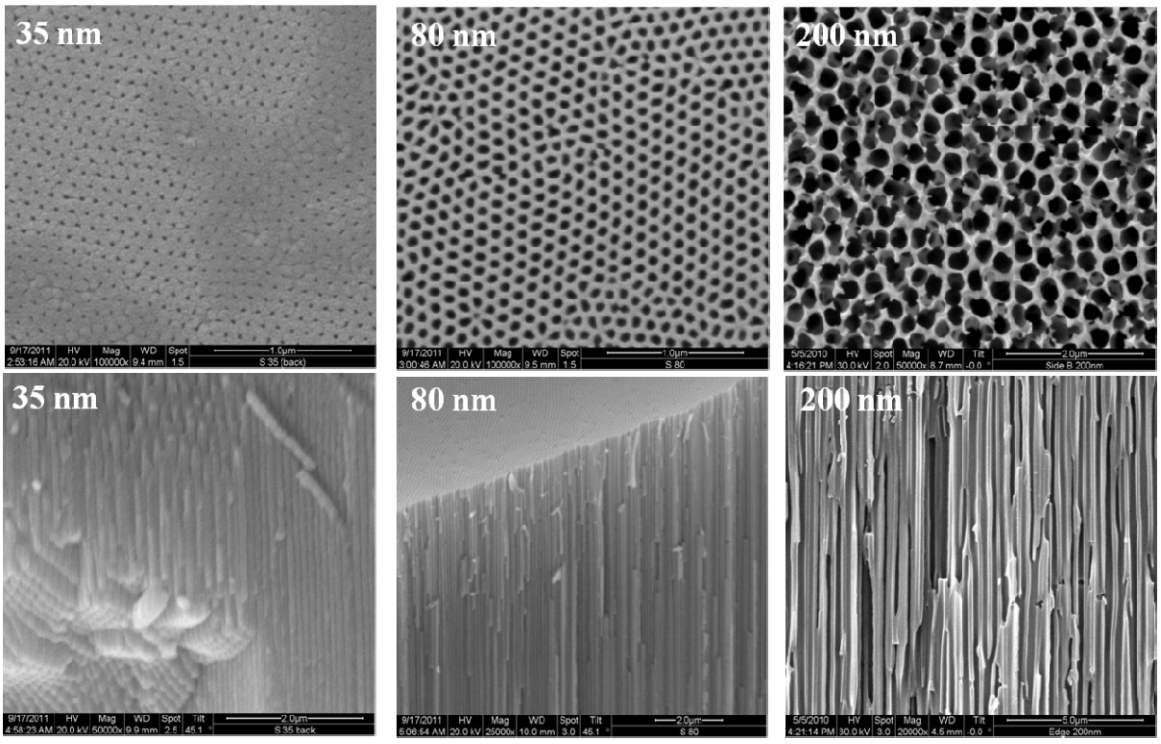

Figure 2.9. Surface (top) and lateral (bottom) view of well-defined honeycomb pore structure of the templates. The pore sizes are marked on the graph.

For our study, it was mainly the pore size, which was crucial. It is this parameter that allowed us to clearly observe the confinement effect on the orientation of the LC polymers which will be discussed in detail in Chapter 5.

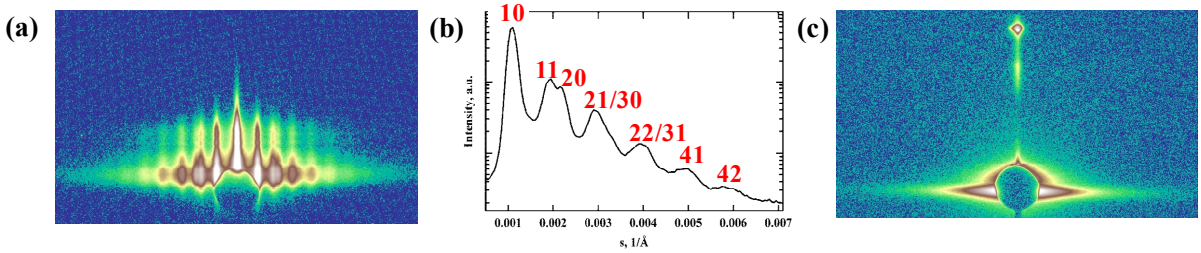

Figure 2.10. 2D SAXS pattern obtained in transversal direction for the templates with 80 nm (a) and 200 nm (c) pore sizes. (b) 1D SAXS equatorial profile extracted from image (a).

2.6. References

(1) Olympus general and technical information (www.olympus.com).

(2) Mettler Toledo general and technical information (www.mt.com).

(3) Klinov, D.; Magonov, S., *Appl. Phys. Lett.* **2004***, 84*, 2697-2699.

(4) Bruker technical information (http://www.bruker-axs.com/atomic-force-microscopes.html).

(5) http://www.microscopy.ethz.ch/TEMED.htm

(6) FEI technical datasheet (www.fei.com).

(7) ESRF and NSLS general and technical information (www.esrf.eu, www.nsls.bnl.gov).

(8) Huang, K. G.; Ramanathan, M.; Montano, P. A. *Review of Scientific Instruments* **1995**, *66*, 1688.

(9) Rigaku, technical information (www.rigaku.com).

(10) Whatman and Smart Membranes general and technical information (www.whatman.com, www.smartmembranes.de).

CHAPTER 3. MORPHOLOGY AND PROPERTIES OF SEGMENTED POLY(ETHER ESTER AMIDE)S COMPRISING UNIFORM GLYCINE OR β-ALANINE EXTENDED BISOXALAMIDE HARD SEGMENTS

Yaroslav I. Odarchenko[a], Martin Rosenthal[a], Niels J. Sijbrandi[d], Ad J. Kimenai[b], Edwin P.C. Mes[b], René Broos[b], Georg Bar[c], Jan Feijen[d] and Pieter J. Dijkstra[d], Dimitri A. Ivanov[a]

[a]Institut de Sciences des Matériaux de Mulhouse-IS2M, CNRS LRC 7228, Jean Starcky, 15, F-68057 Mulhouse, France

[b]Core R&D, Dow Benelux BV, P.O. BOX 48, 4530 AA Terneuzen, The Netherlands

[c]Dow Olefin Verbund GmbH, P.O. Box 1163, D-06258, Schkopau, Germany

[d]Department of Polymer Chemistry and Biomaterials, MIRA Institute for Biomedical Technology and Technical Medicine, Faculty of Science and Technology, University of Twente, P.O. Box 217, 7500 AE Enschede, The Netherlands

Highly phase-separated segmented poly(ether ester amide)s comprising glycine or β-alanine extended bisoxalamide hard segments were studied. These thermoplastic elastomers with molecular weights, M_n, exceeding $30x10^3$ $g{\cdot}mol^{-1}$ are conveniently prepared by polycondensation of preformed bisester-bisoxalamides and commercially available PTHF diols. FTIR revealed strongly hydrogen-bonded and highly ordered bisoxalamide hard segments with degrees of ordering between 73 and 99 %. The morphology consists of fiber-like nano-crystals randomly dispersed in the soft polymer matrix. The micro-structural parameters of the copolymers were addressed by simultaneous small- and wide-angle X-ray scattering. It is shown that the crystals have strictly identical thickness, which is close to the contour length of the hard segment. The long dimension of the crystals is identified with the direction of the hydrogen bonds. The melting transitions of the hard segments are sharp, with temperatures up to 170 °C. The segmented copolymer comprising a β-alanine based bisoxalamide hard segment with a spacer of six methylene groups has a melting transition of 141 °C, which is higher than the melting transition of its glycine analogue (119 °C). The improved thermal properties of the first group of polymers is related to crystal packing of the β-alanine-based hard segments as compared to the packing of the hard segments comprising glycine ester groups.

3.1. Introduction

Segmented block copolymers consisting of alternating flexible soft segments and rigid hard segments are thermoplastic elastomers, TPEs.[1,2] As a result of their phase-separated morphology, these materials show elastomeric behavior at ambient temperatures and can be processed from solution or by heating the materials above the vitrification (in case of amorphous block copolymers) or melting point (in case of semi-crystalline block copolymers) of the hard domains. At ambient temperatures, the hard segments form rigid domains in a continuous matrix of soft segments.[3] These domains act as physical cross-links providing stiffness and strength to the material. The properties of these segmented block copolymers are significantly affected by the symmetry, nature of hydrogen bonding and size distribution of the hard segment.[4-18] Symmetrical and uniform hard segments in segmented copolymers can easily crystallize and high degrees of crystallinity of the hard block can be obtained. Consequently, copolymers with such segments usually have broad and temperature-independent rubbery plateaus, relatively high moduli and good ultimate mechanical properties.

Segmented block copolymers with uniform amide based hard segments have been previously prepared by Gaymans and coworkers.[12,19-33] The main two hard segments which have been used are the di-amide segment (TΦT) based on 1.5 repeating unit poly(p-phenylene terephthalamide) and the tetra-amide segment based on 2.5 repeating unit nylon-6,T (T6T6T). The corresponding segmented copolymers have been generally prepared by first purifying the aromatic amide group containing monomers and subsequently reacting these monomers with polyether prepolymers in a two-step solution/melt polymerization. Although the hard segments are relatively short, they crystallize fast and almost completely in the segmented copolymer. TEM and AFM analysis of these copolymers show a morphology of fiber-like nano-crystals randomly dispersed in a soft polymer matrix.[19,20,33] Even at a hard segment concentration of ~3 wt%, the polymers show a distinct phase separated morphology and hence good elastomeric and mechanical properties.[20,27]

In our previous work, we prepared fully-aliphatic segmented poly(ether amide)s based on uniform rigid oxalamide segments and flexible PTHF segments and studied their properties.[34] The copolymers comprising hard segments with two or three oxalamide units exhibit highly phase-separated morphology, which contributes to their mechanical performance. The oxalamide containing hard segments are strongly hydrogen bonded and highly ordered, forming fiber-like nano-crystals which are randomly dispersed in a soft polymer matrix. The

flow temperatures of bisoxalamide based segmented poly(ether amide)s increased from 150 to 200 °C when the number of methylene groups between the two oxalamide groups was decreased from 10 to 2, but the melting transitions remained very broad. Copolymers with three oxalamide groups in the hard segment had a flow temperature of 220 °C. The use of hard segments with either two or three oxalamide groups provided materials with attractive mechanical properties. Due to the high flow temperatures of the copolymers with three oxalamide groups in the hard segment, melt processing of these materials becomes difficult. Therefore, poly(ether amide)s composed of hard segments containing two oxalamide groups seem to give the optimum balance between the materials properties and processability.

The bisoxalamide based segmented poly(ether amide)s were previously prepared by first reacting bis(3-aminopropyl) end functionalized polytetrahydrofuran (PTHF) with an excess of diethyl oxalate.[34] Subsequently, the amide-ester capped PTHF soft segment was polycondensated in the melt with a linear aliphatic α,ω-diamine chain extender. Although the synthesis of these polymers is straightforward, α,ω-diamine end functionalized prepolymers are needed. In general, the commercial availability of such prepolymers is limited and/or they are relatively expensive. In contrast, a wide range of α,ω-hydroxyl end functionalized prepolymers (high molecular weight diols) are commercially available or synthetically easily accessible, some may have a renewable origin. Therefore, a more attractive strategy to prepare bisoxalamide based segmented block copolymers is the polycondensation of α,ω-hydroxyl end functionalized prepolymer soft segments with preformed OH reactive bisester-bisoxalamide hard segments.

To explore this new strategy, we have prepared segmented copolymers based on polytetrahydrofuran diol soft segments and hard segments containing two oxalamide groups, in which these groups are separated by spacers with different lengths. Moreover the hard segments were either terminated by a glycine or a β-alanine ester residue (industrial amino acids) to make those OH reactive. The molecular weight (M_n) of the soft PTHF segment was varied from 1.0×10^3 to 2.9×10^3 g·mol^{-1}. The influence of the structure of the hard segment and the M_n of the soft PTHF block on the properties of the resulting copolymers was evaluated.

3.2. Experimental

3.2.1. Materials

The synthesis and characterization of the bisester-bisoxalamide monomers and corresponding segmented poly(ether ester amide)s (PEEAs) are described elsewhere.[35] Compression molded bars (75×10×2 mm) were prepared using a hot press (THB 008, Fontijne Holland BV, the Netherlands). Polymers were heated for 4 min at approximately 20 °C above their T_{flow}, pressed for 3 min at 300 kN, and cooled in approximately 5 min under pressure to room temperature.

3.2.2. Methods

Fourier transform infra-red spectra (FTIR). To minimize the potential oxidation of the material, sample preparation comprised the following steps. The surface of a 32×3 mm NaCl disc (Thermo, International Crystal Labs) was roughened to prevent interfering fringes. Subsequently, a polymer solution of 0.3-0.5 $g \cdot ml^{-1}$ in dichloromethane was drop casted on the NaCl disk and the solvent was allowed to evaporate. This step was repeated until the polymer film thickness gave a maximum peak height of 0.5 - 0.7. The holder was placed in the cell in an inert atmosphere (N_2 purge glove bag or N_2 purged IR sample compartment). The cell was heated to 20-50 °C above the T_m of the polymer and subsequently cooled to room temperature. Fourier transform infra-red spectra were recorded on a Thermo 5700 spectrometer utilizing a DTGS detector at 4 cm^{-1} resolution. The temperature of the prepared polymer film was controlled by an infra-red cell from Spectra Tech (model 0019-019). The data were collected between 4000 and 500 cm^{-1} (16 scans were acquired). All spectra were normalized to the 2860 cm^{-1} signal. The carbonyl region was analyzed quantitatively in terms of free, bonded and ordered amide structures by curve fitting (Omnic version 7.2) and following the guidelines of Meier *et al*.[36]

DSC was carried out using a Perkin-Elmer Pyris 1. Calibration was carried out with pure indium. Samples (5-10 mg) were heated from -100 to 200 °C at a rate of 20 $°C \cdot min^{-1}$, annealed for 5 min, cooled to -100 °C at a rate of 20 $°C.min^{-1}$, and subsequently heated from -100 to 200 °C at a rate of 20 $°C \cdot min^{-1}$. Melting (T_m) and crystallization (T_c) temperatures were obtained from the peak maxima, melting (ΔH_m) and crystallization (ΔH_c) enthalpies were determined from the area under the curve.

Thermal gravimetric analysis (TGA) was carried out with 5-10 mg samples under a nitrogen atmosphere in the 50-700 °C range at a heating rate of 10 °C·min^{-1}, using a Perkin-Elmer Thermal Gravimetric Analyser TGA 7.

AFM images were obtained using a MultiMode scanning probe microscope (SPM) (Veeco Metrology Group, Santa Barbara, CA) with a Nano-Scope IV controller running software version 5.12. The TESP probe used was 125 μm in length, had a tip radius of 8 nm and a force constant of 40 N·m^{-1}. A moderate tapping ratio of about 0.5 was applied in all measurements. Height and phase images were recorded at various magnifications. Samples were prepared by drop casting a 1 mg·ml^{-1} chloroform solution on a silicon waver. After evaporation, the sample was heated to 20 °C above the T_{flow} for 15 min and slowly cooled to room temperature.

WAXS and **SAXS** measurements were performed on the BM26 beamline of the ESRF (Grenoble, France) using the wavelength of 1.04 Å. The experimental setup comprised a FReLoN detector mounted on a motorized stage, which ensured adjustable sample-to-detector distance and allowed to record the signal in the ***s***-range (***s***=2sinθ/λ, where θ is the Bragg angle) from 0.01 to 0.5 Å^{-1}. The modulus of the scattering vector ***s*** was calibrated using several diffraction orders of silver behenate in both setups. The patterns were collected in transmission geometry. The sample temperature was controlled by a Linkam heating stage.

For the measurements on the monomers uniaxially oriented samples were placed in the heating stage, with their fiber axes perpendicular to the incident X-ray beam.

3.3. Results and discussion

3.3.1. Synthesis

The synthesis of symmetrical bisoxalamides **2a-c** and **3** capped with glycine ethyl ester or β-alanine ethyl ester groups is depicted in **Figure 3.1**. First, bisoxalamide precursors **1a-c** were prepared by reacting α,ω-diamine spacers with an excess of diethyl oxalate. The compounds were obtained in good yields after purification. The ^{1}H and ^{13}C NMR analysis of the crude products revealed the formation of small amounts of oligomers, which were removed by selective extraction with chloroform. Reaction of **1a-c** with glycine ethyl ester afforded the bisester-bisoxalamides **2a-c**. Similarly, **3** was prepared from **1c** upon reaction with β-alanine ethyl ester. The ^{1}H NMR spectra of the products revealed a high purity of **2a-c** and **3** by comparing the integral values of the glycine or β-alanine methylene protons with the

central methylene protons next to the amide groups. Side reactions, like the reaction of **2a** with glycine ethyl ester, were not observed as ^{13}C NMR spectral data showed no carbonyl peaks found at $\delta = 178$ characteristic of single amides.[37]

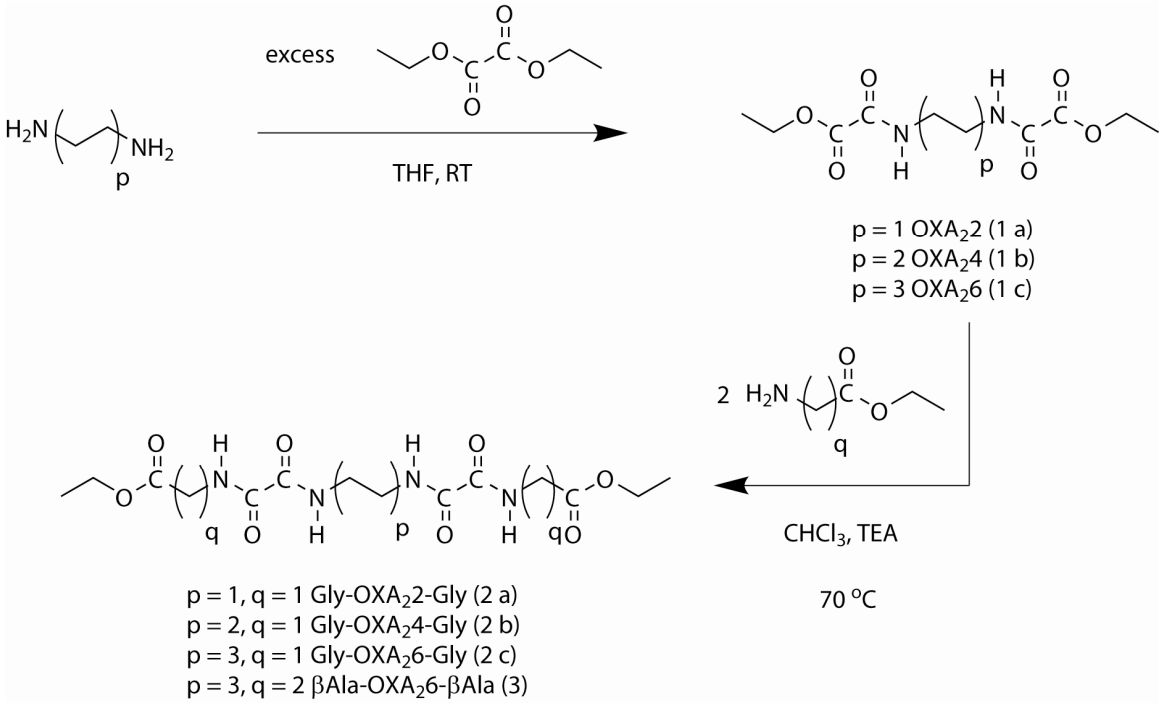

Figure 3.1. Synthesis of bisester-bisoxalamide monomers (2a-c, 3).

The segmented poly(ether ester amide)s were prepared by melt polycondensation of α,ω-hydroxyl end functionalized polytetrahydrofuran (PTHF diols) **4a-c** (1.0×10^3, 2.0×10^3 and 2.9×10^3 g.mol^{-1}) and bisester-bisoxalamides **2a-c** and **3** (**Figure 3.2**). The condensation reactions of PTHF-Gly-OXA$_2$6-Gly **(7a-c)** were performed at 250 °C and low pressure for 3 h. The polymers were obtained as yellow elastic transparent solids in high yields. To prevent thermal degradation, which was observed during polycondensation of PTHF$_{1000}$-Gly-OXA$_2$2-Gly **(5)** at 250 °C, the synthesis of polymers **5**, **6** and **8** was performed in a slightly different way. First, the reaction mixture was heated to a temperature of approximately 230 °C. When the melt was transparent, the temperature was decreased to 190 °C and the reaction was continued for 3 h at low pressure. Also these materials were obtained as transparent elastic solids and their color changed from yellow **(5)** to colorless for polymers **6** and **8**. ^1H NMR analysis revealed the absence of ethyl ester or hydroxyl end groups indicating relatively high molecular weights. GPC analysis confirmed molecular weight values between 34×10^3 and 83×10^3 g·mol^{-1} and polydispersity indices (PDI's) of 2-3 relative to polystyrene standards (**Table 3.1**). The somewhat higher PDI values for **7a-c** from GPC analysis may be ascribed to

the solubility of the polymers in a mixture of 1,1,1,3,3,3-hexafluoro-2-propanol and chloroform resulting in tailing towards the high molecular weight end.

Table 3.1. Molecular weights of segmented PEEAs **5-8**.

	Content*			
	Soft (wt%)	Hard (wt%)	M_n ($g \cdot mol^{-1} x\ 10^3$)	PDI (-)
$PTHF_{1000}$-Gly-$OXA_2$6-Gly **(7a)**	74.6	25.4	42	3.3
$PTHF_{2000}$-Gly-$OXA_2$6-Gly **(7b)**	85.5	14.5	62	2.7
$PTHF_{2900}$-Gly-$OXA_2$6-Gly **(7c)**	89.5	10.5	83	2.7
$PTHF_{1000}$-Gly-$OXA_2$2-Gly **(5)**	77.8	22.2	34	2.0
$PTHF_{1000}$-Gly-$OXA_2$4-Gly **(6)**	76.2	23.8	52	1.9
$PTHF_{1000}$-βAla-$OXA_2$6-βAla **(8)**	73.1	26.9	59	1.9

*The ester groups are included in the calculation of the hard segment content.

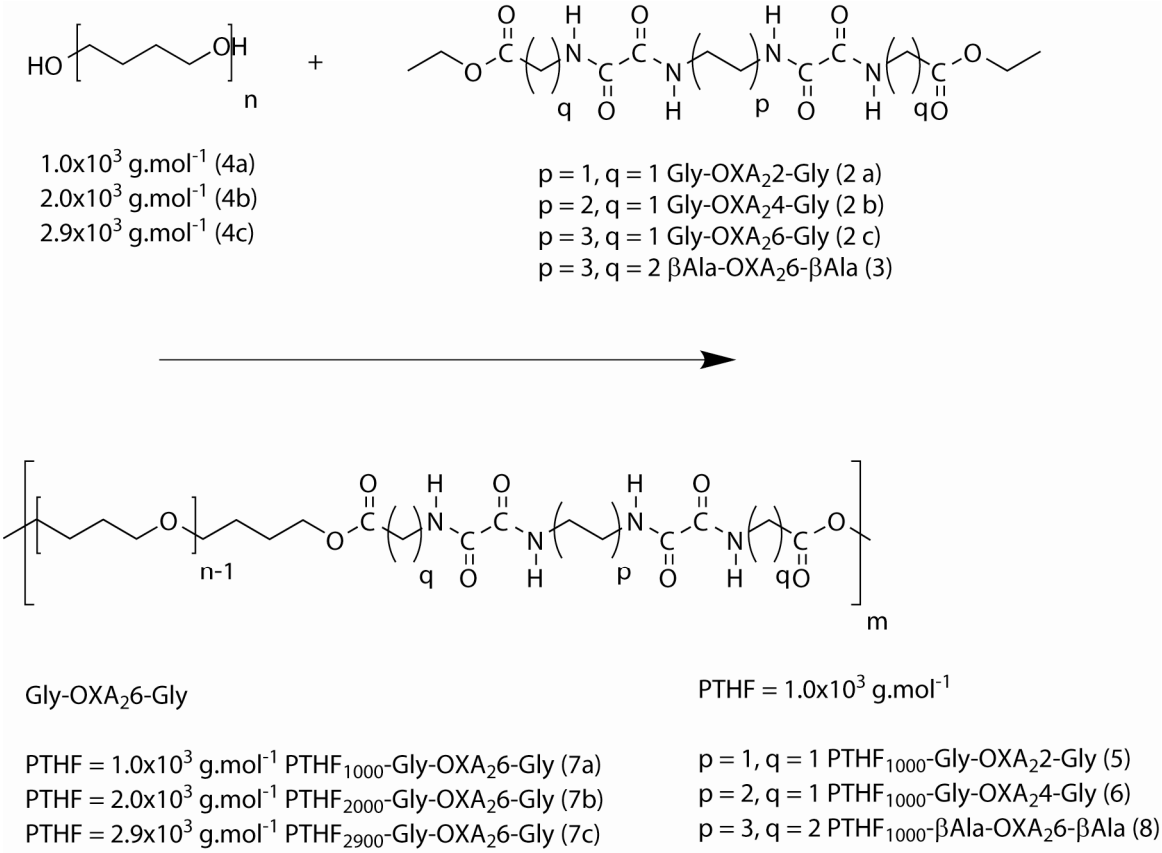

Figure 3.2. Synthesis of segmented poly(ether ester amide)s **5-8**.

3.3.2. FTIR

The FTIR spectra of the segmented PEEAs with varying hard segments **(5-8)** are presented for the selected wave number regions 3500-2700 and 1800-1400 in **Figure 3.3**. Characteristic IR bands are found at ~3295 (Amide A, ν N-H, H-bonded), 1736-1746 (ν C=O ester, non H-bonded), ~1650 (Amide I, ν C=O amide, H-bonded ordered), ~1530 cm^{-1} (Amide II, ν C-N + δ N-H).

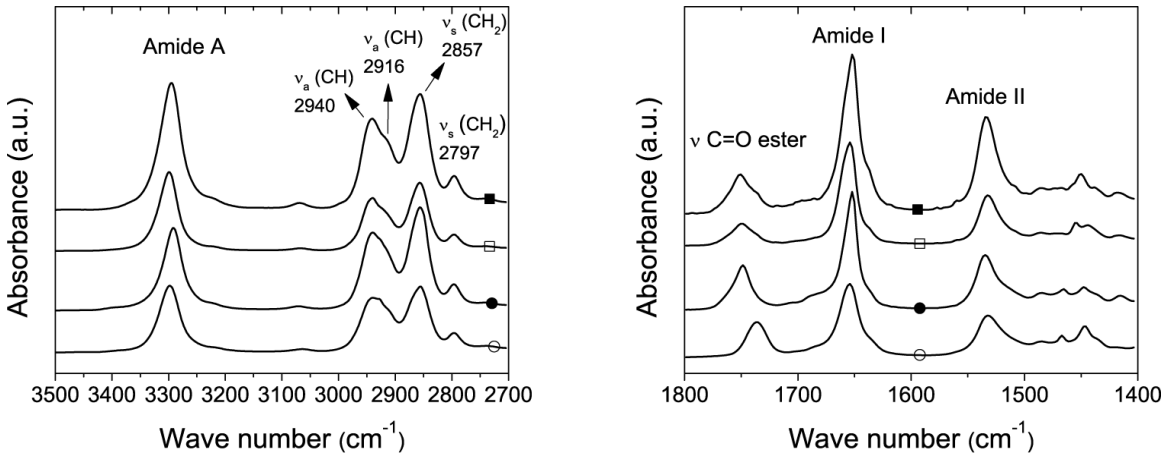

Figure 3.3. FTIR spectra of segmented poly(ether ester amide)s (■) $PTHF_{1000}$-Gly-$OXA_2$2-Gly at 40 °C **(5)**, (□) $PTHF_{1000}$Gly-$OXA_2$4-Gly at 30 °C **(6)**, (●) $PTHF_{1000}$-Gly-$OXA_2$6-Gly at 35 °C **(7a)** and (○) $PTHF_{1000}$-βAla-$OXA_2$6-βAla **(8)** at 50 °C.

For all polymers, the N-H and C=O stretching vibrations appear as sharp bands at 3295 and 1650 cm^{-1}, respectively. This indicates that the bisoxalamide segments in the polymers are highly ordered and strong hydrogen bonds are formed between the oxalamide groups. These observations suggest a high degree of phase separation and the presence of at least paracrystalline amide domains formed by association or stacking of bisoxalamide arrays. Importantly, the ester C=O stretching vibration band of the glycine **(5**, **6** and **7a)** and β-alanine **(8)** moieties in the segmented poly(ether ester amide)s are found at 1746 and 1736 cm^{-1}, respectively, indicative of non-hydrogen bonded ester groups. These wave numbers are similar to those found for the monomers **2a-c** and **3** and point to a similar crystalline structure of the monomer and the hard segments in the polymer.[35] Moreover, this observation suggests that the ester carbonyl groups are spatially tilted away from the oxalamide plane. The higher wave number of the glycine ester carbonyl compared to the β-alanine ester carbonyl vibration band is likely due to rotation of the former group into a more a-polar surrounding.

The amide II band, which is especially sensitive to polymorphism resulting from differences in chain conformation, like the α- or γ-crystalline structures of nylons, is located at

~1532 cm^{-1} for all four polymers. Previous research on segmented poly(ether amide)s with bisoxalamide hard segments showed a similar position of the amide II band for spacer lengths of 2 and 4 methylene groups, but this position shifted to ~1520 cm^{-1} for bisoxalamides with spacer lengths of 6 methylene groups and higher.[34] Higher wave numbers for bisoxalamide segments with decreasing spacer length can be attributed to increasing chain distortions and hence deviations from the fully extended zig-zag conformation. The amide II position of the segmented poly(ether ester amide)s with bisoxalamide segments having spacer lengths of 6 methylene groups is located at ~1532 cm^{-1}, whereas the amide II position of the corresponding segmented poly(ether amide) is found at a wave number of 1520 cm^{-1}. Apparently, the glycine and β-alanine ester groups induce a tilting of the oxalamide groups from a fully extended planar zig-zag conformation thereby shifting the amide II band to higher wave numbers

The effect of temperature on the extent of hydrogen bonding and organization of the hard segment was studied with temperature dependent FTIR. The N-H stretching vibration band and ester and amide C=O stretching vibration bands of $PTHF_{1000}$-Gly-$OXA_2$6-Gly **(7a)** at different temperatures are depicted in **Figure 3.4**. This polymer had a sharp melting transition between 105 and 135 °C (*vide infra*, Thermal Properties, DSC). Between 100 and 140 °C the hydrogen bonded amide N-H vibration band shifts from 3292 to 3333 cm^{-1} and broadens, indicating that the strength of the hydrogen bonds decreases (**Figure 3.4**a). In addition, a new band at 3400 cm^{-1} characteristic of free N-H bonds arises. Melting of the hard segments is also reflected by the strong decrease of the H-bonded ordered amide C=O stretching vibration band at 1652 cm^{-1} and the appearance of the non H-bonded amide C=O peak at 1686 cm^{-1} (**Figure 3.4**b). Such observation seems to agree with the disruption of a crystalline type of order. The ester C=O stretching vibration at 1749 cm^{-1} only slightly broadens and decreases in intensity as expected for non-ordered and non hydrogen-bonded ester groups. Similar structural characteristics were observed in the FTIR spectra of the segmented PEEAs **5, 6** and **8**.

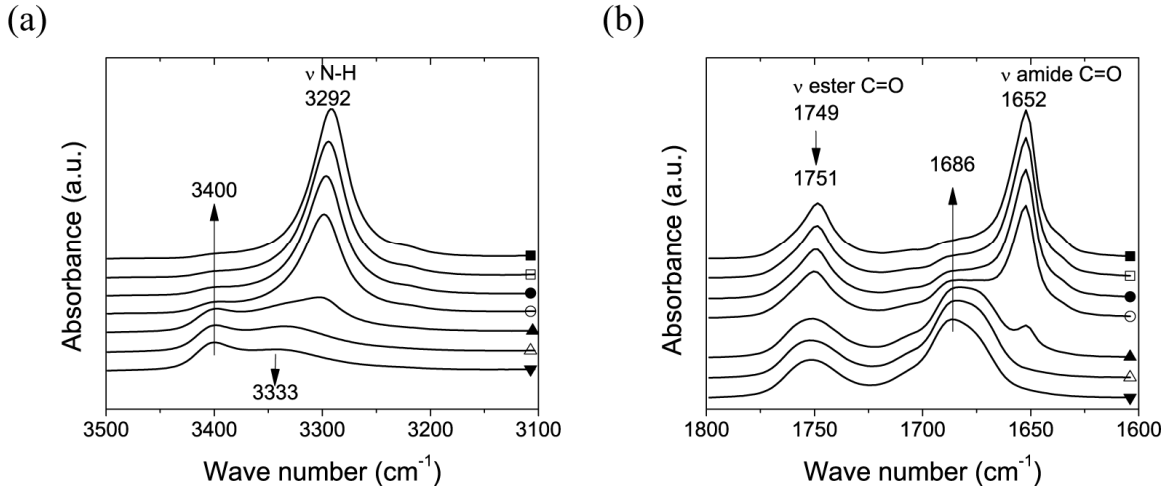

Figure 3.4. FTIR spectra of $PTHF_{1000}$-Gly-$OXA_2$6-Gly **(7a)** at 35 ■, 70 □, 100 ●, 120 ○, 140 ▲, 170 Δ and 200 °C ▼ for (a) the N-H stretching vibration band and (b) the ester and amide C=O stretching vibration band.

The degree of hard segment organization can be estimated by deconvolution of the amide C=O stretching band and calculation of the ratio of the area associated with the hydrogen bonded ordered amide phase at 1652 cm^{-1} to the total amide absorption area. For the polymers comprising Gly-$OXA_2$6-Gly hard segments **7a-c**, the molar fraction of ordered hard segments ranged from 73 to 85 %, while this value was between 95 and 100 % for polymers $PTHF_{1000}$-Gly-$OXA_2$2-Gly **(5)**, $PTHF_{1000}$-Gly-$OXA_2$4-Gly **(6)** and $PTHF_{1000}$-βala-$OXA_2$6-βAla **(8)**. The hard segment ordering of these polymers as a function of the temperature is depicted in **Figure 3.5**. By increasing the M_n of the polytetrahydrofuran soft segment and thus decreasing the hard segment content, the process of relative reduction in ordered H-bonded amide species shifts to slightly lower temperatures (**Figure 3.5**a). This can be explained by the solvent effect proposed by Flory.[38] Upon dilution of the ordered hard segments by increasing the molar fraction of the soft segment, the size of the ordered domains will become smaller. The observed melting transitions appeared to be more affected by changing the number of methylene groups between the oxalamide moieties. Increasing the number of methylene groups in the spacer connecting the two oxalamide moieties shifted the transition to lower temperatures. Replacing the glycine end-functional group by β-alanine however shifted the transition to a higher temperature. This may be explained by a better packing of the β-alanine end groups in the structure.

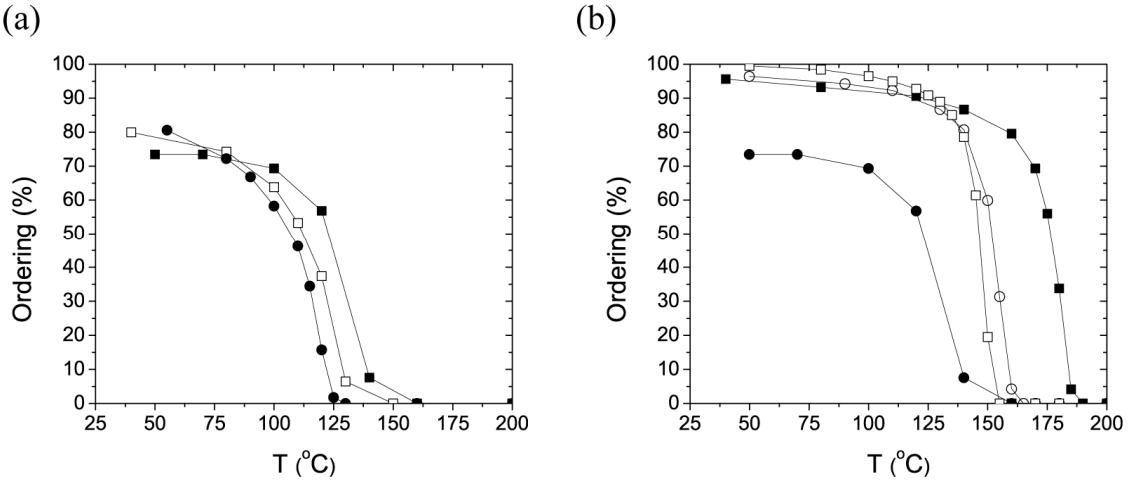

Figure 3.5. Hard segment ordering as a function of the temperature for (a) (■) $PTHF_{1000}$-Gly-$OXA_2$6-Gly **(7a)**, (□) $PTHF_{2000}$-Gly-$OXA_2$6-Gly **(7b)** and (●) $PTHF_{2900}$-Gly-$OXA_2$6-Gly **(7c)**. (b) (■) $PTHF_{1000}$-Gly-$OXA_2$2-Gly **(5)**, (□) $PTHF_{1000}$-Gly-$OXA_2$4-Gly **(6)**, (●) $PTHF_{1000}$-Gly-$OXA_2$6-Gly **(5a)** and (○) $PTHF_{1000}$-βAla-$OXA_2$6-βAla **(8)**.

3.3.3. Thermal properties

The crystallization and melting temperatures and corresponding enthalpies of the segmented poly(ether ester amide)s were taken from the first cooling scan and the second heating scan as measured by DSC (**Table 3.2**).

The segmented PEEAs exhibit a glass transition temperature between -68 and -76 °C. The DSC curves displayed in **Figure 3.6** show the effect of the soft segment M_n on the thermal properties. $PTHF_{1000}$-Gly-$OXA_2$6-Gly **(7a)** has a melting transition at 119 °C and a crystallization transition at 99 °C. Increasing the polytetrahydrofuran segment M_n from 2.0×10^3 to 2.9×10^3 g·mol^{-1} results in an additional thermal transition, which is attributed to crystallization of the soft polytetrahydrofuran phase. The melting temperature increases from -9 to -5 °C and the crystallization temperature increases from –43 to –32 °C with increasing PTHF M_n. Contrary, the melting temperature of the bisoxalamide phase decreases from 119 to 111 °C as the polytetrahydrofuran M_n increases and thus the hard segment content decreases.

The effect of the number of methylene units separating the bisoxalamide moieties in the hard segment on the polymer thermal properties is depicted in **Figure 3.7**. The segmented poly(ether ester amide)s comprising glycine based bisoxalamide hard segments **5**, **6** or **7a** show one melting and crystallization transition attributed to the bisoxalamide hard segment crystals. By increasing the number of methylene groups from 2 to 6, the melting temperature decreases from 171 to 119 °C. This trend is generally observed for nylon type materials, which show a decrease in melting temperature when the amide-to-methylene ratio decrease

i.e. when the concentration of hydrogen bonds in the polymer chain decreases. The melting temperature of the polymer made with the β-alanine capped hard segment **(8)** is found at 142 °C, which is much higher than that of its glycine analogue **7a** (119 °C). A similar phenomena is observed for the bisester-bisoxalamide monomers Gly-OXA$_2$6-Gly **(2c)** (181 °C) and βAla-OXA$_2$6-βAla **(3)** (196 °C).[35]

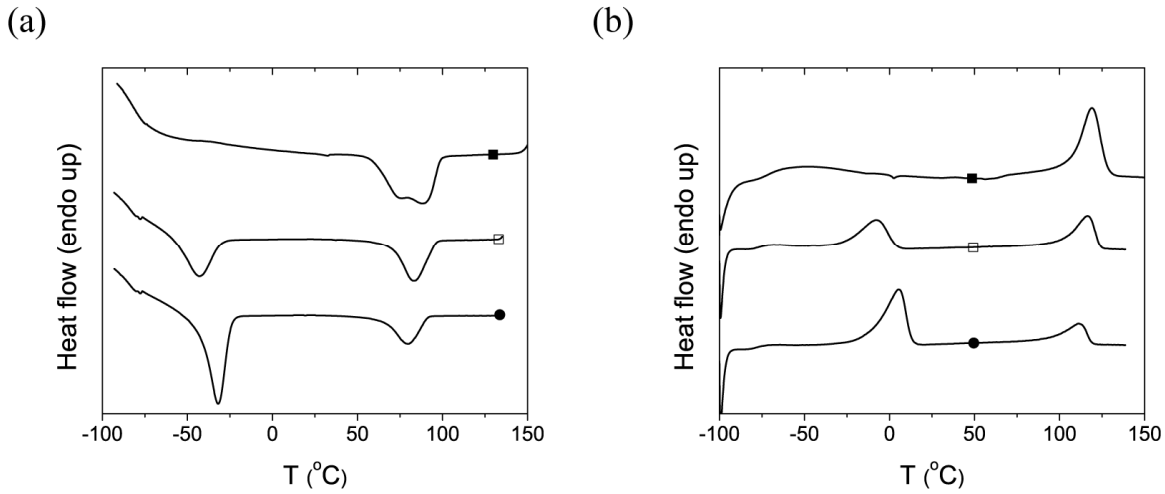

Figure 3.6. DSC first cooling curves (a) and second heating curves (b) of segmented poly(ether ester amide)s (■) PTHF$_{1000}$-Gly-OXA$_2$6-Gly **(7a)**, (□) PTHF$_{2000}$-Gly-OXA$_2$6-Gly **(7b)** and (●) PTHF$_{2900}$-Gly-OXA$_2$6-Gly **(7c)**.

The degree of hard segment crystallinity in the polymer was calculated by using the melting enthalpies determined for the monomers. For all polymers, the crystallinity of the amide phase is higher than 85 % (**Table 3.2**). The supercooling effect, the difference between the melting temperature and the crystallization onset, is for all polymers lower than 20 °C consistent with fast crystallization of the hard segments, which is favorable for processing.

Thermal stability of the segmented poly(ether ester amide)s **5-8** under non-oxidative conditions was investigated by thermal gravimetric analysis (TGA). The segmented poly(ether ester amide)s are stable up to ~390 °C (**Table 3.2**). For all polymers, the decomposition temperatures are considerably higher than the melting temperature, which is important for processing of the materials.

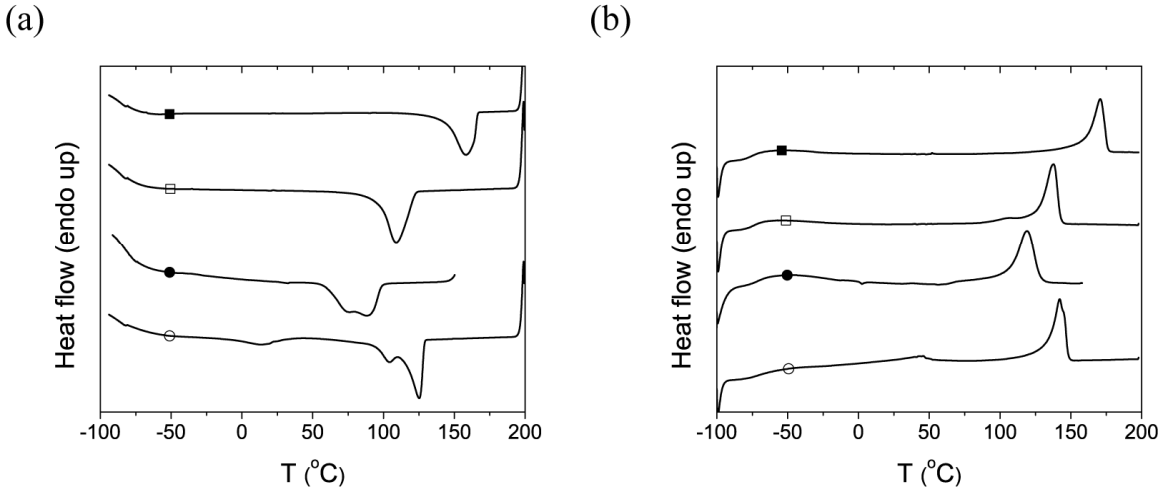

Figure 3.7. DSC first cooling curves (a) and second heating curves (b) of segmented poly(ether ester amide)s (■) $PTHF_{1000}$-Gly-$OXA_2$2-Gly **(5)**, (□) $PTHF_{1000}$-Gly-$OXA_2$4-Gly **(6)**, (●) $PTHF_{1000}$-Gly-$OXA_2$6-Gly **(7a)** and (○) $PTHF_{1000}$-βAla-$OXA_2$6-βAla **(8)**.

Table 3.2. Thermal properties of segmented poly(ether ester amide)s **5**-**8**.

			Hard Segment							
	T_d (°C)	T_g (°C)	T_m (°C)	ΔH_m ($J.g^{-1}$)	T_c (°C)	ΔH_c ($J.g^{-1}$)	ΔH_m* ($J.g^{-1}$)	T_{onset} (°C)	Super (°C)	X_c** (%)
7a	420	-68	119	25	88	23	111	99	20	85
7b	426	-76	116	16	83	16	111	96	20	95
7c	426	-75	111	12	80	11	111	91	20	99
5	393	-74	171	28	159	26	124	166	5	100
6	406	-73	138	29	109	29	119	122	16	100
8	421	-70	46/142	5/28	13/125	5/32	113	129	13	88

*Melting enthalpy of the corresponding monomers[35]
**Degree of crystallinity determined by DSC

3.3.4. Morphology

In our previous study[34], we suggested that bisoxalamide hard segments in segmented poly(ether amide)s form fiber-like nano-crystals as schematically depicted in **Figure 3.11**a. It was shown that the long direction of the crystals is the direction of the hydrogen bonds (***a***-direction). In the present work, we explore the structure of segmented poly(ether ester amide)s based on glycine or β-alanine extended bisoxalamide hard segments **(5-8)**. As mentioned previously, the copolymers are phase separated into relatively pure amide and polyether domains. FTIR measurements accordingly revealed that the bisoxalamide-based hard segments are highly ordered and that hydrogen bonds are solely formed between the oxalamide groups. This leads to a picture of bisoxalamide crystalline structures formed by a

process of self-assembly of oxalamide groups into hydrogen bonded sheets with subsequent stacking of the hydrogen bonded sheets. The crystalline structure of the hard segments likely resembles the crystalline structure of the corresponding monomers **2a-c** and **3**, and was addressed by X-ray diffraction. To this end, powder-like compounds were heated above the melting temperature and subsequently extruded through a die of 300 μm in diameter followed by fast cooling down to room temperature to prevent reorientation of crystals.

All five compounds exhibit a series of strong equatorial peaks with the period close to the long molecular dimension (***c***-parameter). The 2D WAXS fiber patterns corresponding to monomers **2c** and **3** are shown in **Figure 3.8**. Their ***c***-parameter equals 27.27 and 25.81 Å, whereas the length of the monomers in the assumption of the extended chain conformation is 28.75 and 31.25 Å, respectively. Although the unit cells of the monomers were not determined at this stage, from the analogy with the bisoxalamide we studied previously one can expect that one of the parameters other than **c** (e.g., ***a***-parameter) corresponds to the molecular width within the hydrogen bonded planes and the other one- to the distance between these planes (e.g., ***b***-parameter).[34] The value of the ***a***-parameter along the hydrogen bond direction was estimated from the position of the layer lines at the fiber pattern. A strong meridional peak located on the second layer line at around 2.5 Å gives the value for the ***a***-parameter of ca. 5 Å for all monomers, which is in agreement with the literature data on oxalamides.[39]

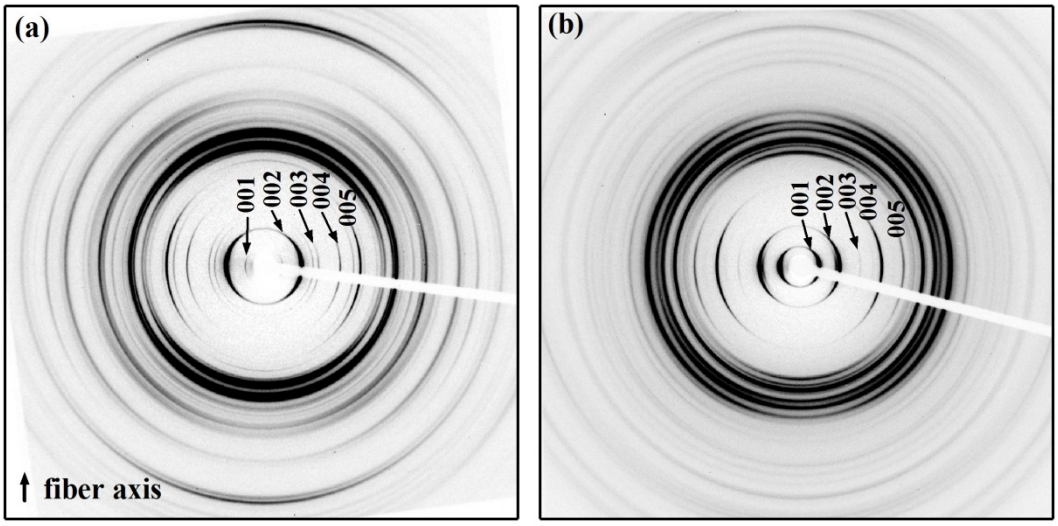

Figure 3.8. Selected 2D WAXS patterns of oriented monomers (a) Gly-$OXA_2$6-Gly **(2c)** and (b) βAla-$OXA_2$6-βAla **(3)**.

To obtain more insight in the crystalline structure of the hard segments in the PEEAs, the materials were further investigated using AFM and X-ray diffraction techniques.

Atomic force microscopy

To illustrate the highly phase separated structure of the segmented poly(ether ester amide)s, the morphology was visualized with atomic force microscopy (AFM) (**Figure 3.9**) The results reveal a morphology characterized by long ribbon-like nano-crystals in a soft polymer matrix. A similar morphology was shown in previous research for analogous bisoxalamide based segmented poly(ether amide)s.[34]

The AFM measurements confirm the proposed fiber-like model as depicted in **Figure 3.11**a. Because the AFM tip has a radius of 8 nm, an accurate determination of the fiber diameter (≤ 3 nm) was not possible. The length of the crystals is up to several hundreds of nanometers. However, the full length of the crystals cannot be determined since only the surface morphology of the sample is scanned.

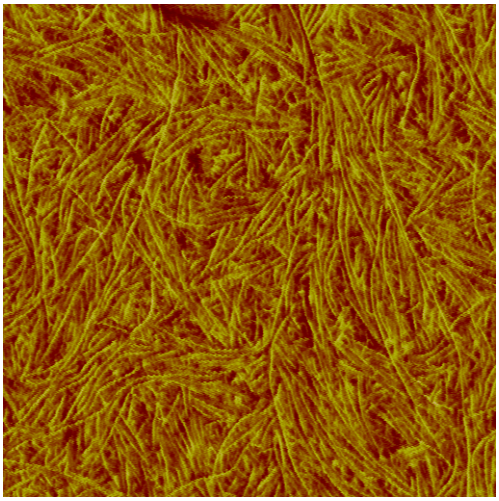

Figure 3.9. Phase image of $PTHF_{1000}$-βAla-$OXA_2$6-βAla **(7)** (image size: 1 × 1 μm).

WAXS

The diffraction peaks observed for the bisoxalamide monomers are largely absent from the curves of the corresponding copolymers and a broad amorphous halo originating from the PTHF phase is mainly visible for samples **5-7** (**Figure 3.10**). The fact that the diffraction peaks are scarce in the patterns of the copolymers can be explained by the small crystal thickness along the ***c***-direction. Moreover, since only one peak corresponding to ~2.5 Å shows up in the WAXS curves for all polymers, it can be suggested that the small dimensions

of the fibers are in the ***bc***-plane while the ***a***-parameter is parallel to the long fibrillar axis. However, the diffraction in the ***b***-direction, i.e. the direction of stacking of the hydrogen bonded sheets, is weak in the diffractogram of the corresponding monomers and consequently not visible in the X-ray pattern of the polymer.

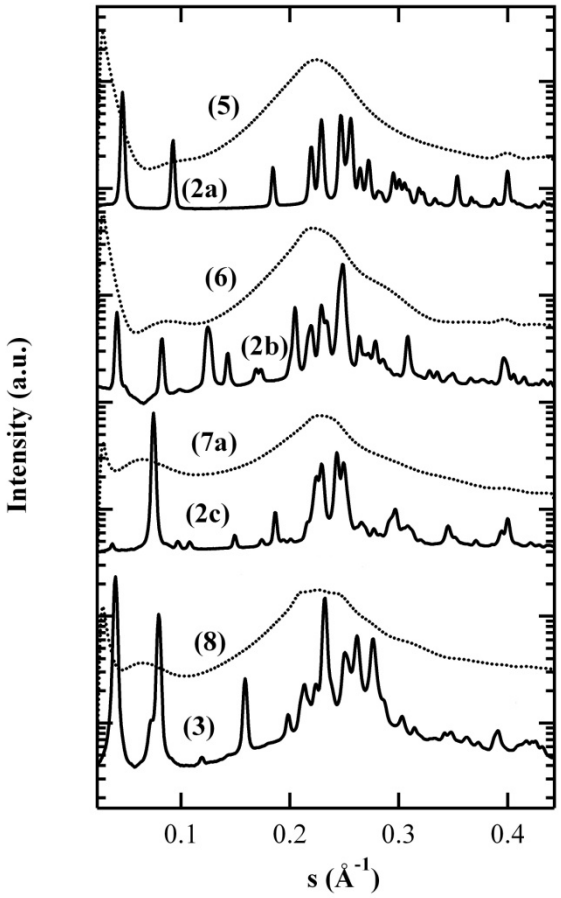

Figure 3.10. WAXD curves of bisester-bisoxalamide monomers and corresponding copolymers of Gly-$OXA_2$2-Gly **(2a)** and $PTHF_{1000}$-Gly-$OXA_2$2-Gly **(5)**, Gly-$OXA_2$4-Gly **(2b)** and $PTHF_{1000}$-Gly-$OXA_2$4-Gly **(6)**, Gly-$OXA_2$6-Gly **(2c)** and (d) $PTHF_{1000}$-Gly-$OXA_2$6-Gly **(7a),** βAla-$OXA_2$6-βAla **(3)** and $PTHF_{1000}$-βAla-$OXA_2$6-βAla **(8)**.

SAXS

The SAXS curves of all segmented PEEAs **5-8** show an interference maximum indicative of the presence of phase separated domains. Based on the fibrillar morphology observed with AFM, the interpretation of the SAXS curves was done using a 2D structural model (**Figure 3.11**a) (and not the conventional 1D model describing the lamellar structures).[34]

Thus, it is assumed that the crystalline domains are much longer in one direction than in the two others and can therefore be considered as virtually infinite fibrils. The micro-

structural parameters of the samples (see **Figure 3.11**a) such as the long spacing (L_B), crystal thickness (L_c) and amorphous domain thickness (L_a) can be derived from the SAXS curves in the approximation of a hexagonal packing of the fibrillar crystals. The L_B corresponds to the position of the Bragg peak whereas the crystalline domain thickness (L_c) was calculated from the position of the form factor visible in the medium-angle range (**Figure 3.11**b). The scattering intensity in the neighborhood of the form factor minimum was approximated with the following expression:

$$I(s) \propto \frac{1}{s^2}\left(\frac{\sin(\pi \times s \times L_c)}{\pi \times s \times L_c}\right)^2 \tag{3.1}$$

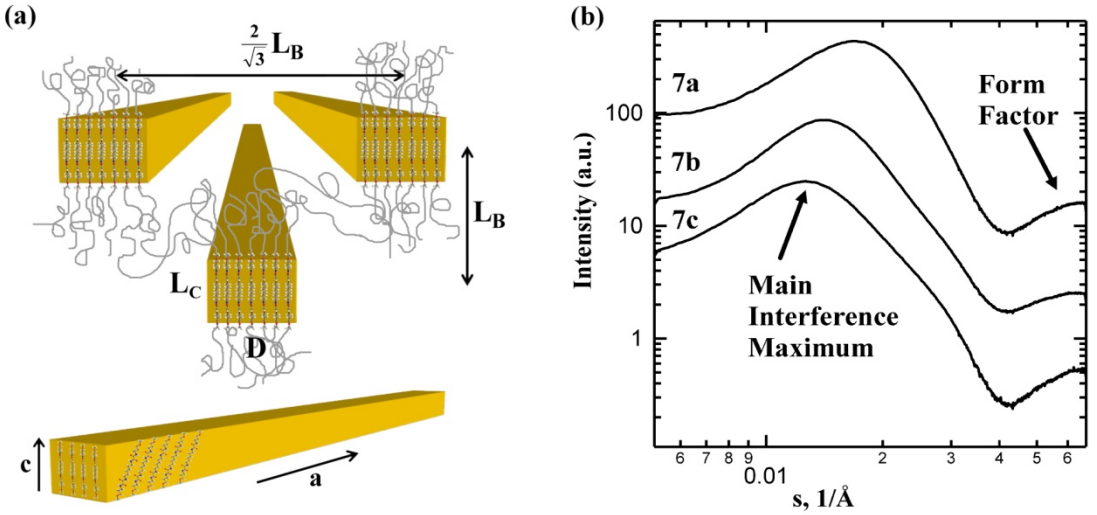

Figure 3.11. (a) Fibrillar crystal model used for interpretation of the SAXS data.[34] (b) SAXS intensities corresponding to the segmented poly(ether ester amide)s consisting of Gly-OXA$_2$6-Gly hard segments and PTHF soft segments with varying lengths **(7a-c)**.

It is noteworthy that the fact that the crystals' form factor is observed in SAXS curves signifies that the crystal thickness is rather monodisperse. For example, observation of the crystals' form factor constitutes a rare observation for semicrystalline polymers because variation of the crystallization temperature during the structure formation and structural defects of different nature easily suppress this feature from the SAXS curves.[40-42] In our case, the monodispersity of the crystals is determined by the chemistry of the copolymers and therefore should be independent from the crystallization conditions.

The crystal width D was calculated from the crystalline volume fraction Φ_{vol} of the bisoxalamide vs. PTHF, L_B and L_c values as follows:

$$\Phi_{vol} = \frac{S_{crystalline\_core}}{S_{lattice\_surface}} \tag{3.2}$$

$$\frac{\frac{M_{bisoxalamide}}{\rho_{bisoxalamide}}}{\frac{M_{bisoxalamide}}{\rho_{bisoxalamide}} + \frac{M_{PTHF}}{\rho_{PTHF}}} = \frac{Lc \times D}{\frac{2}{\sqrt{3}} \times L_B{}^2} \tag{3.3}$$

$$D = \frac{\Phi_{vol} \times \frac{2}{\sqrt{3}} \times L_B{}^2}{Lc} \tag{3.4}$$

Here ρ is the density (0.982 and 1.21 g·cm^{-3} for amorphous PTHF and bisoxalamide segments, respectively), $S_{crystal\_core}$ is the surface per crystal core and $S_{lattice\_surface}$ is the total surface of the 2D lattice formed by the fibrils assuming hexagonal packing of the crystals.

Table 3.3. Long spacing (L_B), crystalline lamellar thickness (L_c and D) and amorphous lamellar thickness (L_a) of segmented poly(ether ester amide)s **5-8**.

	L_B (Å)	L_c (Å)	D (Å)	L_a (Å)	Chain tilt (deg)	Stem Length* (Å)	Hard block Length** (Å)
7a	57.5	24	32	33.5	~5-10	24	18.75
7b	71.4	24	27	47.4	~5-10	24	18.75
7c	79	24	24	55	~5-10	24	18.75
5	49.8	14.3	29	35.5	~5-10	14.5	13.75
6	52.6	17.4	32	35.2	~5-10	17.6	16.25
8	73	22.9	50	50.1	~28	25	18.75

*The value obtained by dividing L_c by the cosine of the tilt angle

**The hard block length is defined as a part of the molecule delimited by the hydrogen bonds.

The resulting long spacing (L_B), crystal dimensions (L_c and D) and amorphous layer thickness (L_a) are listed in **Table 3.3**. It can be seen that the L_B and the L_a increase with the increase of M_n of the PTHF segment length from 1.0×10^3 to 2.9×10^3 g·mol^{-1} **(7a-c)**, whereas the crystal thickness L_c remains constant. This is logical because the weight fraction of the fibrillar crystals formed by the hard block is directly affected by the PTHF segment length. Another interesting observation is that L_a can significantly differ for the hard blocks with

different end groups (cf. for example samples **7a** and **8**). This is linked to the variation of the crystal width, i.e. when the crystals become wider, the nearest neighbor distance increases accordingly. As far as the crystal thickness is concerned the value of L_c increases with the spacer length between oxalamide groups. Therefore, the crystal morphology is mainly determined by the structure of the hard segment. For all copolymers, the L_c is found to be somewhat larger than the estimated hard block length, which indicates that the crystalline core in the copolymer structure also partially includes the ester groups.

When the length of the crystalline stem is calculated by dividing L_c by the cosine of the tilt angle, one can see that copolymers **7a** (glycine substituted bisoxalamide) and **8** (β-alanine substituted bisoxalamide) exhibit similar values of the stem length (~25 Å) while their melting temperatures, 119 °C and 142 °C, respectively, strongly differ. Therefore, the L_c is not the only parameter determining the melting temperature, but the arrangement of the hard block inside the unit cell (i.e. the chain tilt and possibly the difference in the H-bonding energy are also important).

Temperature-dependent WAXS/SAXS

Temperature-dependent WAXS and SAXS measurements were performed to obtain information on the evolution of the phase-separated morphology upon heating. **Figure 3.12** shows the results of such measurements for the segmented poly(ether ester amide)s with different soft segment lengths **(7a-c)**.

Below 0 °C, the (020) and (110) peaks of PTHF crystals are clearly seen for the copolymers with PTHF segment lengths of 2.0×10^3 and 2.9×10^3 $g\cdot mol^{-1}$ (**7b** and **c**). Moreover, the PTHF peaks are much stronger for copolymer **7c**, indicating that the crystallinity of the soft block rapidly increases with its length. The melting transitions of PTHF crystals visible from the variation of the (020) and (110) peaks intensity are in agreement with DSC measurements. The main SAXS interference maximum and the form factor of the bisoxalamide crystals located at ~0.07 $Å^{-1}$ disappear at the melting temperature of the copolymer hard blocks indicating a transition to the homogeneous melt.

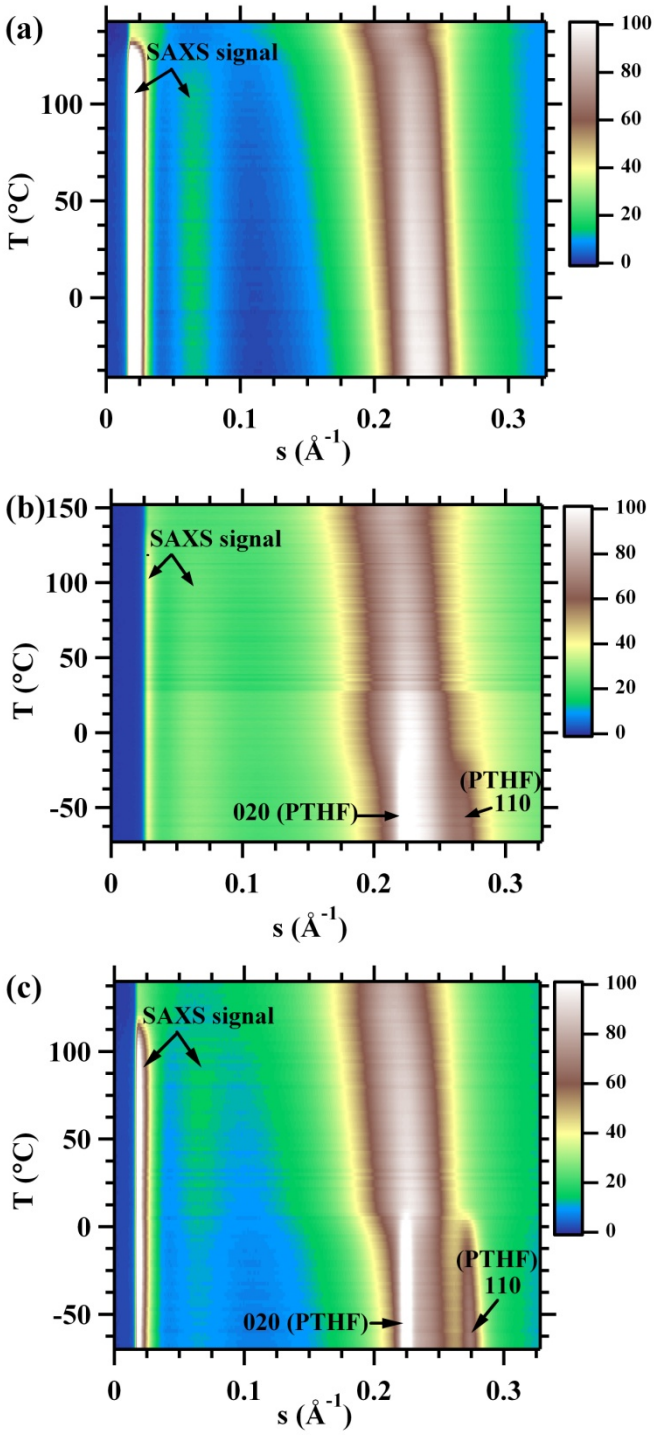

Figure 3.12. Results of simultaneous SAXS/WAXS measurements performed during heating for segmented poly(ether ester amide)s with polytetrahydrofuran with molecular weights of (a) 1.0×10^3 g.mol^{-1} **(7a)**, (b) 2.0×10^3 g.mol^{-1} **(7b)** and (c) 2.9×10^3 g·mol^{-1} **(7c)**.

3.4. Conclusions

Novel 100% aliphatic thermoplastic elastomers are introduced based on oxalic acid chemistry and industrial and potentially renewable monomers like glycine (ethyl ester), aliphatic diamines and high molecular weight diols. In particular, segmented poly(ether ester amide)s were prepared by melt polycondensation of α,ω-hydroxyl end functionalized polytetrahydrofuran and -OH reactive bisester-bisoxalamides with spacer lengths of 2, 4 or 6 methylene groups and capped with glycine- or β-alanine ethyl ester functional groups. All segmented copolymers appear to be highly phase separated materials. FTIR revealed strongly hydrogen bonded and highly ordered bisoxalamide segments with hydrogen bonds formed between the oxalamide groups. The hard segment crystallinities were in between 73 and 99 %. A fibrillar morphology consisting of ribbon-like nano-crystals randomly dispersed in the polyether matrix was observed using AFM. Further structural information was extracted from simultaneous small- and wide-angle X-ray scattering. The long dimension of the crystals is parallel to the direction of the hydrogen bonds, whereas the two small dimensions correspond to the length of one bisoxalamide segment and to the width of the stacks of hydrogen bonded sheets containing ca. 6 to 12 hydrogen bonded sheets, respectively. The melting transition of the glycine based hard segment increased from 119 to 170 °C with decreasing spacer length from 6 to 2 methylene groups. Moreover, changing the glycine ester group into a β-alanine, Gly-$OXA_2$6-Gly to βAla-$OXA_2$6-βAla, led to an increase of the melting transition of the hard segments from 119 to 141 °C. The differences in thermal properties between the copolymers comprising β-alanine or glycine based hard segments is related to a difference in the crystal structure of the hard segment.

3.5. References

(1) Fakirov S. Handbook of condensation thermoplastic elastomers. Weinheim: Wiley-VCH; **2005**.

(2) Holden G, Legge NR, Quirk RP, Schroeder HE. Thermoplastic elastomers, 2nd ed. Munich: Hanser Publishers; **1996**.

(3) Cella RJ. *J Polym Sci: Symp No 47* **1973**;42:727-40.

(4) Biemond GJE, Feijen J, Gaymans RJ. *Polym Eng Sci* **2008**;48:1389-400.

(5) Das S, Cox DF, Wilkes GL, Klinedinst DB, Yilgor I, Yilgor E, Beyer FL. *J Macromol Sci Phys* **2007**;46:853-75.

(6) Das S, Yilgor I, Yilgor E, Inci B, Tezgel O, Beyer FL, Wilkes GL. *Polymer* **2007**;48:290-301.

(7) Eisenbach CD, Stadler E. *Macromol Chem Phys* **1995**;196:1981-97.

(8) Fu B, Macknight WJ, Schneider NS. *Rubber Chem Technol* **1986**;59:896-911.

(9) Harrell LL. *Macromolecules* **1969**;2:607-12.

(10) Miller JA, Lin SB, Hwang KKS, Wu KS, Gibson PE, Cooper SL. *Macromolecules* **1985**;18:32-44.

(11) Ng, H. N.; Allegrezza, A. E.; Seymour, R. W.; Cooper, S. L. *Polymer* **1973**, *14*, 255–261.

(12) Niesten MCEJ, Feijen J, Gaymans RJ. *Polymer* **2000**;41(24):8487-500.

(13) Shirasaka H, Inoue S, Asai K, Okamoto H. *Macromolecules* **2000**;33:2776-78.

(14) Versteegen RM, Kleppinger R, Sijbesma RP, Meijer EW. *Macromolecules* **2006**;39:772-83.

(15) Versteegen RM, Sijbesma RP, Meijer EW. *Macromolecules* **2005**;38:3176-84.

(16) Yilgor I, Shaaban AK, Steckle WP, Tyagi D, Wilkes GL, McGrath JE. *Polymer* **1984**;25:1800-1806.

(17) Yilgor I, Yilgor E. *Polym Rev* **2007**;47:487-510.

(18) Tyagi D, Yilgor I, McGrath JE, Wilkes GL. *Polymer* **1984**;25:1807-1816.

(19) Arun A, Gaymans RJ. *Macromol Chem Phys* **2008**;209:854-63.

(20) Biemond GJE, Feijen J, Gaymans RJ. *J Appl Polym Sci* **2007**;105:951-63.

(21) Bouma K, Wester GA, Gaymans RJ. *J Appl Polym Sci* **2001**;80:1173-80.

(22) Gaymans RJ, Dehaan JL. *Polymer* **1993**;34:4360-64.

(23) Husken D, Feijen J, Gaymans RJ. *J Polym Sci Part A Polym Chem* **2007**;45:4522-35.

(24) Krijgsman J, Husken D, Gaymans RJ. *Polymer* **2003**;44:7573-88.

(25) Krijgsman J, Husken D, Gaymans RJ. *Polymer* **2003**;44:7043-53.

(26) Niesten MCEJ, Bouma K, Gaymans RJ. *Polymer* **1998**;39:93-98.

(27) Niesten MCEJ, Gaymans RJ. *Polymer* **2001**;42:6199-207.

(28) Niesten MCEJ, Harkema S, van der Heide E, Gaymans RJ. *Polymer* **2001**;42:1131-42.

(29) Niesten MCEJ, Tol R, Gaymans RJ. *Polymer* **2001**;42:931-39.

(30) van der Schuur M, de Boer J, Gaymans RJ. *Polymer* **2005**;46:9243-56.

(31) van der Schuur M, Feijen J, Gaymans RJ. *Polymer* **2005**;46:4584-95.

(32) van der Schuur M, Feijen J, Gaymans RJ. *Polymer* **2005**;46:327-33.

(33) Van der Schuur M, Gaymans RJ. *J Polym Sci Part A Polym Chem* **2006**;44:4769-81.

(34) Sijbrandi NJ, Kimenai, AJ, Mes EPC, Broos R, Bar G, Rosenthal M, Odarchenko YaI, Ivanov, DA, Dijkstra PJ, Feijen J. *Macromolecules* **2012**;45:3948-61.

(35) Sijbrandi, N. J.; Kimenai, A. J.; Mes, E. P. C. C.; Broos, R.; Bar, G.; Rosenthal, M.; Odarchenko, Y. I.; Ivanov, D. A.; Feijen, J.; Dijkstra, P. J. *Polymer* **2012**, *53*, 4033–4044.

(36) Meier RJ. *Vib Spectrosc* **2005**;39:266-69.

(37) Asin L, Armelin E, Montane J, Rodriguez-Galan A, Puiggali J. *J Polym Sci Part A Polym Chem* **2001**;39:4283-93.

(38) Flory PJ. *Trans Faraday Soc* **1955**;51:848-57.

(39) Coe S, Kane JJ, Nguyen TL, Toledo LM, Wininger E, Fowler FW, Lauher JW. *J Am Chem Soc* **1997**;119(1):86-93.

(40) Ivanov DA, Hocquet S, Dosiere M, Koch MHJ. *Eur Phys J E* **2004**;13:363-78.

(41) Ivanov DA, Bar G, Dosiere M, Koch MHJ. *Macromolecules* **2008**;41:9224-33.

(42) De ten Hove CLF, Penelle J, Ivanov DA, Jonas AM. *Nat Mater* **2004**;3:33-37.

CHAPTER 4. CONTROLLING CRYSTAL THICKNESS IN SEGMENTED ALL-ALIPHATIC COPOLYMERS BY THE PRIMARY CHEMICAL STRUCTURE

Yaroslav I. Odarchenko[a], Martin Rosenthal[a], Jaime J. Hernandez[a], Loic Vidal[a], Niels J. Sijbrandi[b], Ad J. Kimenai[c], Edwin P.C. Mes[c], René Broos[c], Georg Bar[d], Pieter J. Dijkstra[b], Jan Feijen[b] and Dimitri A. Ivanov[a]

[a]Institut de Sciences des Matériaux de Mulhouse-IS2M, CNRS LRC 7228, Jean Starcky, 15, F-68057 Mulhouse, France

[b]Department of Polymer Chemistry and Biomaterials, MIRA Institute for Biomedical Technology and Technical Medicine, Faculty of Science and Technology, University of Twente, P.O. Box 217, 7500 AE Enschede, The Netherlands

[c]Core R&D, DOW Benelux BV, P.O. Box 48, 4530 AA Terneuzen, The Netherlands

[d]Core R&D DOW Olefin Verbund GmbH, P.O. Box 1163, D-06258, Schkopau, Germany

The semicrystalline morphology of all-aliphatic thermoplastic elastomers consisting of alternating flexible PTHF segments and uniform glycine or β-alanine bisoxalamide units was studied. It is found that the thickness of the hard-block crystals is highly monodisperse and independent of the sample thermal history. The surface free energy of the hard-block crystals is extremely low (~18 erg/cm2), which is likely due to the entropic contribution of soft segments forming tie chains bridging the neighboring crystals. The crystal orientation and phase transitions were addressed during simultaneous time-resolved X-ray scattering and mechanical stretching experiments. Starting from the soft block length of 1000 g·mol^{-1} the elastomers crystallize upon stretching at ambient temperature. Two main morphologies were observed: at low strains the fibril-like crystals become oriented parallel to the flow direction due to their high-aspect ratio, whereas at higher strains the bisoxalamide crystals fragmentation sets in resulting in a change of the preferential stem direction to the one parallel to the drawing direction. The chain tilt in the bisoxalamide crystals was evaluated from the characteristic four-spot SAXS patterns. It was found to be ~5 to 16° for the case of glycine end group and 24° for the alanine and propyl terminal groups.

4.1. Introduction

Recent advances in the design of thermoplastic elastomers, TPEs, stimulated new research into their structure and morphology.[1,2,3] At the service temperatures these materials typically exhibit a phase-separated morphology which depends on the chemical structure, weight fractions and polydispersity of the soft and hard blocks, as well as on preparation conditions such as the sample thermal history. The segmented block copolymers with uniform hard units constitute a special type of TPEs showing fast and nearly complete crystallization. Their structure is composed of ribbon-like crystals immersed in a soft-segment matrix.[4,5] Till now, the information on the uniform thickness of the hard-block crystals was extracted either from DSC data (i.e. from indirect method) or from qualitative analysis of AFM images.[4,6,7]

In general, monodisperse crystals constitute a rather rare observation for semicrystalline polymers.[8,9,10] Indeed, variation of the crystallization temperature during the structure formation and structural defects of different nature typically bring about polydisperse crystal size. Taking into account that the physical properties of semicrystalline polymers are strongly correlated with crystallinity, which is in turn a function of the processing conditions, it is clear that the design of novel TPEs, the properties of which are independent from the processing conditions, is an important challenge.

Apart from the uniform crystal thickness, the structural development during mechanical deformation is also important for the performance parameters of the studied copolymers. In the past, by means of IR spectroscopy it was shown that the deformation reveals two main stages of the morphological reorganization.[4,7] At low draw ratios below the yield point the hard segment chains in the crystals are preferentially oriented perpendicular to the drawing direction. Above the yield point, crystal fragmentation occurs and the hard segments in the crystals reorient along the stretching axis. At large deformations the broken lamellae transform to highly stressed nanofibrils consisting of alternating hard and soft segments, as deduced from small-angle X-ray scattering (SAXS) data.[11,12] The four-spot SAXS patterns recorded at relatively early stages of elongation (ca. 50-150 %) were attributed to formation of tilted hard-segment morphology explained in terms of the high aspect ratio of hard-block crystals.[11,13] However for conventional polyolefins like polyethylene (PE) the former phenomena was interpreted by the tilted chain morphology in the folded lamellar crystals.[14,15] It has been a long way to prove the existence of chain tilt in bulk isotropic PE considering the extensive investigations of the polymer crystallization and structure formation upon

deformation. First, the tilt angle, Φ_c, was deduced from the difference in the long periods for the drawn PE by Peterlin *et al.*[14] Later the chain tilt in single crystal mats was obtained for example by means of X-ray and electron diffraction experiments by Hocquet and coworkers.[16,17] Recently, the accurate value of 35° for the chain tilt in the bulk was measured by our group using the microfocus X-ray scattering.[18] To our knowledge, the chain tilt in the crystals of the phase separated block copolymers has not yet been reported. One can imagine all drawbacks encountered on the way to understand the chains packing for nanometer scale fibril-like crystals anchored to the soft segments chains.[5] Despite the fact that the hard block is highly crystalline (the degree of crystallinity approaches 100%) its weight content in the TPE is typically low (not exceeding 25%) that limits classical structural methods used for the semicrystalline homopolymers.[14]

In this work, the polymer system for which the crystal structure defined by the primary chemical sequence is presented. To get insights into the deformation behavior of the studied poly(ether ester amide)s, the in-situ stretching combined with X-ray experiments were conducted. In particular, the crystal orientation and phase transition of both segments while drawing are addressed. The morphology of the oriented segmented copolymers was studied by temperature-dependent SAXS/WAXS measurements. The role of the monodisperse thickness of the hard-block fibrillar crystals as well as the low values of the surface energy calculated for these crystals will be discussed.

4.2. Experimental

4.2.1. Materials

Segmented poly(ether ester amide)s, PEEAs, comprising glycine or β-alanine extended bisoxalamide hard segments PTHF$_{1000}$-Gly-OXA$_2$2-Gly **(1)**, PTHF$_{1000}$-Gly-OXA$_2$4-Gly **(2)**, PTHF$_{1000}$-Gly-OXA$_2$6-Gly **(3a)**, PTHF$_{2000}$-Gly-OXA$_2$6-Gly **(3b)**, PTHF$_{2900}$-Gly-OXA$_2$6-Gly **(3c)**, PTHF$_{1000}$-βAla-OXA$_2$6-βAla **(4)** and PTHF$_{1100}$-OXA$_2$6 **(5)** were prepared as reported elsewhere.[5,19] In **Figure 4.1**, *n* denotes the number-averaged molecular weight of the PTHF soft segment, *p* is the number of ethylene groups between oxalamide units and *q* corresponds to the number of carbon atoms between oxalamide and ester groups. The yellow transparent elastic solid films were prepared by quenching in ice water or by non-isothermal melt crystallization using a cooling rate of 5º C·min^{-1}.

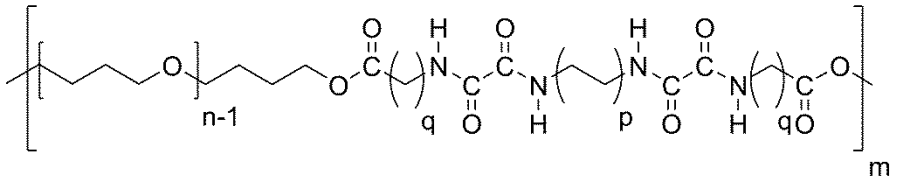

p = 1, q = 1 $PTHF_{1000}$-Gly-$OXA_2$2-Gly (1)
p = 2, q = 1 $PTHF_{1000}$-Gly-$OXA_2$4-Gly (2)
p = 3, q = 1 $PTHF_{1000}$-Gly-$OXA_2$6-Gly (3a)
p = 3, q = 1 $PTHF_{2000}$-Gly-$OXA_2$6-Gly (3b)
p = 3, q = 1 $PTHF_{2900}$-Gly-$OXA_2$6-Gly (3c)
p = 3, q = 2 $PTHF_{1000}$-βAla-$OXA_2$6-βAla (4)

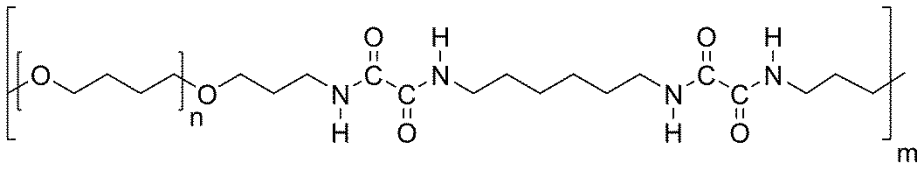

p = 3, q = 0 $PTHF_{1100}$-$OXA_2$6 (5)

Figure 4.1. Chemical structure of segmented block copolymers.

4.2.2. Methods

Polarized optical microscopy (POM) observations in transmission were carried out using an Olympus BX51 microscope equipped with a digital color camera Olympus DP70.

Wide- and Small-Angle X-ray Scattering (WAXS and SAXS) measurements were performed on the BM26 beamline of the European Synchrotron Radiation Facility (ESRF) (Grenoble, France) using the wavelength of 1.04 Å. The experimental setup comprised 2D detectors (FReLoN for WAXS and a Pilatus 1M for SAXS). The sample-to-detector distances were chosen to allow recording the signal in the s-range ($s=2\sin\theta/\lambda$, where θ is the Bragg angle) from 0.01 to 0.5 $Å^{-1}$. The modulus of the scattering vector **s** was calibrated using several diffraction orders of silver behenate. The diffraction patterns were collected in transmission geometry. The sample temperature was controlled by a Linkam heating stage with precision of 0.1 ºC.

The crystal thickness (L_c) was calculated by fitting the form-factor feature present in the SAXS curves using the following expression:

$$I(s) \propto A + \frac{B}{s^n}\left(\frac{\sin(\pi s L_c)}{(\pi s L_c)}\right)^2 \qquad (4.1)$$

The crystal size was estimated from 1D WAXS profiles using the Scherrer formula:

$$l_{hkl} = \frac{0.94\lambda}{\Delta \cos \vartheta} \tag{4.2}$$

The films used in the stretching experiments were cut from compression-molded bars (3x10x1 mm^3). The stress-strain tests were conducted with the Linkam TST 350 tensile stage equipped with the tensile sensor from 0.01 to 20 N. Three different deformation rates were used (20, 30 and 60 μm/s).

Selected-Area Electron Diffraction (SAED) experiments were carried out with a Philips CM200 transmission electron microscope operated at 200 keV. Calibration of the electron diffraction patterns was performed using graphite. The samples were prepared by precipitation from toluene on a glass slide. After the solvent evaporation, the films were floated off in 1% hydrofluoric acid aqueous solution. The samples were subsequently collected on gold TEM-grids with 400 meshes.

4.3. Results and Discussion

4.3.1. Structure of the monomers forming the hard block

Based on our previous X-ray diffraction and FTIR measurements, it was concluded that the crystalline structure of the hard segments in segmented poly(ether-amide)s most likely resembles the crystals of the corresponding monomers consisting of bisoxalamide moieties separated by an alkyl spacer of six methylene units and capped with 3-methoxypropyl end groups.[5] The bisester-bisoxalamide monomer Gly-$OXA_2$6-Gly having glycine terminal groups was examined with help of optical microscopy, X-ray and electron diffraction.

A typical polarized optical micrograph of a monomer shows strongly birefringent texture suggesting high crystallinity of the material (**Figure 4.2**A). The obtained single crystals for SAED experiments have a pronounced needle-like shape (cf. **Figure 4.2**B). The presence of preferential growth direction can be explained by the strong intermolecular like-to-like amide-amide hydrogen bonds, which, according to the FTIR measurements, are solely formed between the oxalamide groups.[18] The corresponding ED pattern is given in **Figure 4.2**C. The observed diffraction peaks belong to the [02-1] diffraction zone. The observed diffraction peaks can be indexed to a monoclinic unit cell with the following parameters: ***a*** = 5.09 Å, ***b*** = 10.88 Å, ***c*** = 27.73 Å and β = 79.6°. The measured and calculated *d*-spacings extracted from ED are summarized in **Table 4.1**. The peak indices obey the following extinction rules: (0kl) k=2n, (hkl) h+k=2n and (0k0) h,k=2n. This is compatible with the C2 symmetry group. The

inter-chain distance along the H-bonds direction derived from the diffraction patterns corresponds to the one known for Nylon 6,2.[20] The ***ac***-projection of the Gly-Oxa$_2$6-Gly monomer crystal is shown in **Figure 4.2**D. The unit cell contains 2 molecules. The adjacent molecules form the H-bonded sheets in the ***ac***-plane. Importantly, that the data derived from ED analysis can be used to index the X-ray fiber measurements (cf. **Table S4.1**).

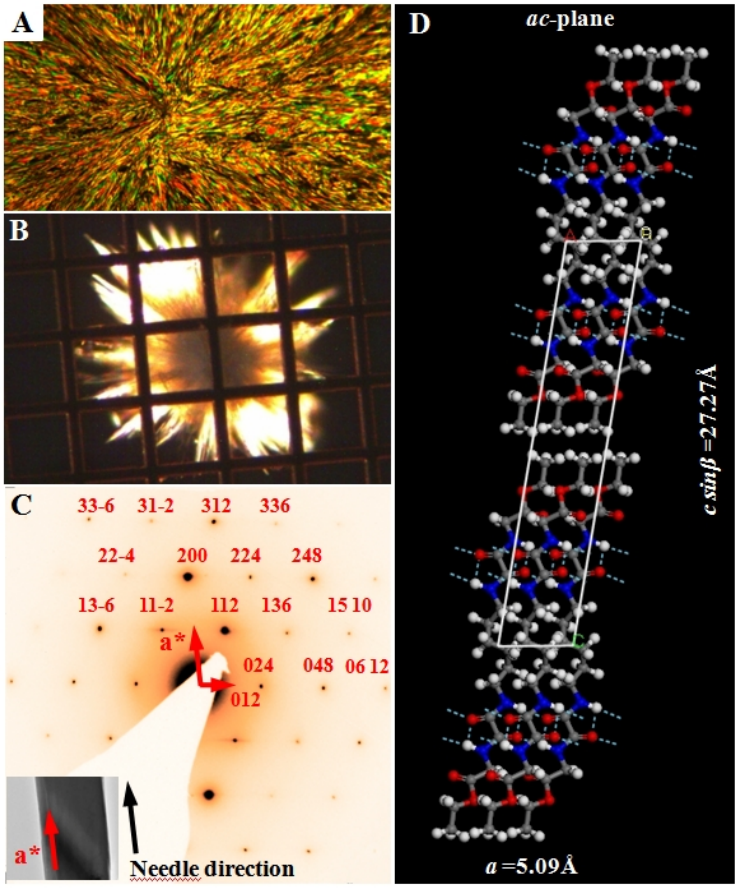

Figure 4.2. A: Polarized optical micrographs of the Gly-Oxa$_2$6-Gly monomer crystallized between glass cover slips. B: View of the needle-like crystals deposited on a TEM grid. C: Electron diffraction pattern corresponding to the [0-21] zone and corresponding TEM-image in correct orientation on the inset. D: Schematic model of the Gly-Oxa$_2$6-Gly crystal. The H-bonds are shown with dotted lines. Hydrogen atoms are hidden for the sake of clarity.

The indexation was performed assuming that the needle growth axis (H-bond direction) corresponds to the crystallographic ***a**** direction, as it can be seen from **Figure 4.2**C. This is in line with the reported structure of polyoxalamides. Indeed, the polyoxalamides with even number of carbon atoms in the spacer between the oxalamide groups adopt structures with only one hydrogen bonding direction, whereas the ones with odd spacers form two hydrogen bonding directions.[21,22,20] It should be mentioned, that previosuly based on Raman

spectroscopy and fiber X-ray diffraction, the H-bonding direction in the bisoxalamide based monomer was shown to be parallel to the ***a***-axis of the crystal (cf. **Figure 4.2**D).[5]

Table 4.1. Measured and Calculated d-Spacings (Å) extracted from Selected-Area Electron Diffraction Measurements on Needle-like crystals of the Gly-Oxa$_2$6-Gly monomer.

h	k	l	d_{exp}, Å	d_{calc}, Å	Lattice
0	2	4	4.25	4.25	
0	4	8	2.13	2.13	
0	6	12	1.43	1.42	
1	3	-6	2.35	2.36	Monoclinic; C2
1	1	-2	4.12	4.12	N13, c-unique
1	1	2	4.5	4.54	Conditions:
1	3	6	2.62	2.60	(0kl) k=2n
1	5	10	1.67	1.67	(hkl) h+k=2n
2	6	12	1.3	1.30	(0k0) h,k=2n
2	4	8	1.72	1.72	parameters:
2	2	4	2.27	2.27	a=5.09 Å
2	0	0	2.51	2.50	b=10.88 Å
2	2	-4	2.05	2.06	c=27.73 Å
3	3	-6	1.37	1.37	β=79.6°
3	1	-2	1.59	1.60	
3	1	2	1.67	1.67	
3	3	6	1.52	1.51	

4.3.2. Deformation behavior of poly(ether ester amide)s

To study the structure evolution of segmented PEEAs during tensile deformation, the in-situ X-ray diffraction experiments were carried out. The copolymer film samples were drawn at a constant deformation rate of 10 $\mu m \cdot s^{-1}$ while the 2D X-ray patterns were recorded simultaneously. In **Figure 4.3** some selected 2D-WAXS patterns for sample **3c** are shown. At zero deformation (cf. **Figure 4.3**A) the polymer reveals an isotropic pattern exhibiting a strong amorphous halo at about 4.4 Å. As mentioned in Chapter 3, the reflections from the hard segment crystals are largely absent from the diffractograms of copolymers. Only two reflections of the bisester-bisoxalamide crystals located at 2.48 and 2.30 Å (200 and 220 peaks, respectively) are visible on the pattern (see **Figure 4.3**A).

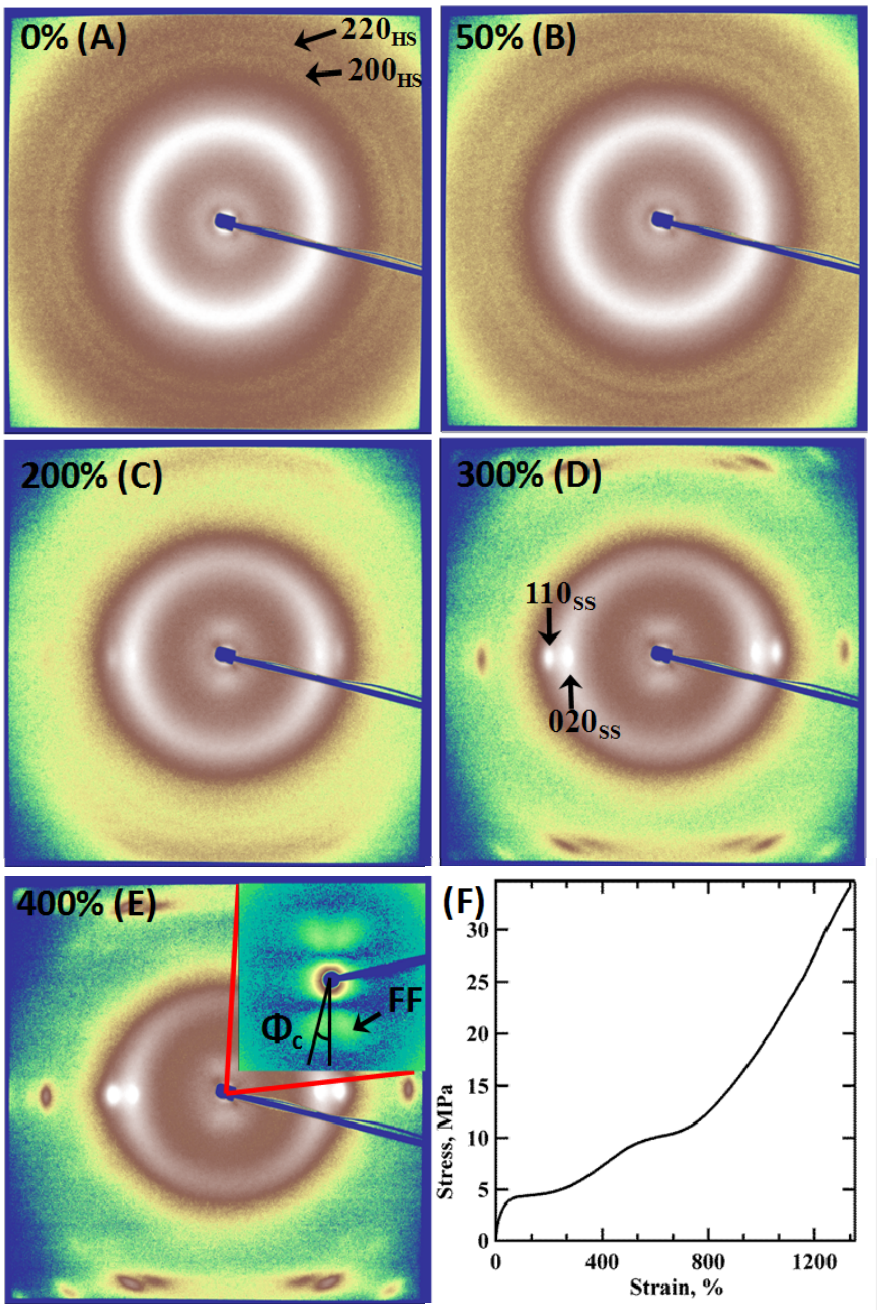

Figure 4.3. 2D-WAXS patterns measured during deformation of PEEA **3c** (A - E). Stress-strain curve for sample **3c** (F). The inset in the same panel shows a magnified four-spot SAXS pattern corresponding to the strain of 400%. The peaks pertinent to the hard and soft segment crystals are marked with subscripts "HS" and "SS", respectively. The stretching direction is vertical.

The characteristic feature in the small-angle region can be attributed to the form-factor (FF) generated by the bisoxalamide crystals due to their uniform thickness (cf. **Figure 4.3**). At the beginning, the non-stretched sample shows isotropic small-angle scattering (cf. **Figure 4.3**A), which is accounted for by random hard-segment crystals orientation (**Figure 4.4**A). At a strain of 50% a faint anisotropy can be noticed in the intensity distribution of the Gly-Oxa$_2$6-Gly crystalline peaks and in the PTHF amorphous halo (see **Figure 4.3**B). The fact

that the 200 reflection corresponding to the H-bonds direction exhibits pronounced arcing on the meridian shows that the hydrogen-bonded sheets are now parallel to the elongation direction. This situation is typical for orientation of high-aspect-ratio objects in a flow. A schematic model of the effect of stretching on the orientation of the fibril-like crystals immersed in the soft block matrix is depicted in **Figure 4.4**B.[19,23]

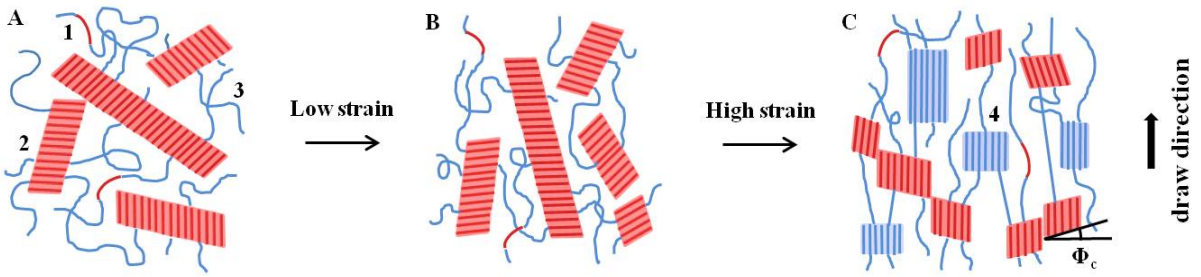

Figure 4.4. Schematic model of structural changes in PEEAs with uniform hard segments occurring during uniaxial deformation: A – nonoriented structure; B – the structure below the yield point; C – the structure above the yield point. The following morphological features are highlighted: 1 - hard block segment; 2 - hard block crystal; 3 - soft block segment; 4 - soft block crystal; 5 - chain tilt angle (Φ_c).

Similar effects of drawing on the orientation of high-aspect-ratio crystals at the initial stages of deformation (below yield point) were detected with the help of IR spectroscopy by Niesten[7] and Versteegen[4]. It should be mentioned that the yield point depends on the content and nature of the copolymer segments and is about 100% for sample **3c** (**Figure 4.3**F). Above the yield point at a strain of 200% sharp crystalline peaks corresponding to the PTHF crystals (reflections 020 and 110) appear on the equator (cf. **Figure 4.3**C). Simultaneously, a diffuse layer line with l=5 shows up in the diffraction pattern. These features are a signature of the strain-induced crystallization of the soft block.[7,11,13] Moreover, at the same stage the FF ripple stabilizes on the meridional direction (see **Figure 4.3**C) indicating that the hard segment stems become preferentially oriented parallel to the drawing direction. Upon increasing the strain to 400% the crystalline reflections of the soft PTHF block become stronger and better oriented (cf. **Figure 4.3**D-E). According to the literature, PTHF crystallizes in a monoclinic unit cell with the following lattice parameters: a = 5.61 Å, b = 8.92 Å, c = 12.25 Å and β = 134.3°.[24] The experimental and calculated d-spacings of the PTHF lattice are given in the Supporting Information (cf. **Table S4.2**). However, for the isotropic copolymer films no traces of PTHF crystals are observed at room temperature (**Figure 4.3**A) owing to the fact that the soft segments are not long enough to form stable crystalline nuclei.[4]

Generally, at high deformations (up to 450%) the 200 and 220 reflections of the hard block crystals are extremely weak as compared to the PTHF reflections, the fact that makes them almost unobservable in the diffractograms. However, on heating the oriented films above the melting temperature of the PTHF crystals the 200 and 220 crystalline reflections of the hard block become visible. Therefore, elevated-temperature measurements were used for precise determination of the bisoxalamide chain orientation, as exemplified in **Figure 4.5** for sample **3c**, which was first stretched to 200% and then heated to 80°C.[7] Here, the hard-segment 200 and 220 reflections are located on the equator indicating that the bisoxalamide crystal stems are preferentially oriented along the stretching direction. This result is supported by the presence of the strong FF signal positioned approximately on the meridian (**Figure 4.5**A). On **Figure 4.3**D the form-factor is not strictly meridional but is split into a clearly pronounced four-spot pattern suggesting a tilt of the hard segment crystalline stems with respect to the normal of the crystal basal plane (Φ_c). The formation of tilted morphology for the urethane-based elastomers at the initial stages of drawing has been previously reported by Bonart[13] and Hsiao[11]. The chain tilt behavior will be discussed later in some more detail.

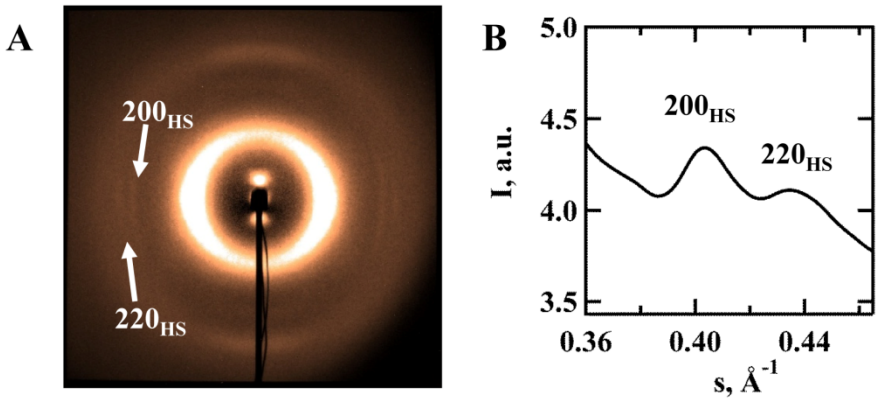

Figure 4.5. A: 2D-WAXS pattern of **3c** stretched to 200% deformation and heated to 80 °C. B: The corresponding equatorial section of the pattern in A showing two peaks corresponding to the hard-block crystals.

The resulting morphology of highly oriented PEEAs is depicted in **Figure 4.4**C. In this sketch, two types of non-folded crystals formed by the PTHF and bisoxalamide segments connected by taut PTHF chains are shown. For both crystal populations the stems are oriented along the drawing direction. This is in agreement with the literature[7,4] where one can find indications that, beyond the yield point, a different deformation mechanism sets in resulting in fragmentation of the hard-block crystals and leading to a drastic change in their orientation. The bisoxalamide crystals act as physical cross-links between the soft-block chains ensuring

excellent mechanical properties of the material at high temperature as it can be seen from the two reflections pertinent to the hard segment crystals (cf. **Figure 4.5**).

4.3.3. Crystal structure of the stretched poly(ether ester amide)s

It is instructive to compare the highly oriented morphologies of the PEEAs with different soft-block lengths. The 2D WAXS patterns of the stretched PEEA films with 1000, 2000 and 2900 $g \cdot mol^{-1}$ soft segments containing the Gly-$Oxa_2$6-Gly monomer are presented in **Figure 4.6**B-D. For PEEAs **3a** and **3b** with short PTHF blocks of 1000 and 2000 the reflections of the hard-segment crystals are better visible on the diffractograms of oriented samples even at room temperature. Thus in **Figure 4.6**B-C the 200 and 220 peaks corresponding to the bisoxalamide unit cell can be safely identified on the equator. It is noteworthy that for the extruded monomer fibers both peaks are positioned on the meridian having a significant azimuthal spread (**Figure 4.6**A). The difference in orientation can be explained by the different mechanisms of molecular orientation during extrusion. As mentioned before, for the polymers stretched to high strains, the H-bonds (***a***-axis) in the hard block crystals are oriented perpendicular to the drawing direction. Such orientation is opposite to that of the extruded monomer fibers for which the beta-sheets are oriented along the extrusion direction (fiber axis), as shown in **Figure 4.6**A. This is probably due to the fact that the hydrogen bonds are already present in the melt[5,7] resulting in fast formation of the H-bonded sheets during the extrusion process.

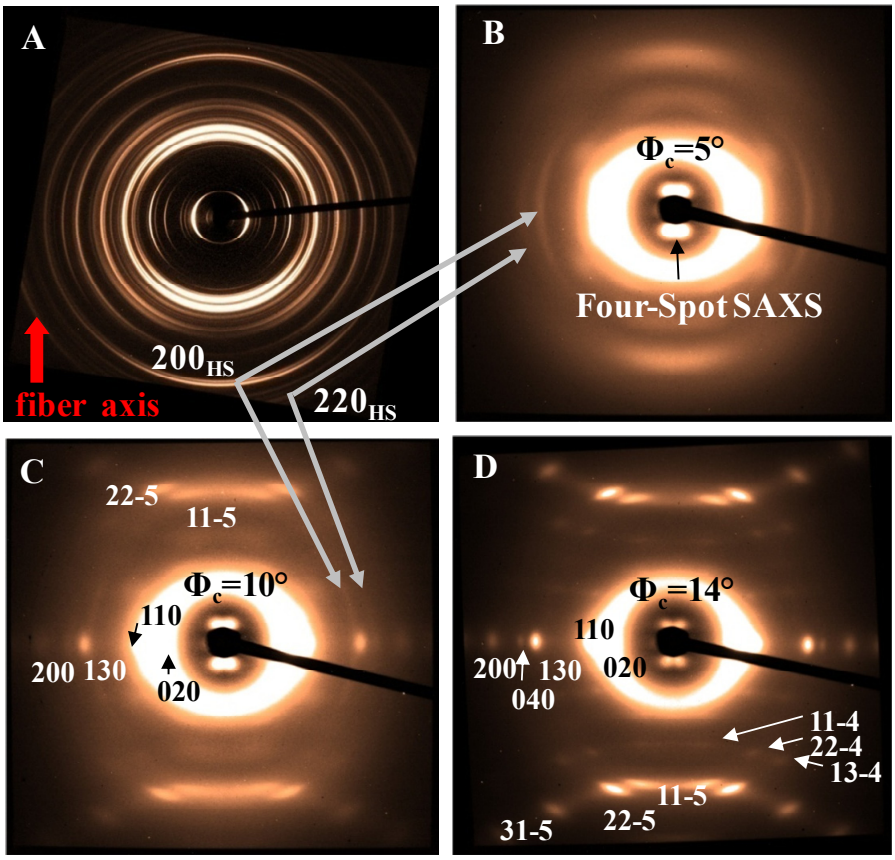

Figure 4.6. 2D-WAXS patterns corresponding to oriented monomer fiber Gly-Oxa$_2$6-Gly (A) and to the corresponding PEEA films with different soft segment lengths: **3a** (B), **3b** (C) and **3c** (D). For 2D patterns B-D the stretching direction is vertical. The peaks of the hard segment crystals are marked with subscripts "HS".

To address the difference of the soft-block crystallization in isotropic and oriented copolymers temperature-dependent SAXS/WAXS measurements were conducted. The heating ramps for sample **3c** are given in **Figure 4.7**. By monitoring the intensity of the strongest 020 and 110 reflections one can see that the melting temperature of the SS increases by more than 60 °C for the stretched copolymer compared to the isotropic material (cf. **Figure 4.7**A and C). Such dramatic increase was already reported for the TΦT-PTHF copolymer with the same soft block length.[7] Noteworthy, no SAXS signal is visible in **Figure 4.7**C for the heating ramp of the oriented sample due to the fact that the SAXS peaks inclined by 14° with respect to the meridian, which excluded them from the angular sector used for the 2D-to-1D data reduction.

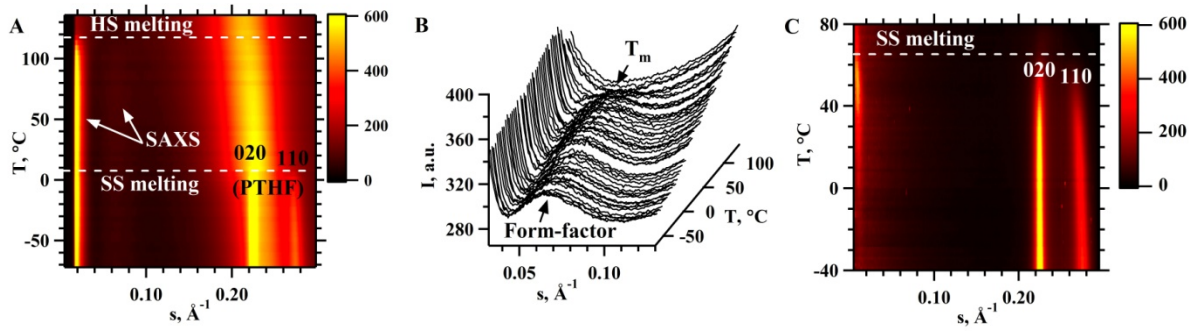

Figure 4.7. Temperature-dependent scattering patterns measured during a heating ramp at 5 °C·min^{-1} for the isotropic (A) and oriented (C) **3c** copolymers. B: Magnified SAXS region of the scattering curves in A centered on the maximum of the FF. The 2D diffractograms were reduced to 1D form using a sector of 5° around the equator for both, the isotropic and oriented, samples.

The PTHF crystal thickness was evaluated from the width of the 11-5 peak, which is positioned in the diffractograms close to the drawing direction. It is noteworthy that the determination of the crystal size from the strongest equatorial reflexes 020 and 110 is limited due to their superposition with the amorphous halo. The L_c-values together with T_m are given in **Table 4.2** for the isotropic and oriented copolymers **3b** and **3c**. For oriented sample **3a** with the shortest PTHF segment (1000 g·mol^{-1}) only a largely disordered chain conformation characterized by a single equatorial reflection and several diffuse layer lines on the meridian are observed (cf. **Figure 4.6**B). For a longer PTHF block with 2000 g·mol^{-1} **(3b)** the soft segment crystallizes upon drawing, which results in the increase of stress at break by 26% from 22.2 to 28.0 MPa.[19] By increasing the soft block length even further, i.e. from 2000 g·mol^{-1} to 2900 g·mol^{-1} **(3c)**, the crystal size obtained from the Scherrer formula for 11-5 reflection increases by about two times (from 28 to 54 Å). This can explain an additional increase of stress at break by 22% for sample **3c** in comparison to **3b**.[19]

Although the cross-links formed by soft segment crystals can account for the difference in stress at break of the studied polymers, the broad temperature-independent plateau and the Young's modulus in the range of 139 – 170 MPa are mainly determined by the cross-links associated with the hard segment crystals.[19] In the next section we address the peculiarities of the PEEA morphology and its correlation with the thermal history.

Table 4.2. Characteristics of the Soft Segment Crystals.

Sample	T_m, °C (ISOTR**)	T_m, °C (OR**)	L_c* (11-5), Å (OR**)
3b	-16.4	40	28
3c	3	65	54

*the crystal thickness values were obtained from the line broadening analysis performed for the 11-5 reflection of PTHF crystals;

**ISOTR and OR stand for the isotropic and oriented samples, respectively.

4.3.4. Copolymer morphology in relation to the sample thermal history

The L_c-values calculated from the position of the form-factor ripple as explained in the technical section. The 1D SAXS curves of the isotropic PEEAs **3a-c** comprising the Gly-Oxa$_2$6-Gly monomer are given in **Figure 4.8**A. The FF intensity decreases considerably with increasing of the hard-block content from 10.5 to 25.4% by weight. Moreover, the FF shows the same spacing of 24 Å as seen from **Table 4.3** for the different SS lengths. This shows that crystal thickness is invariant from the soft segment employed. The exact values of crystal thicknesses are slightly smaller than the projection of the ***c***-parameter on the ***b*c****-plane ($c\cdot\sin\beta$) of the corresponding monomer (the inter-layer spacing in the monomer crystal equals 27.3 Å). The difference of 3.3 Å can be accounted for by the exchange of the terminal methyl group by the soft PTHF segment during the melt esterification process.[19] All crystal thickness values of the studied samples are summarized in **Table 4.3**.

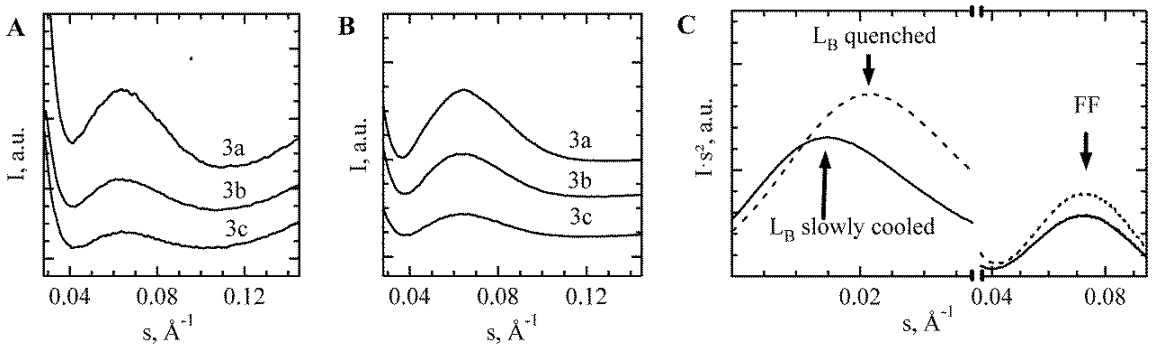

Figure 4.8. A-B: SAXS profiles of the isotropic and oriented PEEA films, respectively. C: Lorenz-corrected 1D SAXS curves for quenched (dashed line) and slowly cooled (solid line) sample **3a**.

Interestingly, for the stretched films (**Figure 4.8**B), the position of the FF ripple shifts to lower angles indicating that, together with improvement of their orientation, the thickness of the hard block crystals increases (see **Table 4.3**). Based on the fact that such "elongation" depends on the spacer length *p* (cf. **Figure 4.1**), one can suggest that the alkyl chains between the oxalamide units adopt a more strained conformation.

Table 4.3. Long Spacing (L_B), Crystal Thickness (L_c) and Amorphous Layer Thickness (L_a) of Isotropic and Oriented Segmented Poly(ether ester amide)s.

Sample	ISOTROPIC			ORIENTED			
	L_B, Å	L_c, Å	L_a, Å	L_B, Å	L_c, Å	L_a, Å	Φ_c
1	49.8	14.3	35.5	50.9	16.3	34.6	~5-10
2	52.6	17.4	35.2	47.7	19.1	28.6	~5-10
3a	57.5	24.0	33.5	57.3	27.7	29.6	~5-10
3b	71.4	24.0	47.4	63.1	26.8	36.3	~5-10
3c	79.0	24.0	55.0	78.4	26.8	51.6	~10-16
4	73.0	22.9	50.1	50.4	23.5	26.9	24
5	75.7	16.5	59.2	57.7	18.4	39.3	24

The strong intensity and well-defined shape of the FF observed in 1D SAXS curves testifies that the crystal thickness distribution is monodisperse and is determined by the primary chemical structure of the copolymers. This also could imply that crystal thickness is independent from the thermal history. To check this hypothesis, PEEA samples subject to different thermal treatments were studied. For example, 1D SAXS profiles of the quenched and slowly-cooled isotropic sample **3a** are shown on **Figure 4.8**C. One can notice that the value of the long spacing (L_B) owing to the electron density contrast of the microphase separated hard and soft domains changes while the crystal thickness does not vary. The L_B and L_c values for all samples with different thermal history are listed in **Table 4.4**. It should be mentioned that FF originates from the oxalamide crystals and there is no contribution from PTHF crystals, as it can be seen from the heating ramp experiment shown on **Figure 4.7**A-B where the FF of the hard block preserves above melting temperature of the soft block crystals.

Table 4.4. Long Spacing (L_B) and Crystal Thickness (L_c) for Slowly-Cooled Down and Quenched Isotropic Samples of Segmented Poly(ether ester amide)s.

	L_B, Å		L_c, Å	
Sample	S*	Q**	S*	Q**
1	53.3	46.7	14.1	14.0
3a	65.3	57.0	24.0	23.1
3c	83.3	75.0	22.4	22.3
4	77.8	59.9	21.4	20.6
5	83.9	80.5	15.9	15.7

*slowly cooled to RT;
**quenched to ice water

The chain tilt in the hard-block crystals can be evaluated from the four-spot SAXS patterns of highly oriented copolymers (e.g. **Figure 4.3**E). It is remarkable that Φ_c stays constant beyond the yield point during stretching, but the measured chain tilt values differ for various samples (see **Figure 4.9**). The chain tilt values for all the studied PEEAs are summarized in **Table 4.3**. We assume that in our case these angles represent the inherent feature of the bisoxalamide crystals and reflect the tilt of the polymer chains with respect to the basal crystal surface. This fact is reflected on the sketch in **Figure 4.4**C. It can be seen that the alignment of PTHF chains bridging the bisoxalamide segments makes all hard block crystals become inclined with respect to the drawing axis at a fixed angle Φ_c.

The occurrence of a chain tilt is believed to be accounted for by the necessity to accommodate the chain folds on the disordered fold surfaces. For polyethylene (PE) crystals of orthorhombic symmetry the chain tilt of 35°[18] is likely to be dictated by a large difference (~16.5%) between densities of amorphous and crystalline phases.[25] This is supported by the fact that some (unfolded) paraffins exhibit the same orthorhombic structure but do not have a chain tilt.[26] In contrast to PE, the orthorhombic crystals of polyhydroxybutyrate (PHB) characterized by a density difference with the melt state of only 7% are known to crystallize without chain tilt.[27] The existence of a chain tilt in PE lamellae upon drawing was reported by Peterlin *et al.*.[14] Importantly, the chain tilt in polyethylene single crystals can be different in crystallographically different sectors.[16] In recent simulations of deformation of polyethylene Rutledge *et al*.[28] have shown that the chain tilt in the lamella can remain constant during deformation.

In the present study, the value Φ_c is pertinent to the used hard-block segment and is relatively small (~5-16°) for the case of glycine end-group **(1-3c)** while it increases to 24° for segments with alanine **(4)** and propyl end–groups **(5)** (see **Table 4.3**).

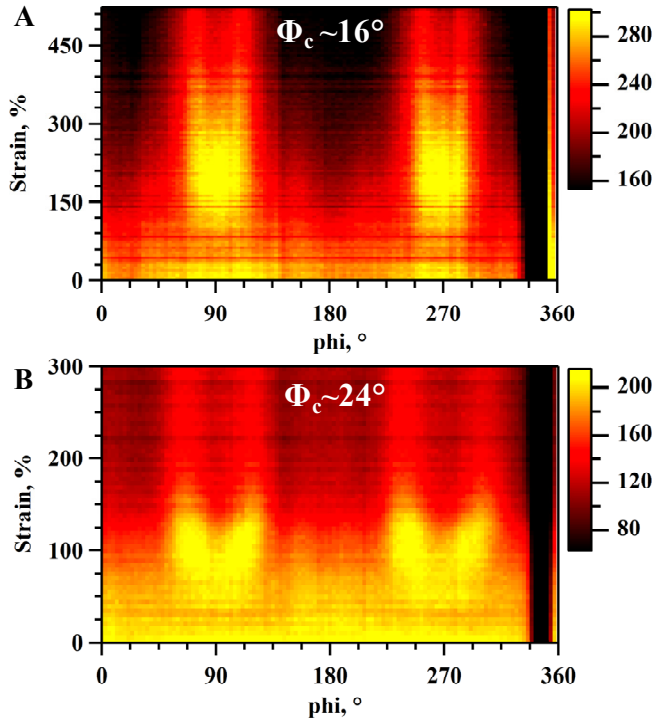

Figure 4.9. A-B: Azimuthal intensity profiles calculated for simultaneous SAXS/WAXS-stretching experiments in the s-range between 0.045 and 0.090. The patterns in A and B stand for samples **3c** and **4**, respectively.

4.3.5. Surface energy of the bisoxalamide crystals

In our study, we were interested in thermodynamics of the high-aspect-ratio hard-segment crystals which have the size of several nanometers in two dimensions (**Table 3.3.**). The melting enthalpy per mole of the hard-segment crystals, ΔH, derived from the DSC data (not shown here) are given in **Figure 4.10**A as a function of the spacer length p. The enthalpy for the bisoxalamide based crystals with the glycine end group **(1, 2** and **3a)** shows no change with the spacer length, whereas for the propyl end-group **(5)** and the alanine end-group **(4)** the enthalpy shows variation up to 30%, which testifies that the nature of the segment end-group plays a significant role.

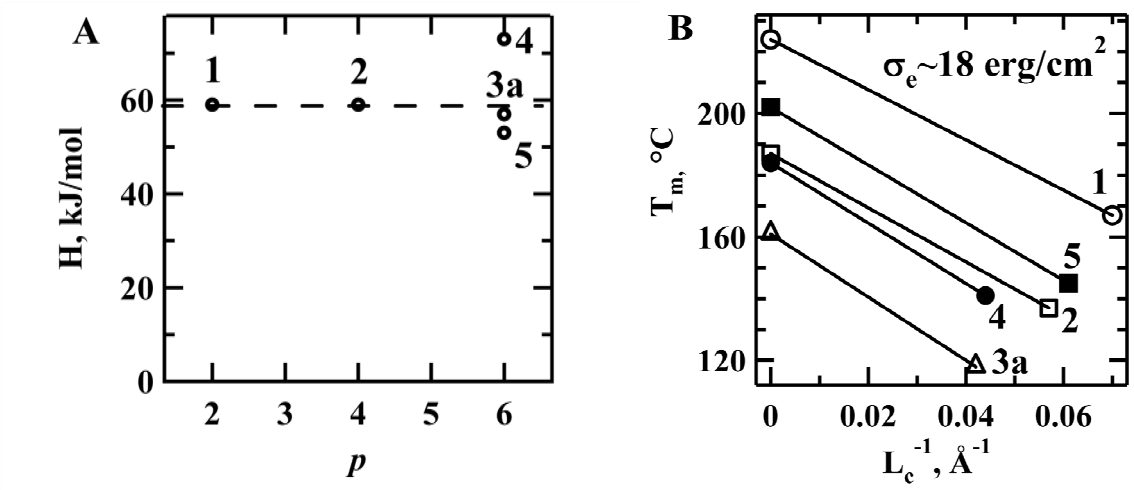

Figure 4.10. A: The melting enthalpy per mole of the hard segment crystals *vs.* spacer length *p*. B: Gibbs-Thomson plot showing the melting temperature *vs.* reciprocal crystal size. All copolymers have a short PTHF segment length of 1000 g·mol^{-1} **(1, 2, 3a, 4)** or 1100 g·mol^{-1} **(5)**.

Using the Gibbs-Thomson equation given as:

$$T_m = T_m^0\left(1-\frac{2\sigma_e}{\rho L_c \Delta H_f}\right) \tag{4.3}$$

the surface energy of the high-aspect-ratio hard-block crystals can be calculated. Since the exact equilibrium melting temperatures of the compounds is unknown, we have used instead the melting temperature of the corresponding monomers, forming macroscopically thick crystals.[19] It can be seen that the melting temperatures of the hard-segment crystals are only 20 °C lower than those of the corresponding monomers. When plotted in the Gibbs-Thomson coordinates, essentially the same slope is observed for copolymers with a similar PTHF length (**Figure 4.10**B). The estimated surface energy σ_e is 18 erg/cm^2, which is relatively low when compared to that of the conventional homopolymers.[29,30] Moreover since our crystals are needle-like,[23] this can make the efficient energy values even lower. In the literature, similar values were reported for polyamide 6,6 and were accounted for by a different crystallization mechanism similar to non-polymeric materials.[31] In our case, such low value is likely due to the entropic contribution of the soft segments forming tie chains bridging the neighboring crystals.

4.4. Conclusions

The case of a polymer system in which the crystal size is encoded in the primary chemical structure was studied using the example of TPEs consisting of alternating flexible PTHF segments and uniform glycine or β-alanine bisoxalamide units. We show that the thickness of

the hard-segment crystals is highly monodisperse and independent of the sample thermal history. The unit cell of the monomer consisting of a bisoxalamide array with a spacer length of six methylene units and capped with glycine end groups was analyzed based on selected-area electron diffraction and X-ray data. It was found to be monoclinic with parameters $\boldsymbol{a}$ = 5.09 Å, $\boldsymbol{b}$ = 10.88 Å, $\boldsymbol{c}$ = 27.73 Å and β = 79.6°.

The crystal orientation and phase transitions were addressed in simultaneous time-resolved X-ray scattering and mechanical stretching experiments. Starting from the soft-block length of 1000 $g \cdot mol^{-1}$, the elastomers crystallize upon stretching at ambient temperature. The melting temperature of PTHF crystals owing to the stress-induced crystallization increases by more than 60 °C with respect to the isotropic copolymers. During stretching of segmented PEEA copolymers two main morphologies were revealed: at low strains the hard segments in fibril-like crystals become oriented perpendicular to the flow direction due to their high aspect ratio, whereas at higher strains the crystal fragmentation sets in resulting in a change of the preferential stem direction to the one parallel to the drawing direction. The chain tilt in the bisoxalamide crystals was addressed from the characteristic four-spot SAXS patterns. It was found that it stays constant at high deformations. The tilting angle of the bisoxalamide unit with respect to the normal of the crystal basal plane is relatively small (~5÷16°) in the case of glycine end group and increases to 24° for the alanine and propyl segment. The bisoxalamide crystal surface free energy is found to be extremely low (~18 erg/cm^2), which is likely due to the entropic contribution of the tie PTHF chains bridging neighboring crystals.

4.5. Supporting Information

Table S4.1. Measured and Calculated *d*-Spacings (Å) extracted from X-ray Fiber Diffraction Experiments on Needle-like Crystals of Gly-Oxa$_2$6-Gly Monomer.

h	k	l	d_{exp}, Å	I	d_{calc}, Å
0	0	1	27.30	m	27.27
0	0	2	13.47	vs	13.64
0	1	1	10.37	m	10.11
0	0	3	9.33	m	9.09
0	0	4	6.72	s	6.82
0	2	0	5.77	w	5.44
0	0	5	5.38	s	5.45
0	2	2	5.18	w	5.05
1	0	0	4.98	w	5.01
1	1	1	4.64	w	4.61
1	1	2	4.46	s	4.54
1	1	-1	4.37	s	4.37
1	1	-2	4.12	s	4.12
1	0	4	4.02	s	4.43
1	2	2	3.76	m	3.68
0	1	7	3.61	w	3.67
0	3	3	3.44	w	3.37
0	0	8	3.37	s	3.41
1	1	6	3.21	w	3.52
0	3	5	3.13	vw	3.02
0	2	8	2.90	m	2.89
0	3	7	2.70	m	2.65
2	1	0	2.54	m	2.44
2	0	0	2.51	s	2.50
2	0	-2	2.39	w	2.39
2	1	-2	2.34	vw	2.33
2	2	2	2.30	w	2.31
2	2	0	2.25	vw	2.27
			ρ_{calc}=0.95 g/cm^3		

Table S4.2. Measured and Calculated *d*-Spacings (Å) extracted from X-ray Diffraction Experiments on Oriented PTHF Block of **3c.**

h	k	l	d_{exp}, Å	I	d_{calc},
0	2	0	4.41	vs	4.46
1	1	0	3.70	vs	3.66
1	3	0	2.38	s	2.39
0	4	0	2.22	w	2.23
2	0	0	2.00	m	2.01
1	1	-4	2.78	w	2.84
2	2	-4	2.30	w	2.30
1	3	-4	2.11	w	2.11
1	1	-5	2.19	s	2.23
2	2	-5	2.09	s	2.10
3	1	-5	1.82	m	1.82
0	2	5	1.63	w	1.63
Monoclinic unit cell C2/C (theoretical values)					
Lattice		a, Å	b, Å	c, Å	β, °
		5.61	8.92	12.25	134

4.6. References

(1) Eustache, R.-P. Fakirov, S., Ed.; Wiley-VCH: Weinheim, 2005; pp. 263–280.

(2) Guelcher, S. A. Tissue engineering. Part B, Reviews **2008**, 14, 3–17.

(3) Kojio, K.; Furukawa, M.; Motokucho, S.; Shimada, M.; Sakai, M. *Macromolecules* **2009**, *42*, 8322–8327.

(4) Versteegen, R. M.; Kleppinger, R.; Sijbesma, R. P.; Meijer, E. *Macromolecules* **2006**, *39*, 772–783.

(5) Sijbrandi, N. J.; Kimenai, A. J.; Mes, E. P. C.; Broos, R.; Bar, G.; Rosenthal, M.; Odarchenko, Y.; Ivanov, D. A.; Dijkstra, P. J.; Feijen, J. *Macromolecules* **2012**, *45*, 3948–3961.

(6) Niesten, M. C. E. J.; Feijen, J.; Gaymans, R. J. *Polymer* **2000**, *41*, 8487–8500.

(7) Niesten, M. C. E. J.; Harkema, S.; Heide, E. V. D.; Gaymans, R. J. *Polymer* **2001**, *42*, 1131–1142.

(8) Le Fevere de Ten Hove, C.; Penelle, J.; Ivanov, D. A.; Jonas, A. M. *Nature materials* **2004**, *3*, 33–7.

(9) Ivanov, D. A.; Bar, G.; Dosie, M.; Koch, M. H. J. *Society* **2008**, 9224–9233.

(10) Ivanov, D. A.; Hocquet, S.; Dosiére, M.; Koch, M. H. J. *The European physical journal. E, Soft matter* **2004**, *13*, 363–78.

(11) Yeh, F.; Hsiao, B. S.; Sauer, B. B.; Michel, S.; Siesler, H. W. *Macromolecules* **2003**, *36*, 1940–1954.

(12) Sauer, B. B.; Mclean, R. S.; Gaymans, R. J.; Niesten, M. C. J. E. *Journal of Polymer Science: Part B: Polymer Physics* **2003**, *42*, 1783–1792.

(13) Bonart, R. Journal of Macromolecular Science, Part B **1968**, 2, 115–138.

(14) Peterlin, A.; Baltá-Calleja, F. J. *Kolloid-Zeitschrift & Zeitschrift für Polymere* **1970**, *242*, 1093–1102.

(15) Peterlin, A. *Journal of Materials Science* **1971**, *6*, 490–508.

(16) Hocquet, S.; Dosie, M.; Thierry, A.; Lotz, B.; Koch, M. H. J.; Dubreuil, N.; Ivanov, D. A.; Dosière, M. *Macromolecules* **2003**, *36*, 8376–8384.

(17) Hocquet, S.; Dosiere, M.; Tanzawa, Y. *Macromolecules* **2002**, 5025–5033.

(18) Rosenthal, M.; Bar, G.; Burghammer, M.; Ivanov, D. A. *Angewandte Chemie* **2011**, *123*, 9043–9047.

(19) Sijbrandi, N. J.; Kimenai, A. J.; Mes, E. P. C. C.; Broos, R.; Bar, G.; Rosenthal, M.; Odarchenko, Y. I.; Ivanov, D. A.; Feijen, J.; Dijkstra, P. J. *Polymer* **2012**, *53*, 4033–4044.

(20) Chatani, Y.; Ueda, Y.; Tadokoro, H.; Deits, W.; Vogl, O. *Macromolecules* **1978**, *11*, 636–638.

(21) Franco, L.; Subirana, J. A. *Synthesis* **1998**, *9297*, 3912–3924.

(22) Armelin, E.; Alemán, C.; Puiggali, J. *The Journal of organic chemistry* **2001**, *66*, 8076–85.

(23) Odarchenko, Y. I.; Sijbrandi, N. J.; Rosenthal, M.; Kimenai, a J.; Mes, E. P. C.; Broos, R.; Bar, G.; Dijkstra, P. J.; Feijen, J.; Ivanov, D. A. *Acta biomaterialia* **2012** (accepted).

(24) Cesari, M.; Perego, G.; Mazzei, A. *Die Makromolekulare Chemie* **1965**, *83*, 196–206.

(25) Bassett, D. C. *Principles of Polymer Morphology*; Cambridge University Press: Cambridge, 1981.

(26) Ungar, G.; Keller, A. *Polymer* **1987**, *28*, 1899–1907.

(27) Barham, P. J.; Keller, A.; Otun, E. L.; Holmes, P. A. *Journal of Materials Science* **1984**, *19*, 2781–2794.

(28) Lee, S.; Rutledge, G. C. *Macromolecules* **2011**, *44*, 3096–3108.

(29) Harrison, I. R. Journal of Polymer Science Part A-2: Polymer Physics **1973**, 11, 991–1003.

(30) Hoffman, J. D.; Davis, G. T.; Lauritzen, J. I. *Treatise on Solid State Chemistry, Vol. 3*; Hannay, N. B., Ed.; Plenum Press: New York, 1975.

(31) Lee, S.; Phillips, P. *European Polymer Journal* **2007**, *43*, 1933–1951.

CHAPTER 5. ORIENTATION OF TYPICAL MAIN-CHAIN LIQUID-CRYSTALLINE POLYMERS UNDER CONFINEMENT: TRUE MOLECULAR EPITAXY VERSUS GRAPHO-EPITAXY. THE CASE OF POLY(DI-N-ALKYLSILOXANES)

Yaroslav Odarchenko,[a] Matthieu Defaux,[a] Martin Möller,[b] Dimitri A. Ivanov[a]

[a]Institut de Sciences des Matériaux de Mulhouse-IS2M, CNRS LRC 7228, Jean Starcky, 15, F-68057 Mulhouse, France

[b]Deutsches Wollforschungsinstitut an der RWTH Aachen e.V., Pauwelsstr. 8, 52074 Aachen, Germany

In this chapter, the chain orientation in thin films of poly(di-n-alkylsiloxanes) deposited on nanopatterned surfaces as well as the same polymers embedded in nanoporous templates is addressed by means of micro-focus and grazing-incidence X-ray diffraction and Atomic Force microscopy. It is shown that one carbon atom in the alkyl side-group attached to the siloxane backbone can switch by 90 degrees the in-plane orientation of the chains with respect to the PTFE rubbing direction. This fact is analyzed in terms of a mismatch between the contact planes of the siloxane and PTFE. The true molecular epitaxy is observed for the mismatch values less than 8%, while for the bigger values the orientation effect is only due to the grapho-epitaxy whereby the mesomorphic lamellae grow in the grooves resulting from the PTFE rubbing. Embedding the same polymers in nanoporous templates provides evidence of the grapho-epitaxy, with the mesomorphic lamellae orientating along the pore axis. In this case, the pores can be considered as a confinement medium analogous to a substrate with mesoscale grooves.

5.1. Introduction

Highly-oriented materials with hierarchical multiscale organization obtained through self-assembly hold promise for a variety of practical applications. In particular, controlling the structure of thin films and surfaces at spatial scales ranging from Angstroms to centimeters is found crucial for sensors,[1] light emitting diodes,[2] photovoltaic cells[3] and field-effect transistors.[4] The control of morphology and alignment in the course of crystallization is, however, not simple due to high free energy change associated to this phase transition. To this end, liquid-crystalline (LC) materials combining order and mobility at molecular and supramolecular levels can be employed. Generally, the LC alignment can be induced with the help of patterned substrates,[5,6] variety of external fields (e.g. magnetic[7,8], electric[9] or mechanical[10]) or by using porous templates.[11,12]

As far as patterned substrates are concerned, the dependence of the liquid-crystal orientation on spatially inhomogeneous surfaces is well known.[5,13] Berreman demonstrated that in the nematic phase *para*-azoxyanisole (PAA) accommodates planar orientation on rubbed solid surfaces or perpendicular to a surface which is inhomogeneous in two directions.[13]

Importantly, one can fabricate well-oriented highly crystalline material using the passage through a LC state. In the work of Maret and Blumstein, the alignment of thermotropic polyesters exhibiting nematic phase was performed with the help of magnetic field and shown to be preserved upon crystallization.[7] Our group has previously shown that the crystallization process can be efficiently controlled for a main-chain LC polymer, poly(di-*n*-propylsiloxane) (PDPS), by using a transient columnar mesophase.[14,15] In the work of Defaux *et al.*, rubbed PTFE surfaces have been successfully used to orient PDPS in thin films.[16] The polymer films deposited by spin-coating of toluene solution exhibit exclusively lamellar needles oriented perpendicular to the rubbing direction, i.e. with the siloxane backbones parallel to the PTFE chains.

In this section, the orientation of poly(di-*n*-alkylsiloxanes) family polymers containing side groups with two to six carbon atoms will be studied. In particular, thin films deposited on nanopatterned surfaces as well as embedded in nanoporous templates will be addressed by means of Grazing-Incidence and Micro-focus X-ray Scattering, as well as with AFM technique.

5.2. Experimental

5.2.1. Materials

Poly(di-*n*-alkylsiloxanes) samples with number of C atoms per alkyl side-chain from two to six were synthesized in the group of Prof. Martin Moeller (DWI at Aachen University, Germany) by anionic or cationic ring-opening polymerization of hexa-*n*-alkylcyclotrisiloxane as described elsewhere.[17] The polymer characteristics are given in **Table 5.1**. Two types of poly(di-n-alkylsiloxane) samples with the characteristic submicron size were prepared from 5 % wt polymer solutions in toluene. These are the samples spin-coated on PTFE-rubbed surfaces and obtained by wetting of the nanoporous alumina membranes. The PTFE rubbing was performed using a home-built machine operated at 300 °C at a deposition rate of 0.63 mm s^{-1}. During rubbing, a thin PTFE film is deposited on the substrate, in which the chains are aligned in the rubbing direction.[18] The Anodic Aluminum Oxide (AAO) templates with 200 and 35 nm pore size were supplied by Whatman Ltd. and SmartMembranes GmbH, respectively. The thickness of the template with 200 nm pores is 60 μm, while the one with 35 nm pores - 50 μm. The honeycomb morphology of the membranes consisting of isolated channels perpendicular to the surface was checked with SEM and SAXS techniques.

5.2.2. Methods

Atomic Force microscopy (AFM) experiments were carried out with a Nanoscope IV Multimode AFM (Veeco Metrology Group) in Tapping Mode, which is most suitable for soft materials imaging. Tapping mode Si probes from Nanosensors were used (PPP-NCL, resonant frequency 172-191 kHz, spring constant 33-47 N/m).

GIWAXS. The films on the PTFE-rubbed surface were analyzed using a grazing-incidence wide-angle X-ray diffraction setup. GIWAXS experiments were conducted at the X6B beamline of the National Synchrotron Light Source, Brookhaven National Laboratory, using X-ray energy of 15.8 keV. Samples were contained in a chamber with Kapton windows equipped with a computer-controlled heating stage Instec HCS402. The focused beam of 0.25 mm vertical × 0.5 mm horizontal was hitting the film at an incidence angle θ_{inc} of 0.2°. The 2D diffraction patterns were collected using a CCD detector from Princeton Instruments having a 120 mm × 120 mm image area (2084 × 2084 pixels). Each sample was measured in the machine direction (MD), i.e. when the beam is parallel to the rubbing direction, and in the transversal direction (TD), that is perpendicular to the rubbing sense.

Microfocus X-ray diffrection. Wetted porous templates were studied using micro-focus X-ray diffraction facility at the ID13 beamline of the European Synchrotron Radiation Facility. The measurements were performed in transmission with the pore axis normal to the X-ray beam using crossed-Fresnel optics and wavelength of 1.0 Å. The illustration of the experiment is shown in **Figure 5.1**. The images were recorded with a Frelon fast CCD with a pixel size of 50 microns (not rebinned) and a 16-bit readout. The spot size of the monochromatic X-ray beam at the focus point was about 1.0 micron along both axes. The norm of the scattering vector s ($s=2\sin\theta/\lambda$) was calibrated using diffraction pattern of corundum. The region of interest was selected with an on-axis optical microscope operated in reflection mode. A beam monitor installed upstream the sample provided dose-monitoring for online exposure normalization. The sample was scanned along the pore axis with help of an x-y gantry. The diffraction patterns were collected using a step of 1.0 μm. The data reduction and analysis including geometrical and background correction, visualization and the radial as well as azimuthal integration of the 2D diffractograms were performed using home-built routines designed in Igor Pro software (Wavemetrics Ltd.).

Table 5.1. Molecular weight distribution and thermal behaviour of poly(di-*n*-alkylsiloxanes) synthesized in the group of Prof. Martin Moeller (DWI, Aachen University, Germany).

Sample	number of C atoms per side-chain, *n*	M_w, kg/mol	PDI[a]	T_m,[b] °C	T_i,[c] °C
PDES	2	573	1.5	17	50
PDPS	3	461	1.6	70	224
PDBS	4	34	1.5	-19	310
PDPenS	5	325	1.3	-19	330
PDHS[d]	6	681	1.9	14	322

[a] polydispersity
[b] melting temperature, i.e. the transition from the crystal to mesophase
[c] isotropization temperature
[d] copolymer poly(di-pentyl/hexylsiloxane) with the monomer ratio of 10/90

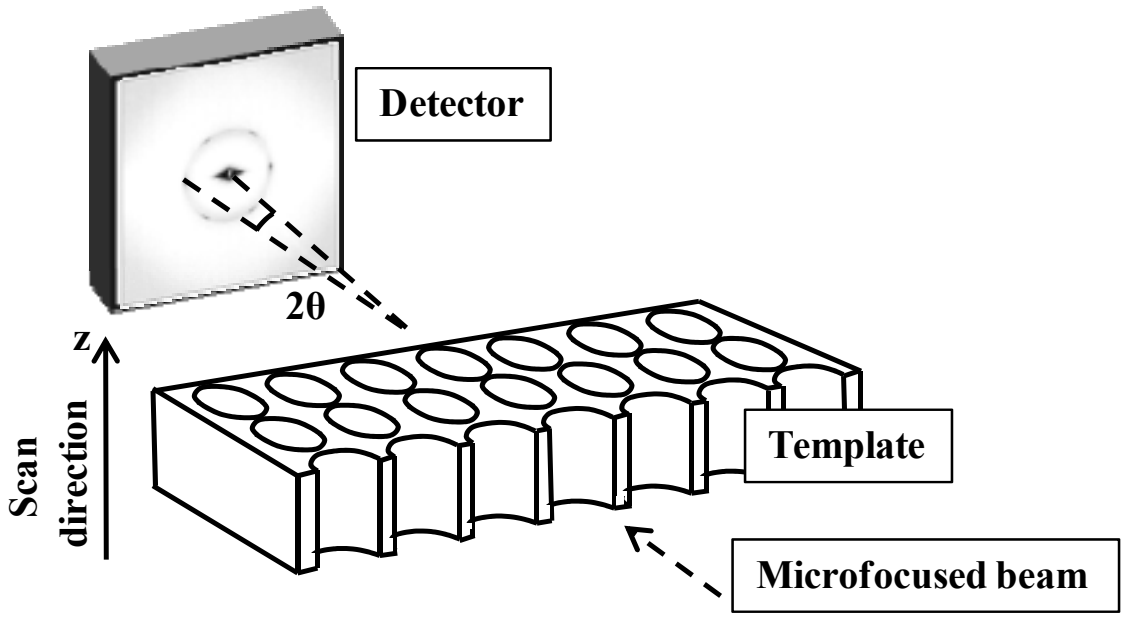

Figure 5.1. Schematic illustration of the X-ray microfocus experiment with the pore axis perpendicular to the X-ray beam.

5.3. Results and Discussion

5.3.1. True molecular versus grapho-epitaxy of poly(di-n-alkylsiloxanes) on nano-patterned surface

Poly(diethylsiloxane) (PDES) has a rather narrow mesophase stability window from –10 °C to 53 °C (**Table 5.1**). The particularity of this polymer opposed to the next member of the family (i.e. PDPS) is that it is mesomorphic at room temperature. The AFM micrograph of deposited PDES shows needles well oriented in the sense of rubbing (**Figure 5.2**F). Taking into account that the polymer chains are stacked perpendicular to the needle axis, one should observe preferential in-plane orientation by probing the film with the X-ray beam in the MD and TD directions. The 2D GIWAXS patterns reveal the characteristic reflections of a hexagonal mesophase which can be assigned to 10 peak (cf. **Figure 5.2**A). In the MD direction, the maximum intensity of the 10 peak is on the meridian indicating stacking of the columns parallel to the substrate. The absence of other peaks on the same arc suggests that PDES chains orient perpendicular to the needle axis. Indeed, in the TD pattern, the 10 reflections with equal intensities are observed at 60 ° with respect to each other, providing evidence that the (hk) plane of the hexagonal lattice is parallel to the rubbing direction. The resulting PDES film structure is schematically given in **Figure 5.3**A. Each mesomorphic column is shown by a cylinder, and it incorporates one individual polymer chain. The

lamellae grow along the rubbing direction, i.e. with the siloxane backbones perpendicular to the PTFE chains, which means that the orientation is defined by the substrate topography and not by the mismatch of the unit cells in the contact planes. The relation between PDES and PTFE chains can be defined as grapho-epitaxy.

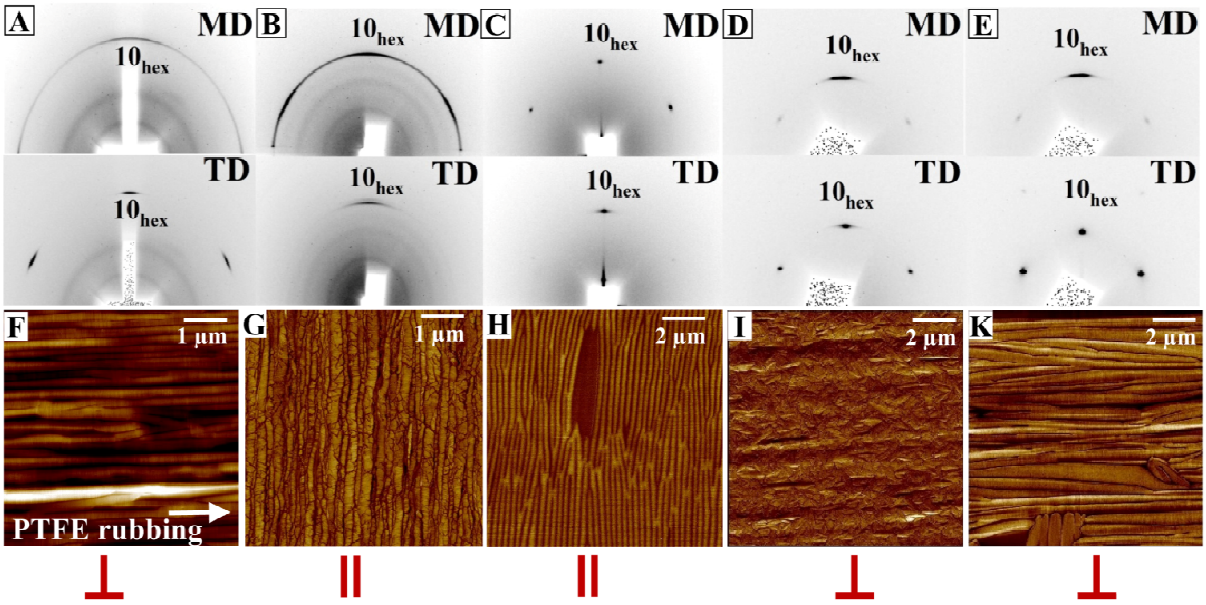

Figure 5.2. Top: 2D GIWAXS patterns of PDES (A), PDPS (B), PDBS (C), PDPenS (D) and PDHS (E) thin films deposited on PTFE-rubbed surface measured in the machine (**MD**) and transversal (**TD**) directions. Middle: AFM Tapping Mode micrographs of the PDES (F), PDPS (G), PDBS (H), PDPenS (I) and PDHS (K) showing lamellae (needle-like objects) grown on a PTFE-rubbed surface. The PTFE rubbing direction is close to horizontal (indicated with the white arrow). Bottom: the direction of the polymer backbones with respect to the PTFE chains of the substrate is indicated. All measurements were conducted at room temperature except GIWAXS for PDPS, which was performed at 90 °C.

When one adds one carbon atom to the side chain, i.e. by passing from PDES to PDPS, the in-plane columnar orientation is rotated by 90 ° and becomes parallel to the PTFE rubbing direction[16]. This can be seen from the corresponding GIWAXS patterns (**Figure 5.2**B) measured in the LC state at 90 °C above the crystal – mesophase transition (**Table 5.1**). Although, the diffracted intensity in the MD pattern is spread along the arc corresponding to the interplane distance of 9.70 Å, the characteristic three-spot pattern with comparable peak intensities can be still seen. The orientation is preserved upon crystallization when the sample is slowly cooled to the room temperature, as can be seen from the AFM micrographs of the needles grown perpendicular to the rubbing direction (cf. **Figure 5.2**G). Therefore, the perpendicular in-plane PDES chains arrangement with respect to the rubbing direction is opposite to that of PDPS depicted on **Figure 5.3**B.

Other polymers from the poly(di-*n*-alkylsiloxanes) family with longer side-chains, i.e. poly(dibutylsiloxane) (PDBS), poly(dipentylsiloxane) (PDPenS) and copolymer poly(di-pentyl/hexyl-siloxane) with the monomer ratio of 10/90 (denoted as PDHS) exhibit a LC state over a wide temperature range including room temperature (see **Table 5.1**). For PDBS with *n*=3 the interplane distance increases to 10.65 Å while the orientation of the chains is kept the same as for PDPS (cf. **Figure 5.2**C, H). Further increase in *n* results in a switch of orientation between PDBS and PDPenS, owing to the difference in the side-chain length. Despite the fact that AFM observations reveal numerous defects in the film organization, it is still possible to conclude that the PTFE rubbing direction has a significant impact on the PDPenS chains orientation (**Figure 5.2**I). The 2D GIWAXS patterns show that most of the lamellae are aligned perpendicular to the rubbing direction (**Figure 5.2**D), similarly to the case of PDES. At the same time, the X-ray measurements confirm the existence of orientational defects, which are directly visualized on the AFM micrograph. Notably, in the TD pattern, the meridional peak with the *d*-spacing of 11.78 Å is stronger and slightly wider than its two off-meridional counterparts, whereas they are expected to have identical intensity. The MD pattern displays a strong difference between the intensity of the meridional peak and the two counterparts. The probable explanation can be that the high nucleation rate of PDPenS on PTFE substrates limits the time of the mesophase growth and, hence, precludes the formation of well-organized lamellae.

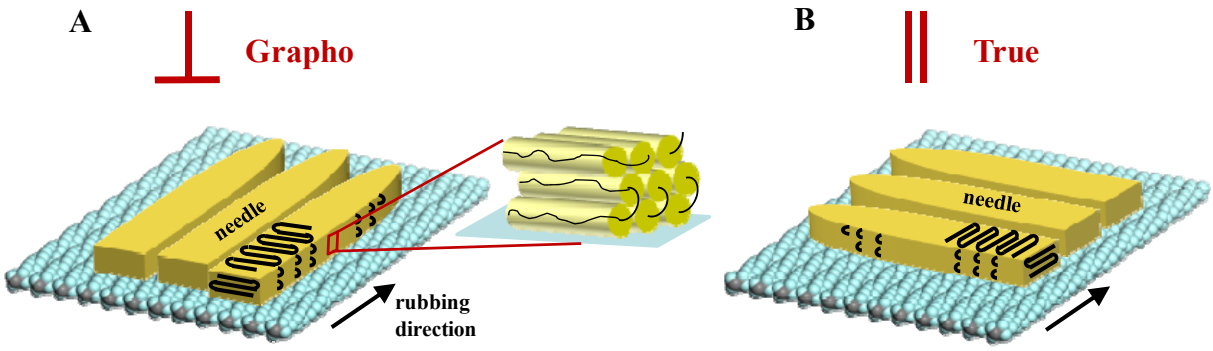

Figure 5.3. Two orientations of the poly(di-*n*-alkylsiloxanes) films. A: grapho-epitaxy (Grapho) when the polysiloxane backbone chains are perpendicular with respect to orientation of PTFE. The PTFE chain direction is indicated with black arrows. B: molecular epitaxy (True) when the siloxane backbone chains are parallel to the rubbed PTFE chains; For the sake of clarity, the polysiloxanes backbone is given in black.

By increasing the side-chain length further (the case of PDHS), the columnar orientation does not change anymore, according to the X-ray diffraction images given on **Figure 5.2**E.

This is also confirmed by the AFM micrograph on which well-pronounced needles parallel to the rubbing direction are seen (cf. **Figure 5.2**K). In this case, the polymer chains lie perpendicular to the rubbing direction, as schematically illustrated in **Figure 5.3**.A.

Our findings clearly show that one CH_2 group in the side-chains can switch the in-plane orientation of the polymer chains. Therefore, we can claim that our surface-induced orientation is sensitive to the smallest possible modification of the polymer architecture.

Table 5.2. Correlations between the mismatch of the poly(di-*n*-alkylsiloxanes) and PTFE unit cells and their relative orientation.

Sample	*n*	*a*, Å	PTFE Mismatch(%) with respect to a_{PTFE}=5.6 Å	*c*, Å	PTFE Mismatch(%)with respect to c_{PTFE}=19.5 Å	Relative orientation
PDES	2	9.3	21.9	5	2.5	⊥
PDPS	3	11.2	1.3	5	2.5	II
PDBS	4	12.3	7.8	5	2.5	II
PDPenS	5	13.6	16.6	5	2.5	⊥
PDHS	6	14.6	22.3	5	2.5	⊥

We attempted to rationalize the behaviour of poly(di-*n*-alkylsiloxanes) deposited on PTFE-rubbed surfaces in terms of a mismatch between the unit cell parameters. It is well documented that PTFE in the bulk can reach crystallinity on the order of 93-98 %. The sterical constraints imposed on the chain by the size of fluorine atoms leads a helical conformation of the chain instead of a planar zigzag, as is the case of PE.[19–21] The PTFE is believed to exist in a hexagonal phase at room temperature, the so-called phase IV ($a = b$ = 5.6 Å, c = 19.5 Å; helix 15_7).[21] Above 30 °C it undergoes a transition to form I which has an increased concentration of motion defects accompanied by partial untwisting of the chain, although not achieving the planarity of the PE chain. The analysis of the unit cell mismatch calculated for the form IV of PTFE crystal are given in **Table 5.2**. It should be noted that the mismatch values take into account the temperature effect of LC phase and thus correspond to the temperature at which the samples were analyzed. One can clearly see that the backbones of poly(di-*n*-alkylsiloxanes) and PTFE are parallel for the polymers having the smallest lateral mismatch values (<= 7.8 %). All the studied poly(di-*n*-alkylsiloxanes) are considered to have

the cis-trans conformation of the backbone upon the mesophase formation (5.0 Å). Therefore, along the chains the mismatch for PDPS and PDBS with respect to PTFE crystals will be not more than 2.5 % which can be considered as a "true" molecular-epitaxy (**Figure 5.3**B). Nevertheless, due to motion defects appearing in the PTFE chain when the temperature increases, the register between the *c*-parameters of the unit cell cannot be considered seriously. For the other three samples, i.e. PDES, PDPenS and PDHS, the preferential orientation on PTFE is perpendicular to the rubbing direction and can be qualified as grapho-epitaxy (cf. **Figure 5.3**A).

5.3.2. Impact of the film thickness on the surface-induced orientation: the case of thin PDES films

Controlling the film structure on a large scale is crucial for many applications. As shown previously, the lamellar alignment of poly(di-*n*-alkylsiloxanes) deposited on substrates can be induced by the PTFE rubbing. It is instructive to evaluate the maximum film thickness to which the surface-induced orientation propagates. To this end, the experiments were carried out on films of different thickness. The samples were prepared by both spin-coating and drop-casting. AFM imaging was used to characterize the surface structure as exemplified on **Figure 5.4**.

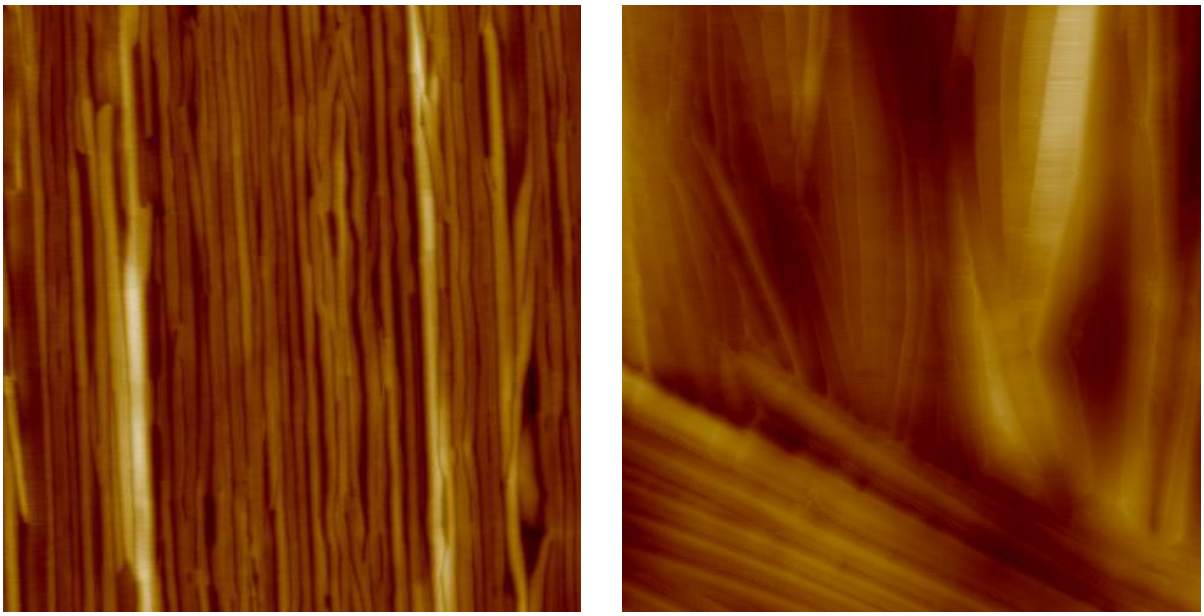

Figure 5.4. Tapping Mode Height AFM images (10 x 10 μm^2) of PDES thin films deposited on a PTFE rubbed surface. The film thicknesses is 0.85 µm (left) and 2.5 µm (right).

It turns out that PDES thin film substrate-orientation can be preserved for thicknesses comprised between 60 nm and 800 nm. Below 60 nm, the film starts to dewet the substrate several minutes after preparation. At 1 μm thickness, the orientational defects become frequent. These defects look like short needles growing perpendicularly to the PTFE rubbing. Also, the average lamellar height (or the width of the needles) increases. For the films of 2.5 μm thickness, the lamellar orientation parallel to the rubbing direction is largely lost. Although the rubbing direction is still easily detectable the surface topography dramatically changes. The needles are now grouped in bundles in which they are stacked parallel to each other and oriented in different directions.

The above discussion prompts us to assume that the surface-induced orientation is mostly operational in the close vicinity of the interface surface/polymer, which is natural. The results thereby explain the limited impact of the substrate on thicker films. Importantly, to be oriented, the poly(di-*n*-alkylsiloxanes) need to nucleate and grow at a moderate rate. In these conditions, the structural defects do not impede the alignment on the PTFE substrate.

5.3.3. Effect of the pore size on polymer orientation in nanoporous templates

By confining the LC polymers in nanoporous templates one can expect to induce orientation due to the geometrical constraints imposed by the pore walls. To explore this effect, we performed an X-ray microfocus scan across the membrane with 200 nm pores impreganted with PDES, as shown in **Figure 5.5**C. The extent of filling of the membrane pores with the polymer can be appreciated by comparing the SAXS signal originating from the AAO template and 10 reflection from the hexagonal mesophase of PDES. The 2D microfocus X-ray patterns corresponding to the overplayed PDES film (i.e. the one on the top of the membrane) and to PDES located inside the pores are exemplified on **Figure 5.5**A-B. **Figure 5.5**A shows the 10 reflection corresponding to the intercolumnar distance of 9.3 Å with two clear maxima situated on the meridian. Such orientation is similar to the one reported for thin films on rubbed PTFE surface and can be viewed as a layer-like packing of the backbone siloxane chains with $\mathbf{10}_{hex}$ vector normal to the substrate (**Figure 5.6**A).[16] Importantly, for PDES embedded inside the pores the diffraction pattern does not change (cf. **Figure 5.5**B). It can be assumed that the layers in the pore are preferentially parallel to the surface of the AAO membrane due to the epitaxy with the polymer chains on the top surface as illustrated in **Figure 5.6**A-B. The alike behaviour is observed for all the studied

polysiloxanes such as PDPS, PDBS, PDPenS and PDHS that exhibit the columnar diameters comprised between 11.2 and 14.6 Å (see **Table 5.2**).

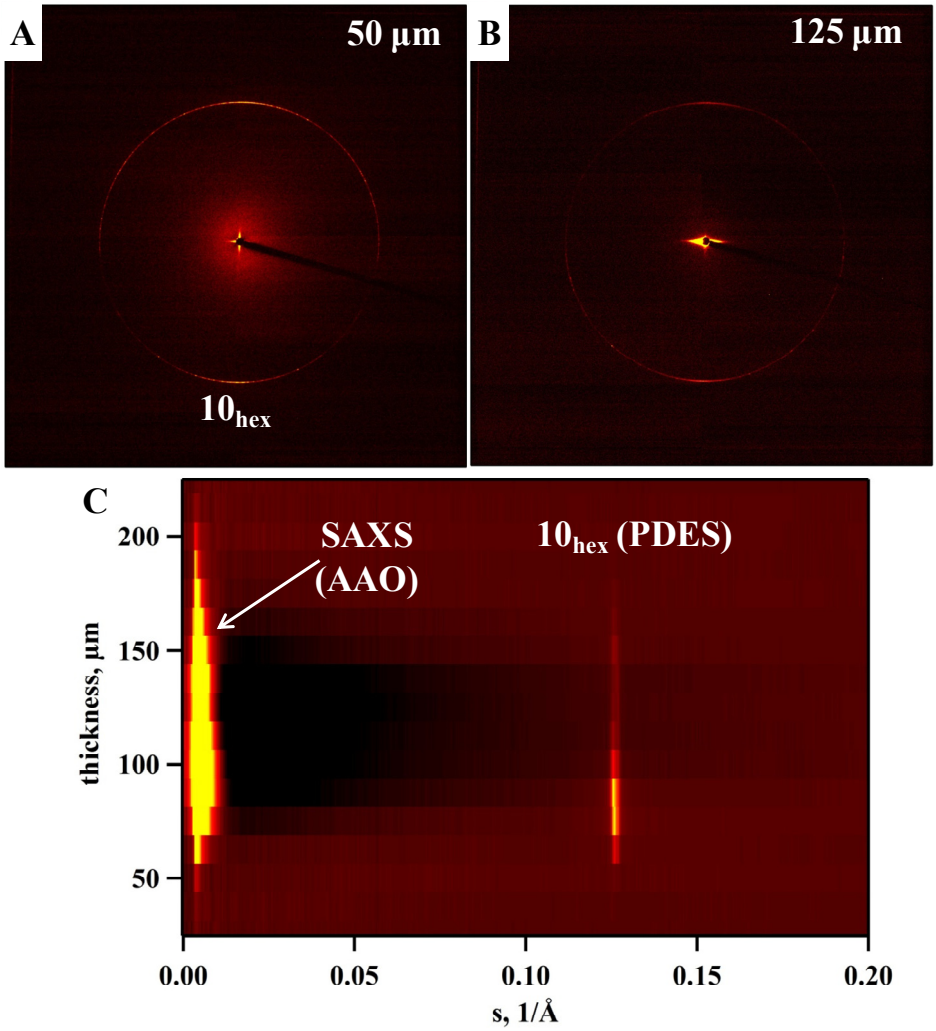

Figure 5.5. 2D Microfocus X-ray patterns measured on a PDES thin film close to the surface (A) and in the nanoporous template with 200 nm pore size (B). Pore axis is vertical. 1D-reduced intensity measured during the microfocus scan across the polymer-impregnated template (C).

When the pore size is decreased to 35 nm one observes a six-spot pattern with the diffraction peaks situated at 60° with respect to each other starting from the equatorial direction. A typical 2D diffractogram corresponding to the PDES film is shown on **Figure 5.7**A. This pattern orientation is not typical for the case of thin films deposited on a horizontal substrate (cf. **Figure 5.2**A-E). In the case of the template-impregnated PDES, the well-oriented pattern with unusually-oriented distinct 10 siloxane reflections (cf. **Figure 5.7**) prompts us suggesting that the grapho-epitaxy with the pore walls takes place. Thus, one would expect the mesoscopic lamellae growing strictly along the pores direction, i.e. with one of the $\mathbf{10}_{hex}$ vectors of the columnar phase oriented perpendicular to the pore axis (see **Figure**

5.6B-C). We speculate that this change in orientation is due to geometrical constraint imposed by the pores with a small diameter. Thus, the pore curvature guides mesoscopic lamellae to grow exclusively in the direction of pore length, which can be considered as infinite as compared to the perimeter of the pore wall. Noteworthy, the same result was also obtained for other polymers of the poly(di-*n*-siloxane) family, i.e. for PDPS, PDBS, PDPenS and PDHS.

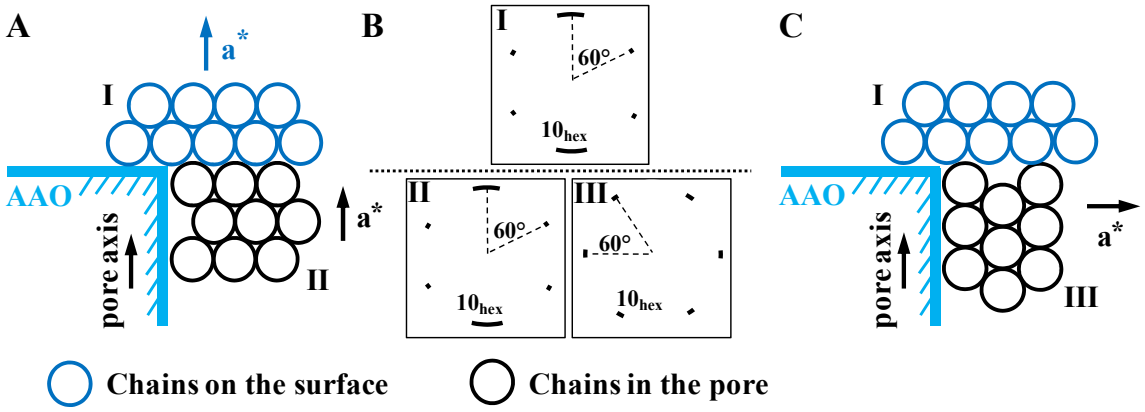

Figure 5.6. Cartoon showing two different orientations of the poly(di-*n*-alkylsiloxanes) LC lattice. The layers formed by the polysiloxane chains in the 200 nm pores are perpendicular (A) and in the 35 nm pores are parallel (C) to the pore axis. (B) Schematic 2D diffraction patterns from the LC columnar phase on the surface of the membrane (**I**) and inside the 200 nm (**II**) and 35 nm (**III**) pores.

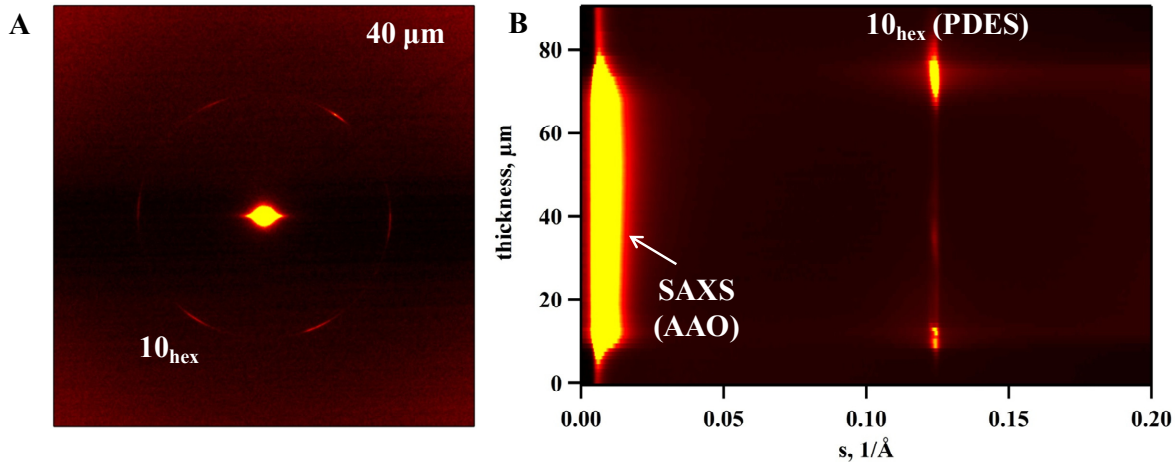

Figure 5.7. 2D Microfocus X-ray patterns measured on a PDES-impreganted nanoporous template with 35 nm pore sire (A). Pore axis is vertical. 1D-reduced intensity measured during the microfocus scan across the polymer-impregnated template (B).

5.4. Conclusions

In this chapter, we describe a comparative study of the texture of poly(di-*n*-alkylsiloxanes) thin films deposited on nanopatterned substrates and impregnated in nanoporous templates.

These two cases allow us to get insights about the mechanisms of the liquid-crystalline orientation under 2D and 1D confinement.

For the PTFE-rubbed substrates, two in-plane orientations are observed, depending on the diameter of the mesomorphic columns. The PDPS (n = 3) and PDBS (n = 4) films align with their main chains parallel to the rubbing direction. All other polymers having 2, 5 or 6 carbon atoms in the side-chain orient in the perpendicular direction. The inter-columnar parameter of both siloxane polymer and PTFE are nicely matched for the case of PDPS and PDBS, which are considered to reveal a truly molecular epitaxy. For the other cases, the unit cell parameters exhibit a mismatch exceeding 8 %. Therefore, the alignment of the mesomorphic lamellae along the rubbing direction is supposedly guided by the topology of the rubbed surface (grooves) resulting in perpendicular orientation of the polymer backbones with respect to the PTFE chains. The grapho-epitaxy is also found to take place in nanoporous templates with the pore diameter of 35 nm owing to geometrical confinement imposed by the pore curvature. In contrast to the rubbed surface, which can be regarded as infinite in 2D, the perimeter of the pore walls is very small, which precludes all lamellar orientations except the one with the growth direction parallel to the pore axis. Finally, experiments performed on PDES have shown that the high quality orientation induced by the PTFE rubbing was maintained up to the film thicknesses of approximately 1 micron.

5.5. References

(1) Bearzotti, A.; Bertolo, J. M.; Innocenzi, P.; Falcaro, P.; Traversa, E. *Journal of the European Ceramic Society* **2004**, *24*, 1969–1972.

(2) Tang, C. W.; VanSlyke, S. a. *Applied Physics Letters* **1987**, *51*, 913.

(3) Schmidt-Mende, L.; Fechtenkötter, A.; Müllen, K.; Moons, E.; Friend, R. H.; MacKenzie, J. D. *Science (New York, N.Y.)* **2001**, *293*, 1119–22.

(4) Dimitrakopoulos, B. C. D.; Malenfant, P. R. L. **2002**, 99–117.

(5) Ong, H. L.; Hurd, A. J.; Meyer, R. B. *Journal of Applied Physics* **1985**, *57*, 186.

(6) Lee, B. W.; Clark, N. a *Science (New York, N.Y.)* **2001**, *291*, 2576–80.

(7) Maret, G.; Blumstein, A. *Molecular Crystals and Liquid Crystals* **1982**, *88*, 295–309.

(8) Gopinadhan, M.; Majewski, P. W.; Osuji, C. O. *Macromolecules* **2010**, *43*, 3286–3293.

(9) Kim, J.-H.; Yoneya, M.; Yokoyama, H. *Nature* **2002**, *420*, 159–62.

(10) Twomey, C.; Blanton, T.; Marshall, K.; Chen, S.; Jacobs, S. *Liquid Crystals* **1995**, *19*, 339–344.

(11) Steinhart, M.; Zimmermann, S.; Göring, P.; Schaper, A. K.; Gösele, U.; Weder, C.; Wendorff, J. H. *Nano letters* **2005**, *5*, 429–34.

(12) Ha, K.; Ahn, H.; Son, C. *Liquid crystals* **2006**, *33*, 935–940.

(13) Berreman, D. *Physical Review Letters* **1972**, *28*.

(14) Gearba, R. I.; Dubreuil, N.; Anokhin, D. V.; Godovsky, Y. K.; Ruan, J.-J.; Thierry, A.; Lotz, B.; Ivanov, D. a. *Macromolecules* **2006**, *39*, 978–987.

(15) Gearba, R. I.; Anokhin, D. V.; Bondar, A. I.; Godovsky, Y. K.; Papkov, V. S.; Makarova, N. N.; Magonov, S. N.; Wim Bras, O.; Koch, M. H. J.; Masin, F.; others *Macromolecules* **2006**, *39*, 988–999.

(16) Defaux, M.; Vidal, L.; Möller, M.; Gearba, R. I.; Dimasi, E.; Ivanov, D. A. *Macromolecules* **2009**, *42*, 3500–3509.

(17) Out, G. J. J. Poly(di-n-alkylsiloxane)s, Synthesis and Molecular Organization, University of Twente, The Netherlands, 1994.

(18) Wittmann, J. C.; Smith, P. *Nature* **1991**, *352*, 414–417.

(19) Eby, R. K.; Clark, E. S.; Farmer, B. L.; Piermarini, G. J.; Block, S. *Polymer* **1990**, *31*, 2227–2237.

(20) Clark, E. S. **1999**, *40*, 4659–4665.

(21) Clark, E. S. Journal of Macromolecular Science, Part B **2006**, 45, 201–213.

CHAPTER 6. CONFINED CRYSTALLIZATION OF A LIQUID-CRYSTALLINE/SEMICRYSTALLINE BLOCK COPOLYMER FORMED THROUGH COMPLEXATION OF POLY (2-VINYLPYRIDINE-B-ETHYLENE OXIDE) WITH A WEDGE-SHAPED MESOGEN

Yaroslav Odarchenko[a], Jingbo Wang[b], Matthieu Defaux[b], Denis Ahokhin[a], Janis Lejnieks[b], Helmut Keul[b], Martin Möller[b], Ahmed Mourran[b], Dimitri A. Ivanov[a]

[a]Institut de Sciences des Matériaux de Mulhouse-IS2M, CNRS LRC 7228, Jean Starcky, 15, F-68057 Mulhouse, France;

[b]DWI at RWTH Aachen University and Institut für Technische und Makromolekulare Chemie der RWTH Aachen University, Forckenbeckstr. 50, D-52056 Aachen, Germany;

The semicrystalline – liquid crystalline diblock copolymer formed by complexation of a wedge-shaped molecule, 4'-(3'',4'',5''-tris(octyloxy) benzamido) propanoic acid, with PEO-P2VP copolymer is studied in this section. The complexed P2VP block forms smectic liquid-crystalline layers causing segregation of the PEO block. Due to incompatibility between the blocks, the morphology depends on the molar ratio ligand/pyridine (x). For $x \geq 0.5$, PEO forms cylinders within the LC-matrix. The phase segregation strongly shifts the crystallization temperature to lower values and forces PEO to crystallize within the block copolymer cylinders. In thin films, the alignment of the smectic layers parallel to the substrate induces homeotropic orientation of the PEO cylinders. At the same time, the crystalline stems preferentially orient parallel to the smectic normal. For $x \leq 0.33$, PEO forms crystalline lamellae within the LC-matrix and crystallization dominates the final structure.

6.1. Introduction

Block copolymers have been attracting the attention of polymer scientists during the last decades because of their interesting properties and potential applications in the growing field of nanotechnology.[1] Semicrystalline block copolymers containing one crystallizable block is an important family of block copolymers, for which complex hierarchical ordering and competition between microphase separation and crystallization on different length scales are observed.[2–8] The semicrystalline block can crystallize in the nanoconfined environment, whereby the crystallization mechanism is controlled by the block copolymer morphology, the crystallization behavior of the semicrystalline block, and glass transition of the amorphous block. Depending on the interplay between these factors, two confinement regimes (hard and soft confinement) with different crystallization mechanisms are observed.[4,9,10] In "hard confinement regime" the crystallization can remain restricted within the microphase separated regions either when the amorphous segment is glassy ($T_{ODT} > T_g > T_c$) or for strongly microphase separated blocks[9] (large values of χ). In contrast, if the amorphous block is in the rubbery state at the crystallization temperature ($T_{ODT} > T_c > T_g$) or if the driving force of the microphase separation is weak, the diblock copolymer structure can be ruptured by the crystallization process resulting in the so-called "break-out crystallization"[11]. The latter case is termed "soft confinement regime". In general, various nanoconfined environments (such as spheres,[8] cylinders,[7,8] and lamellae[3,5,6]) can be yielded by the microphase separation of diblock copolymers; these morphologies can be associated to heterogeneous or homogeneous nucleation mechanisms.

In the liquid-crystalline (LC)-semicrystalline block copolymers, hierarchically-ordered structures are expected with the characteristic scale of the LC ordering comprised between 1 and 10nm and that of the microphase separated domains from 10 to 100nm. It is expected that crystallization of the crystallizable block can be confined by the mesomorphic matrix. Recently, Zhou et al. showed that the crystallization behavior of a semicrystalline block such as PEO was controlled by the weight fraction of the LC segment in the block copolymer.[9] Thus, if the LC weight fraction is less than 50%, PEO crystallizes in the "LC lamellae in PEO lamellae" structure at normal undercoolings, while for high LC contents (LC>50%) PEO crystallizes only at very large undercoolings and forms the "PEO cylinders in LC matrix" structure.

A possible interest of hierachical ordering of the diblock copolymer is in effortless tuning of the microdomain orientation in thin films, which is important for practical applications.

The mesogenic block orients parallel to the SiO_2 interface as well as at the air interface, leading to formation of microdomains parallel to the substrate.[12,13]

The LC ordering can be introduced via covalent bonding[14] or via supramolecular self-assembly[15–17]. In the latter case, a mesogen is selectively complexed with one segment of the block copolymer to render it liquid crystalline via non-covalent bonds such as ionic interactions, hydrogen bonding or charge-transfer interactions.[15–20] The mesostructures based on ionic interactions are typically thermally stable and in some cases the complexes decompose before reaching the isotropic phase.[21–24] Recently, poly(2-vinylpyridine) (P2VP) have been complexed with a wedge-shaped ligand consisting of a sulfonated group at the tip and a large non-polar body.[25] In this situation, the final morphology of the system can be influenced by the shape of the mesogen and degree of complexation. In addition, incorporation of such a ligand in a miscible P2VP – PEO diblock copolymer[26] promotes the phase segregation between the blocks.[27] In thin films, smectic ordering of the ligand takes place with the layers oriented perpendicular to the interface between the blocks resulting in cylinders or lamellae perpendicular to the air/substrate interface.

The complexes based on hydrogen bonds are particularly interesting since binding is thermally reversible, selective and directional.[15,16] In the present paper, we focus on the P2VP-PEO block copolymer complex with a new ligand, 4′-(3″,4″,5″-tris(octyloxy) benzamido) propanoic acid. The structure and thermotropic transitions of some molecules of this homologous series were recently reported.[28] Here, the bulk structures of the complex with both P2VP homopolymer and P2VP-containing block copolymer have been investigated. The complexation is found to depress the T_g of the glassy block and induce the formation of a LC phase, which in turn confines the PEO crystallization and results in crystal orientation in thin films. Also, the segregation strength between the blocks varies with the complexation degree, the fact that provides a possibility to control the morphology and orientation of the mono-domains in the thin films. These findings open new opportunities in tuning the crystallinity and crystal orientation, which is crucial for several practical applications such as solid-state electrolytes for lithium batteries.[29]

6.2. Materials and Methods

6.2.1. Materials

$P2VP_{350}$ homopolymer (M_n = 35000, M_w/M_n = 1.07) was purchased from Sigma-Aldrich, diblock copolymer $P2VP_{150}$-PEO_{550} with M_w/M_n = 1.18 was synthesized by sequential anionic polymerization.[27] The 4′-(3″,4″,5″-tris(octyloxy) benzamido) propanoic acid (C8-Ala-COOH, **Scheme 6.1**) was used as a ligand and is denoted as **L**. The details of the synthesis were published elsewhere.[28] Silicon wafers (100) were purchased from CrysTec GmbH. Chloroform (p.a.) and isopropanol (p.a.) were supplied by VWR International and used as received.

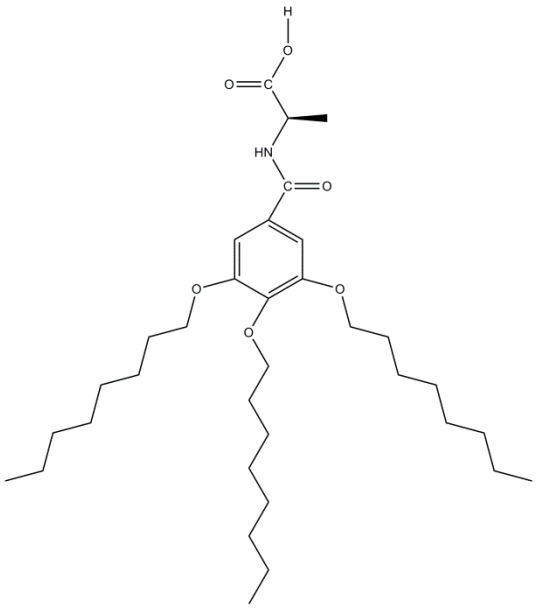

Scheme 6.1. Chemical structure of the ligand **L**.

Preparation of Polymer Complex. The preparation procedure of block copolymer/ligand complex or homopolymer/ligand complex is similar to the one reported in the literature.[27] The complexes are denoted as P2VP(**L**)$_x$ and P2VP(**L**)$_x$-PEO for the homopolymer/ligand and block copolymer/ligand, respectively, where x is the degree of complexation, defined as the molar ratio of the **L** and pyridine moieties.

Film Preparation. Silicon wafers having a ca. 2 nm thick native silicon oxide layer are used as substrates. Before experiments, they were cleaned by sonication in isopropanol for 5 minutes, followed by drying in N_2 stream, and activated with UV/O_2 for 12 minutes. All the substrates were used immediately after the UV/O_2 treatment. The polymer complex was

dissolved in chloroform at concentration of 3 wt%. The solution was spun cast (Convac 1001S, Germany) onto freshly prepared silicon wafers at a speed of 2500 rpm for 30 s to result in film thickness of ca. 220 nm. The film thickness was measured by ellipsometry (MM-SPEL-VIS, OMT GmbH). Before spin-coating, the solutions were filtered through 0.2 μm PTFE syringe filters. Thermal annealing of the films was performed under vacuum (2×10^{-2} mbar) at 100°C (i.e., below the isotropic temperature of the complex) for different times. After thermal annealing, the films were quenched to ambient temperature by quickly transferring them onto a steel plate.

6.2.2. Methods

Fourier Transform Infrared Spectroscopy (FTIR) spectra with a resolution of 4 cm^{-1} were recorded with a Nicolet NEXUS 670 Fourier Transform IR spectrometer. The samples were prepared by drying several droplets of 3 wt% solution on KBr plates at room temperature. For each spectrum more than 200 scans were acquired to enhance the signal-to-noise ratio.

Differential Scanning Calorimetry (DSC) measurements were performed on a Netsch DSC 404 instrument under N_2 stream. The instrument was calibrated with pure indium. For measurements, about 3 mg of the studied complex was sealed in aluminum pans. The samples were heated to 150 °C, kept at that temperature for 2 minutes to erase the thermal history and then cooled to -50 °C at a rate of 10 °C·min^{-1}. Subsequently they were heated to 150 °C at a rate of 10 °C·min^{-1} to analyze the melting behavior of the complex. The PEO crystallinity was calculated according to the following equation:

$$Cr = \frac{\Delta H_f}{w \cdot \Delta H_0} \times 100\% \qquad (6.1)$$

where ΔH_f is the measured heat of fusion per one gram of sample, w is the weight percentage of PEO in the block copolymer complex and ΔH_0 is the thermodynamic heat of fusion per gram of completely crystalline PEO, which equals 203 J·g^{-1}.[30]

Wide-Angle X-ray Scattering (WAXS) measurements were carried out using a custom-built SAXS/WAXS machine (Molecular Metrology Ltd.) coupled to a Rigaku MicroMax-007HF rotating anode generator. The 2D WAXS data were collected in vacuum using Fuji image plates with a pixel size of 100x100 μm^2. The modulus of the scattering vector **s** ($s=2\sin\theta/\lambda$, where θ is the Bragg angle) was calibrated using several diffraction orders of Ag

behenate. WAXS measurements were performed in transmission on oriented samples (fibers) prepared by extruding of the polymer complexes with a home-made mini-extruder.

Grazing Incidence X-ray Scattering (GIWAXS) experiments were conducted on the X6B beamline of the National Synchrotron Light Source at Brookhaven National Laboratory using a wavelength of 0.79Å. The samples were positioned in environmental chamber isolated with Kapton windows and equipped with a computer-controlled heating stage Instec HCS402 containing a cryo-unit. The focused beam of 0.25 mm vertical × 0.5 mm horizontal size was directed on the sample at an angle θ_{inc} of 0.2°. The diffraction pattern was collected using a CCD detector from Princeton Instruments having a 120 mm × 120 mm image area (2084 × 2084 pixels). The sample-to-detector distance, typically of 240 mm, was calibrated using Ag behenate powder.

Grazing Incidence Small-Angle X-ray Scattering (GISAXS) experiments were performed on the BM26 beamline of the E.S.R.F. (Grenoble, France). Diffraction patterns were collected with a MAR CCD image plate system. The wavelength of 1.24 Å and the sample-to-detector distance of 0.51 m define the accessible s-range from 0.015 to 0.370$Å^{-1}$. The films deposited on Si wafers were fixed on a special tilting stage, which allows rotation in and out of the incidence plane.

Scanning Force Microscope (SFM). The morphology of the polymer complex films was investigated under ambient conditions in Tapping Mode with a NanoScope IIIa instrument (Digital Instruments/ Veeco Metrology, Santa Barbara, CA). Commercially available standard silicon cantilevers (PPP-SEIH-W from Nanosensors) with a spring constant of 5-37 N/m and oscillation frequency of ~125 kHz were used. Both the topography and phase images were recorded; the micrographs were processed with Digital Instruments software, NanoScope, version 5.12r5. The phase images of polymer complex film at high temperature were acquired using a hot stage controlled by a MMHTRS High Temperature Heater Controller (Digital Instruments, Veeco Metrology, Santa Barbara, CA).

6.3. Results

6.3.1. FTIR analysis of the block copolymer complex

The spectroscopic investigation was undertaken to understand whether the hydrogen bonding between the pyridine group of the polymer backbone and carboxylic group of the ligand is strong enough to induce the complex formation. Previously, X. Zhu *et al.* studied the

complex formation of P2VP and (4′ - [3″,4″,5″ - tris(octyloxy)benzoyloxy]azobenzene-4-sulfonic acid).[25] However, in that particular case there was a strong ionic interaction between sulfonic acid and pyridine, whereas the strength of hydrogen bonding in the pyridine/carboxylic group pair, which is in the focus of the present study, is at least three times weaker.[31]

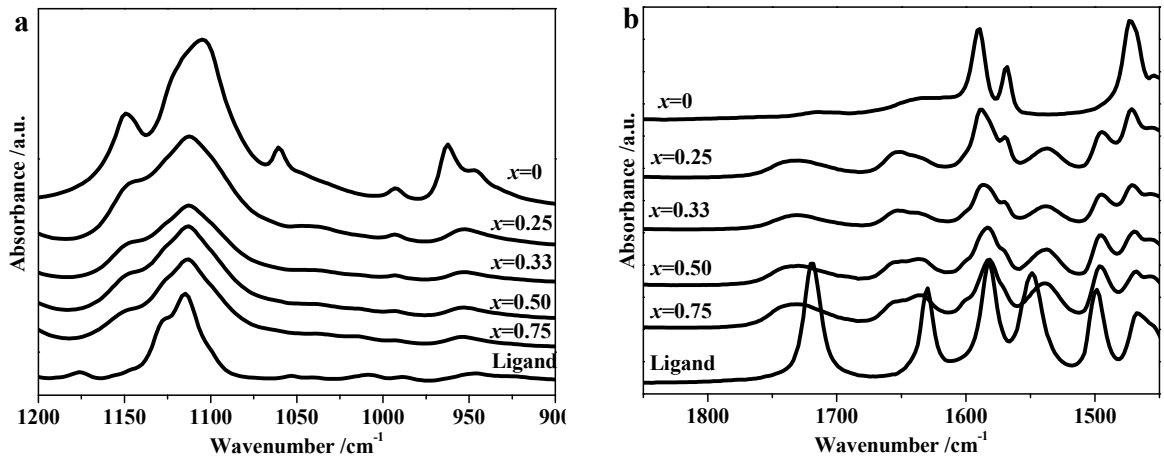

Figure 6.1. FTIR spectra of P2VP(**L**)$_x$-PEO: (a) 900-1200cm^{-1} region; (b) 1350-1450cm^{-1} region. The curve for x=0 corresponds to the pure copolymer.

When C8-Ala-COOH is mixed with P2VP-PEO, the ligand preferentially attaches to P2VP because of the acid/base interactions. However, PEO chain might also form hydrogen bonds between the ether groups of the backbone and carboxylic group of the mesogen. It is known that positions of the stretching modes of the pyridine ring at 1590, 993 and 625 cm^{-1} are altered when pyridine is involved in hydrogen bonds.[32] As can be seen from **Figure 6.1** which shows FTIR spectra of P2VP(**L**)$_x$-PEO, the bands at 993 and 1590 cm^{-1} are broadened and shifted to smaller wavenumbers with increasing x. Moreover, a new shoulder appears at about 1600 cm^{-1} for x equal 0.50 and 0.75. For ligand, the band at 1719 cm^{-1} corresponding to the stretching vibration of C=O of the carboxylic group broadens and shifts from 1719 cm^{-1} to 1730 cm^{-1} when the complex is formed (**Figure 6.1**b). These results suggest that a hydrogen bond interaction of the carboxylic group of **L** with the pyridine unit in P2VP takes place. However, a quantitative determination of the degree of complexation between the ligand and P2VP is difficult. Indeed, the presence of benzene ring in the ligand and its absorption band overlaps with those of pyridine, preventing to perform the analysis for example with the use of the method reported in ref. [33] Moreover, it was documented that if hydrogen bonding is not strong enough to drive all the ligand to bind to the block copolymer backbone, the degree of

complexation saturates at about 0.7-0.8.[20,33] Therefore one cannot exclude the presence of a small amount of free ligand in the complex. Since there is no evidence of the macrophase separation of the ligand, from which a band corresponding to that of the dimerization of the ligand is expected (1719 cm^{-1}), the free ligand is likely to be present in the molecular state. It is noteworthy that the characteristic band of the ether groups remains unaltered regardless of the degree of complexation.

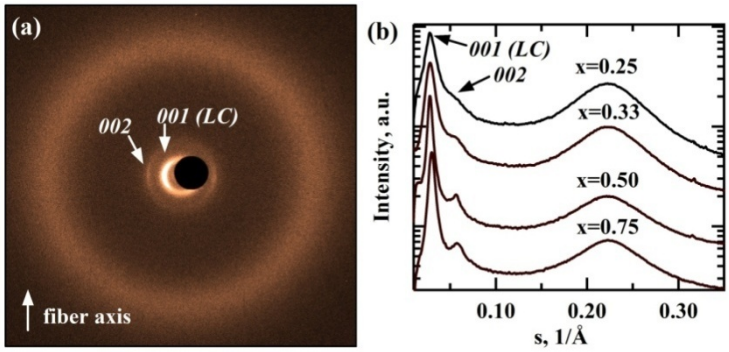

Figure 6.2. WAXS patterns of P2VP(**L**)$_x$ recorded at room temperature: (a) 2D pattern corresponding to x=0.50, (b) 1D-reduced WAXS curves of P2VP(**L**)$_x$ for x = 0.25, 0.33, 0.50 and 0.75.

6.3.2. Bulk structure

Mesomorphic structure of the homopolymer complex P2VP(L)$_x$. Depending on the sample thermal history, the C8-Ala-COOH compound in the pure state reveals two crystalline polymorphs, monoclinic and hexagonal. The details of the structural analysis of the pure ligand are given in the Supporting Information (cf. **Figures S6.1**, **S6.2** and **S6.3**). It should be emphasized that no liquid-crystalline state was detected for the ligand. The complexation with P2VP homopolymer changes the ligand structure. Thus, two orders of the fundamental WAXS peak of the complex are observed for all the compositions, thereby showing the formation of a smectic structure upon complexation (cf. **Table 6.1** and **Figure 6.2**). The smectic ordering is present up to x=0.75, which is at variance with what has been observed for a similar system previously.[25] Indeed, for such system one can expect formation of a columnar phase due to the space hindrance imposed on the ligand molecules disposed along the P2VP chain. The absence of a smectic-columnar phase transition supports the hypothesis that at high degrees of complexation the hydrogen bonding is not strong enough to drive all of the ligand to the P2VP backbone. As mentioned above, the free ligand molecules probably dissolve in the polymer matrix in the molecular state. In this context, it is worth mentioning

that extruded fibers of the complexes corresponding to high degrees of complexation show decreasing orientation, the fact that can be also accounted for by the free ligand molecules.

Table 6.1. Structural properties of the as-prepared fibers of P2VP(**L**)$_x$ and P2VP(**L**)$_x$-PEO.

Samples	x	WAXS of the LC phase			SAXS
		d_{001}, nm	Δ, nm^{-1}	d_{002}, nm	L, nm
P2VP(**L**)$_x$	0.2	3.66	0.088	1.81	-
	0.3	3.48	0.081	1.92	-
	0.5	3.37	0.046	1.71	-
	0.7	3.28	0.059	1.76	-
P2VP(**L**)$_x$-PEO	0	-	-		34
	0.2	3.64	0.098	1.81	36
	0.3	3.47	0.094	1.83	40
	0.5	3.20	0.084	1.68	37
	0.7	3.16	0.064	1.7	36

Δ –half width at half maximum (FWHM) of the 001 peak

Block copolymer complex PEO-P2VP(L)$_x$. The LC ordering such as described for the case of the P2VP(**L**)$_x$ is preserved in the P2VP(**L**)$_x$-PEO complexes: in the WAXS patterns, two peaks with d spacing ratio of 1:2 are observed. The position of the first peak is similar to that of the homopolymer (cf. **Table 6.1** and **Figure 6.3**). The presence of the WAXS peaks pertinent to the unit cell of PEO in the as-prepared fibers shows that in all the complexes the PEO bock is semicrystalline (see **Figure 6.3**). The crystal orientation can be analyzed from the positions on the 2D diffractograms of the characteristic peaks at 0.46 nm and 0.38~0.40 nm of the monoclinic lattice of PEO. These peaks correspond to 120 and $\bar{1}$32, 032, 112, $\bar{2}$12, $\bar{1}$24, $\bar{2}$04, 004 reflections, respectively.[2] For all degrees of complexation the maximum intensity of the 120 peak is on the equator of the diffractograms, which means that the PEO chains in the crystalline lamellae are preferentially oriented parallel to the drawing direction (**Figure 6.3**).

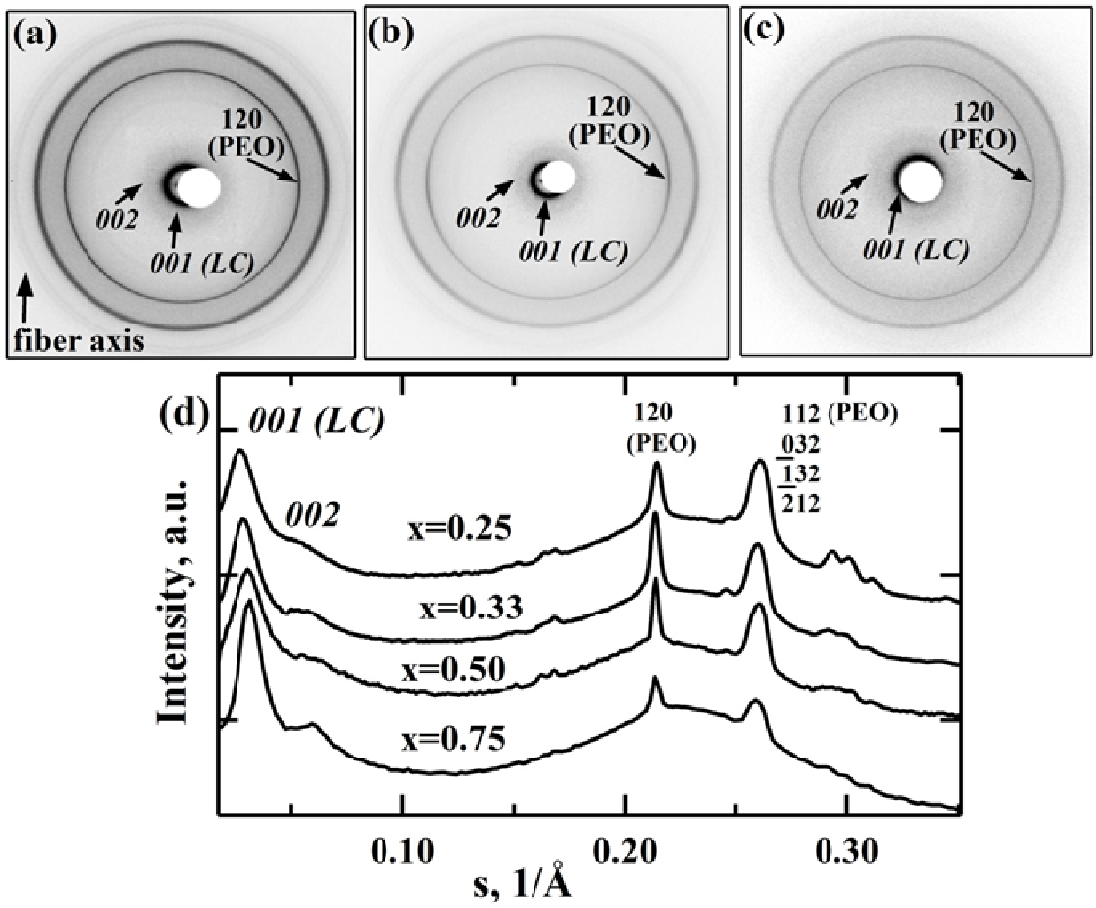

Figure 6.3. 2D WAXS patterns of the as-extruded P2VP(**L**)$_x$-PEO samples for x = 0.25 (a), 0.33 (b) and 0.50 (c). The corresponding 1D WAXS curves together with the curve for x = 0.75 are given in (d).

The SAXS technique was used to address the P2VP(**L**)$_x$-PEO supramolecular structure. In the pure block copolymer, only one broad SAXS peak at $s = 0.029\ nm^{-1}$ (d = 34nm) is observed (**Figure 6.4**). It is known that the P2VP and PEO blocks are miscible at room temperature. Using the analytical method described by Yeh et al. the "lower critical ordering transition" temperature (LCOT) of the studied copolymer was calculated to be 350°C.[26] Therefore, the observed SAXS peak can be ascribed to the electron density contrast between the amorphous regions and the PEO crystals. In the polymer complex, a SAXS peak at a similar position is observed. In order to prove the existence of a microphase separation in the block copolymer complex, SAXS experiments were performed at 100°C (i.e. above the melting temperature of PEO). In this case, a much sharper interference maximum with a slightly changed d-spacing was observed (cf. **Figure 6.4**), which allowed us to conclude that the SAXS intensity at room temperature originates at least in part from the microphase-separated domains. The characteristic distance between the domains, L, was calculated from the corresponding 1D SAXS curves (cf. **Figure 6.4** and **Table 6.1**).

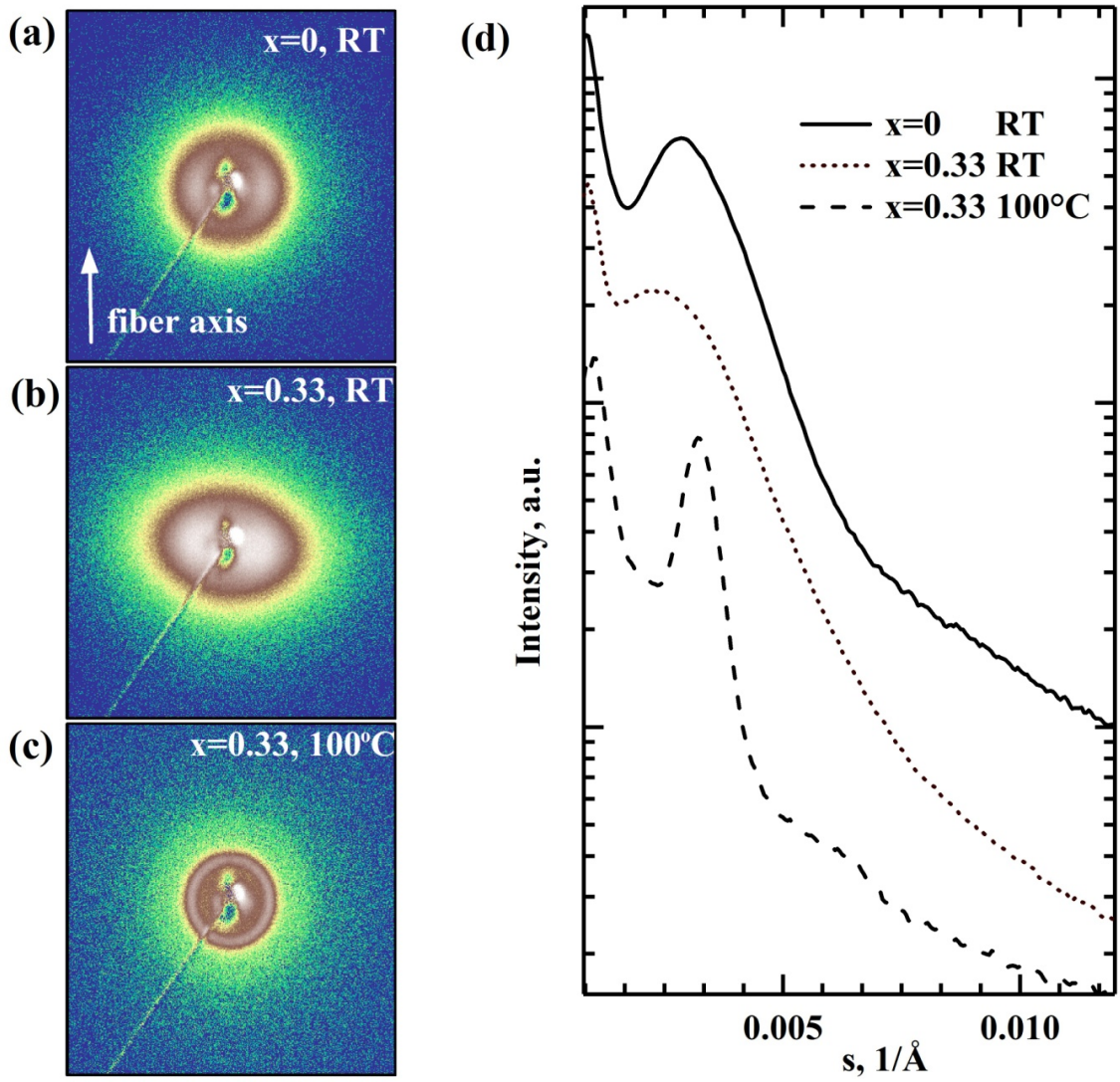

Figure 6.4. 2D SAXS patterns of the as-extruded P2VP(**L**)$_x$-PEO samples measured at room temperature for x = 0 (a), x = 0.33 (b) and at 100°C for x = 0.33 (c). The corresponding 1D SAXS curves are given in (d).

6.3.3. Crystallization and melting behavior of the block copolymer complexes

Figure 6.5 shows the DSC curves acquired during cooling and subsequent heating of P2VP(**L**)$_x$-PEO. The parameters evaluated from these curves are listed in **Table 6.2**. It can be seen that, although crystallization and melting of PEO is observed for all samples, the crystallization temperature region is different. Thus, the neat block copolymer (the weight fraction of PEO is 60%) does not exhibit a clear exothermic peak upon cooling, but it undergoes cold crystallization at -16.1°C during subsequent heating (**Figure 6.5**). Similar behavior has been previously observed for PEO-P2VP copolymer with various PEO weight fraction.[34]

Incorporating of 0.25 of **L** drastically changes the crystallization behavior of PEO. Although in this case the weight fraction of PEO decreases to 39%, the sample starts to exhibit on cooling a sharp crystallization peak at 20.5°C. When *x* increases to 0.33, the sample shows two crystallization peaks on cooling, one of which is relatively close to room temperature (13.6 °C) and the other one at -19.1 °C. Further increase of *x* to 0.50 and to 0.75 leads to disappearance of the room-temperature exothermic peak, while the low-temperature peak remains. A slight decrease of T_m from 59.3 to 57.0°C (**Figure 6.5**b) and that of crystallinity from 70% to 50% (**Table 6.2**) are observed when the degree of complexation increases from 0.25 to 0.75. It is noteworthy that in this temperature range the DSC curves do not reveal transitions of the liquid crystalline phase.

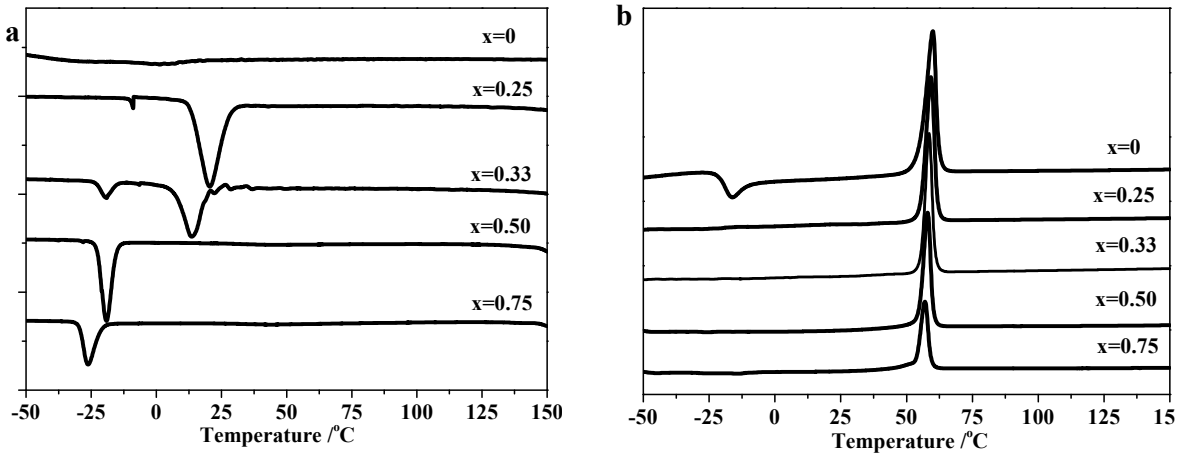

Figure 6.5. DSC curves of PEO-P2VP(**L**)$_x$ with different degree of complexation, *x*, measured during cooling (a) and subsequent heating (b) at 10 °C·min^{-1}.

Table 6.2. Thermodynamic parameters of P2VP(**L**)$_x$-PEO with different degree of complexation.

x	T_{mp}, ºC	T_{cp}, ºC	ΔT, ºC*	H, J·g^{-1}	Crystallinity, %
0	-16.1	60.0	76.1	71.5	58
0.25	20.5	59.3	38.8	54.7	69
0.33	13.6(-19.1)	58.6	45.0(77.7)	45.0	63
0.50	-23.5	58.0	81.5	33.4	57
0.75	-26.2	57.0	83.5	25.6	55

*Supercooling ΔT is defined as $\Delta T = T_{mp} - T_{cp}$

6.3.4. Thin film structure

The structure of thin films of P2VP(**L**)$_x$-PEO complexes was investigated using a combination of SFM, GIWAXS and GISAXS. **Figure 6.6-10** show SFM images and GISAXS/GIWAXS patterns for the films with different values of *x*. The micro-structural parameters are summarized in **Table 6.3**. In general, in the light Tapping mode conditions,[27] the SFM images are largely featureless (results not shown here). It can be supposed that the hydrophobic alkyl tails of the ligand preferentially adsorb on the film/air interface to reduce the surface energy. This results in a surface layer, which prevents observation of the film microstructure. Since the cantilever can penetrate this surface layer and resolve the microstructures under the hard Tapping mode conditions,[27] only the results of hard Tapping mode are reported here.

Pure P2VP-PEO. **Figure 6.6** represents the SFM and GIWAXS results obtained on pure P2VP-PEO block copolymer after thermal annealing. At room temperature, the film surface displays densely packed spherulite-like features. Importantly, above the melting point of PEO, SFM does not reveal any signs of the microphase separation, because, as it was mentioned, the temperature employed in the experiments is still far below the LCOT. The 2D GIWAXS pattern (cf. inset in **Figure 6.6**) displays reflections of the monoclinic unit cell of PEO crystals. The position of 120 peak indicates that the crystalline PEO chains are preferentially oriented perpendicular to the substrate.

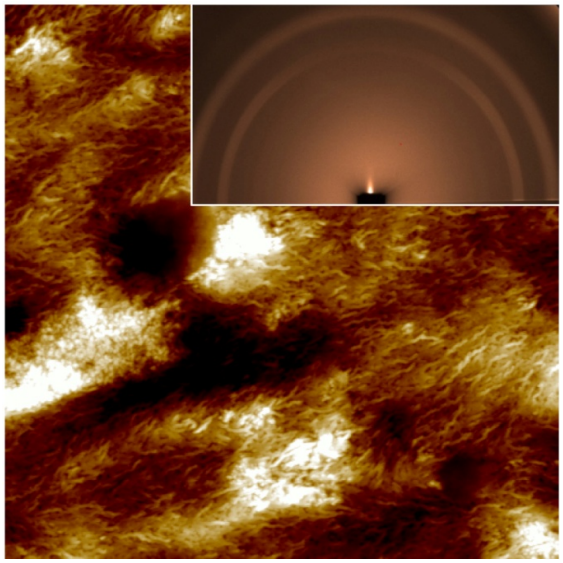

Figure 6.6. Room-temperature SFM height image and GIWAXS pattern (inset) measured on a film of pure P2VP-PEO. The scan size is 3x3μm^2.

P2VP(<u>L</u>)$_{0.25}$-PEO. At room temperature the contrast in the SFM phase images is rather low (results not shown), since both the semicrystalline PEO and liquid-crystalline P2VP(**<u>L</u>**)$_{0.25}$ domains are hard. Heating the films above the melting point of PEO makes it possible to discriminate the PEO-rich regions from the LC-complex regions. As illustrated in **Figure 6.7**a, at 65°C bright discontinuous dots/stripes having periodicity of 36±2nm together with featureless domains are observed. Based on the weight fraction of PEO (39%) one can assign these regions to the LC lamellae. At this temperature, all PEO crystals are molten, but the presence of the mesogen preserves the phase separation of PEO and LC blocks. Melting of PEO makes the PEO-rich regions to become softer than the LC phase and accounts for their darker contrast in the SFM phase images.

It is noteworthy that at some places the structure of microdomains looks discontinuous. In the GISAXS pattern the interference peak is positioned on the equator, which means that the block copolymer microdomains are oriented perpendicular to the substrate (**Figure 6.7**b). The GISAXS spacing equals ca. 35 nm, which is in good agreement with the SFM data (cf. **Table 6.3**). However, since only one peak is visible, it is impossible to identify the type of the micro-phase separated morphology.

Based on GIWAXS, both PEO crystals and LC phase are relatively well oriented (**Figure 6.7**c). The PEO chains have a texture similar to that of the pure P2VP-PEO films, but the crystalline stem orientation is noticeably better. Two meridional peaks of the LC phase with a *d*-spacings ratio of 1:2 are observed, allowing assigning it to a lamellar phase. The period of the LC lamellar phase is similar to the one measured on the bulk samples.

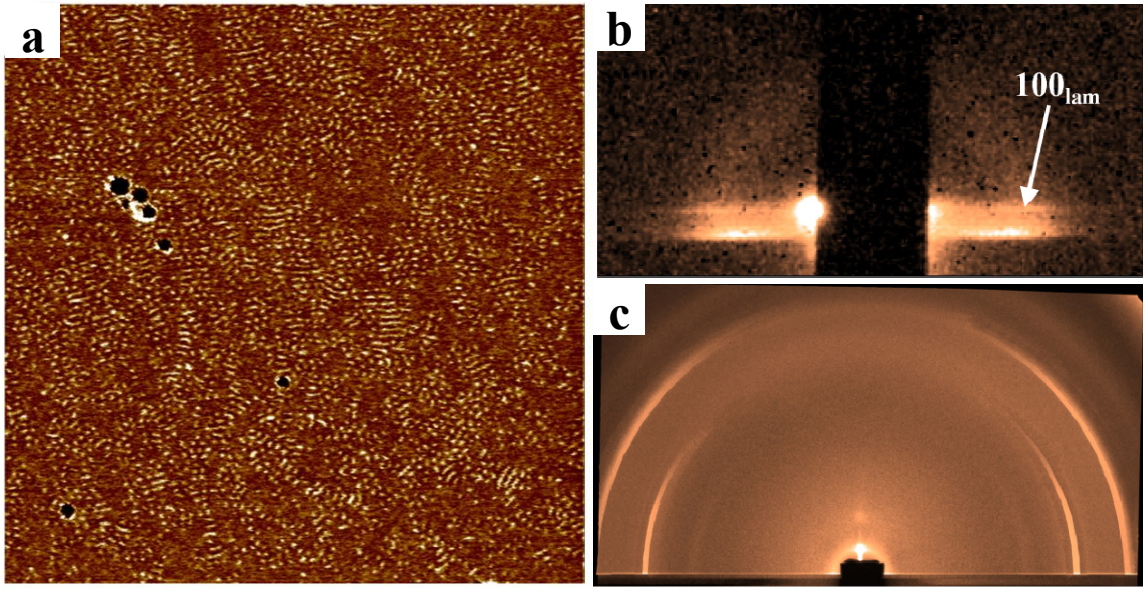

Figure 6.7. SFM phase image recorded at 65 °C (a), room-temperature GISAXS (b) and GIWAXS pattern (c) of P2VP(**L**)$_{0.25}$-PEO film. The scan size is 3x3μm^2

P2VP(L)$_{0.33}$-PEO. Similarly to the case of x =0.25, the phase contrast in SFM images (**Figure 6.8**) is enhanced by heating the sample above the melting point of PEO. The SFM images show a typical fingerprint morphology, indicating the presence of vertically-standing block copolymer lamellae with periodicity of 35±3nm (cf. **Figure 6.8**a and **Table 6.3**). However, the presence of a cylinder structure lying parallel to the substrate cannot be completely ruled out, as it would exhibit a very similar morphology. Indeed, the GISAXS data reveals a mixture of the block copolymer lamellae standing vertically and cylinders lying parallel to the surface. In this case, the equatorial GISAXS peak corresponds to the vertically oriented lamellar phase with a periodicity of 37 nm, and the non-equatorial reflection, indexed as 100 peak of a hexagonal phase, corresponds to cylinders lying parallel to the surface with a period of 34 nm (**Figure 6.8**b). Moreover, the LC ordering of the complex also exhibits both homeotropic and planar orientation, as can be seen from the equatorial and meridional position of the GIWAXS peaks at 3.5 nm and 1.8 nm (**Figure 6.8**c). In contrast, the PEO crystals reveal only one orientation with ***c*** axis directed along the film normal; the quality of the crystal orientation being improved as compared to that of x=0.25.

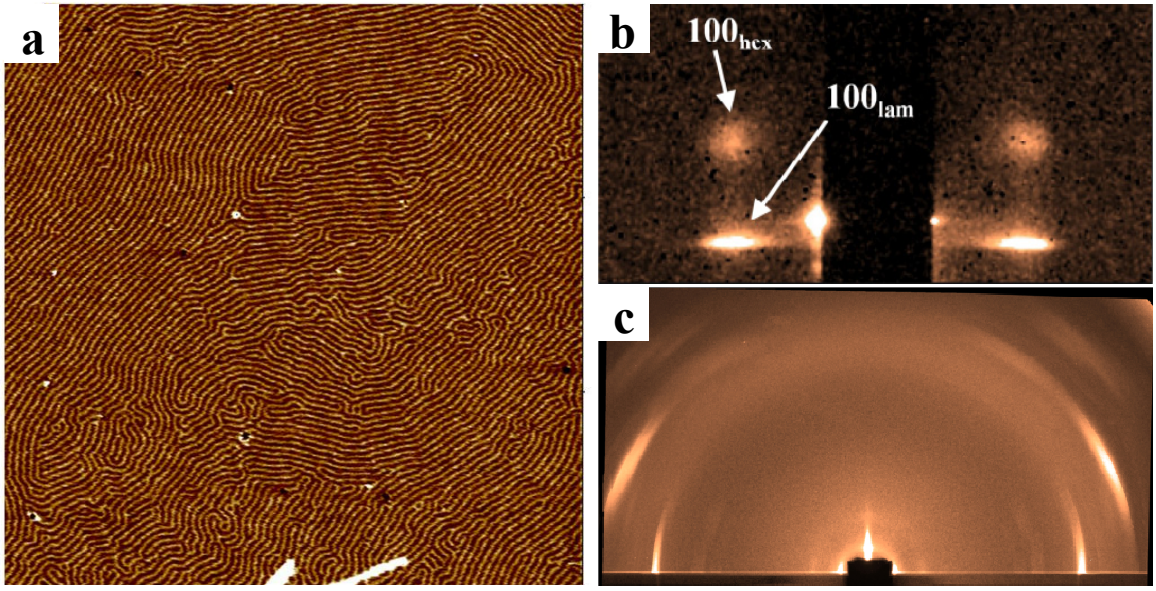

Figure 6.8. SFM phase images measured at 65 °C (a), room-temperature GISAXS (b) and GIWAXS (c) patterns of P2VP(**L**)$_{0.33}$-PEO film. The scan size is 3x3μm^2.

P2VP(L)$_{0.50}$-PEO. When the degree of complexation reaches 0.50, the weight fraction of PEO decreases further to 29% (cf. **Table 6.3**). Therefore, predominantly cylindrical morphology of the PEO block is expected. As shown in **Figure 6.9**a, the block copolymer cylinders with periodicity of 39±4 nm are well visible with SFM. The phase contrast in the images is already well pronounced at room temperature, which means that crystallinity of PEO block is low. This fact is supported by weaker diffraction from the PEO crystals in GIWAXS. The GISAXS pattern reveals only the first order of the equatorial peak, corresponding to the distance of 36 nm, which can be assigned to the 100 reflection of hexagonal phase with cylinders oriented homeotropically (**Figure 6.9**b). The orientation of the LC phase can be appreciated from the two orders of the fundamental meridional peak of the lamellar phase with a distance of 3.2 nm (cf. inset of **Figure 6.9**c). In this case, the smectic LC layers are parallel to the substrate. Also highly oriented peaks of the PEO crystals are observed in GIWAXS. The direction of the PEO stems is the same as for the lower *x* values, i.e. perpendicular to the substrate.

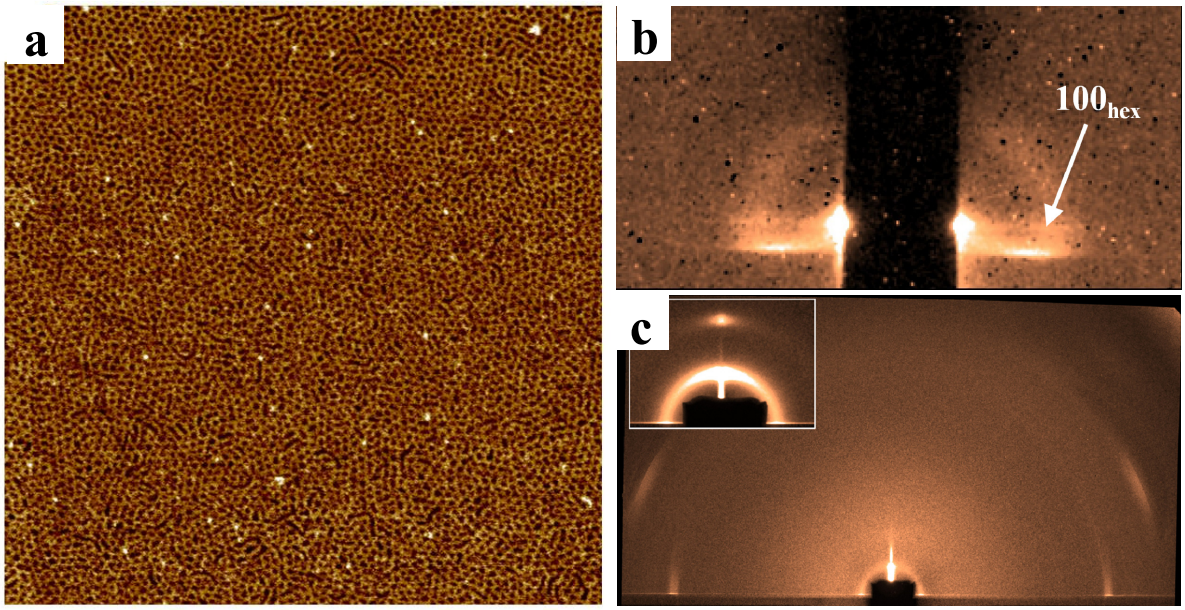

Figure 6.9. Room-temperature SFM phase image (a), GISAXS (b) and GIWAXS (c) patterns of P2VP(**L**)$_{0.50}$-PEO film. The scan size is 3x3μm^2.

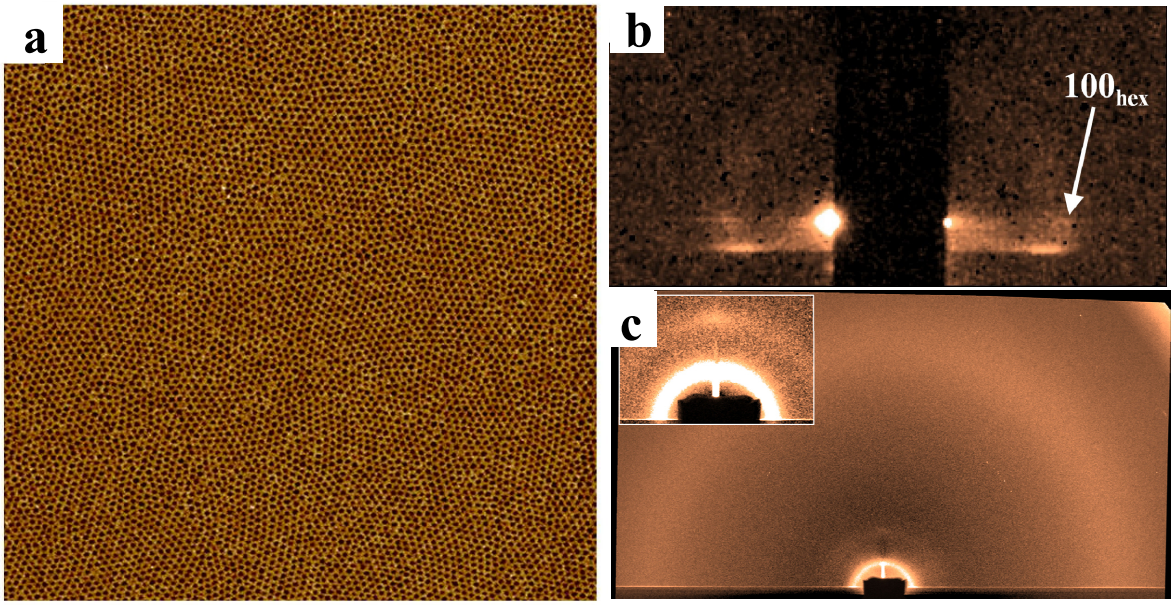

Figure 6.10. Room-temperature SFM phase image (a), GISAXS (b) and GIWAXS (c) patterns of P2VP(**L**)$_{0.75}$-PEO film. The scan size is 3x3μm^2.

P2VP(L)$_{0.75}$-PEO. At this composition, the weight fraction of the PEO is further decreased to 23%, SFM exhibits a regular structure of dark dots (**Figure 6.10**a). This morphology with periodicity of 35±3 nm can be assigned to PEO cylinders oriented perpendicular to the surface. The orientation of the copolymer is in agreement with the GISAXS pattern showing a

strong equatorial peak at 31 nm (**Figure 6.10**b). The absence of GIWAXS peaks prompts us concluding that crystallization is largely suppressed in the sample. By contrast, the morphology of the LC phase does not change as compared to x=0.50 (**Figure 6.10**c).

Table 6.3. Micro-structural parameters of PEO_{560}-$P2VP_{150}(\underline{L})_x$ films obtained from SFM and GISAXS

		SFM		GISAXS		
x	w_{LC}*, %	Periodicity d_{exp}, nm	Layer thickness/ cylinder diameter d_{PEO}, nm	Periodicity d_{exp}, nm	Lattice parameter L, nm	Type of morphology
0.25	61	36±3**	22±3	34±2	34 (lam)	Break-out crystallization from Sm-*in*-PEO Lam
0.33	65	36±2	22±3	29±2/ 37±2	33 (hex)/ 37 (cyl)	Sm-*in*-PEO Lam & Sm-*in*-PEO Cyl (there is also break-out crystallization here)
0.50	71	39±4	24±6	36±2	42 (cyl)	Crystalline PEO Cyl in Sm matrix
0.75	77	35±3	21±4	33±2	38 (cyl)	Amorphous PEO cylinders in Sm matrix

*Measured from SFM phase images after thermal annealing.
**Based on the power spectral density (PSD) function for SFM phase image recorded at 65°C.

6.4. Discussion.

6.4.1. Liquid-crystalline morphology

The phase behavior of a polymer complex depends on a subtle balance between the association interaction and polar-nonpolar repulsion in the ligand/polymer pair.[33,35,36] Obviously, the hydrogen bonds between the carboxylic groups and pyridine units are energetically more favorable than dimerization of the ligand as evidenced by the red shift of

the carbonyl absorption band in the FTIR spectra. The molecular shape of the ligand and phase separation between the P2VP backbone and hydrophobic alkyl tail promote formation of a smectic structure. Similar structure has been reported by Ikkala and coworkers for a simple surfactant (PDP)[15,35] and a cholesteric derivative.[33] In principle, one can imagine that the layer-like packing of the mesogens in the complex occurs either with or without interdigitation of the alkyl tails.[35] In the first case, a smectic layer with a period close to the length of a single mesogen molecule is formed[21] while the second case brings about a bilayer formation.[35] For the ligand under study, the high density of alkyls (three alkyl chains per ligand) makes the chain interdigitation unlikely, the fact which is supported by the WAXS results (cf. **Figure 6.2** and **Table 6.1**). Indeed, the smectic layer period is about 3.3-3.7 nm, which is close to the double of the molecular length of the ligand in the fully extended state (~1.7nm).

The degree of complexation has an influence on the LC ordering. At low degrees of complexation, the density of the mesogens along the backbone is low, which gives rise to a loosely packed smectic mesophase. Thus, at x=0.25, the FWHM of the LC phase fundamental peak equals 0.088nm^{-1} (**Table 6.1**), corresponding to a domain size of about 10 nm, or of approximately three smectic periods. The smectic order improves as more ligand is incorporated: for x = 0.5 the FWHM is reduced to 0.046 mm^{-1}. Interestingly, the d-spacing of the X-ray diffraction peak gradually decreases with increasing x, which probably means that higher degrees of complexation result in a more stretched conformation of the P2VP backbone, and, accordingly, in a smaller polymer chain cross-section. Simultaneously, the decrease of FWHM of the LC phase fundamental peak indicates improvement of long range ordering of the smectic phase (cf. **Table 6.1**). Noteworthy, the presence of PEO block does not change the type of mesophase.

6.4.2. Crystallization and orientation of PEO in thin films

As mentioned above, PEO and P2VP chains are miscible. It is reported that PEO cannot crystallize when the weight fraction of the corresponding block is less than 60%, due to the blocks miscibility.[34] Introduction of the ligand into the system generates the microphase separation and promotes the LC ordering. We believe that three different confinement regimes are observed in this work: soft confinement at low x ($\leq$0.25), co-existence of soft and hard confinements at intermediate x~0.33 and hard confinement at higher values of x ($\geq$0.5).

Low degrees of complexation. When the sample (at *x=0.25)* is cooled down from the annealing temperature, PEO crystallization occurs at about room temperature, i.e. under normal undercooling conditions (ΔT = 38.8 °C). This undercooling is similar to that of a PEO homopolymer with molecular weight of 30 kg·mol^{-1} (results not shown here). It is likely that at this composition the segregation strength of microphase separation is not sufficient to efficiently confine the crystallization, and therefore the microphase-separated block copolymer morphology is partially destroyed by the growing PEO crystals. Such crystallization behavior of PEO in the soft confinement is typical for the moderate strength of the microphase separation.[11] In thin films, the ligand organizes in a smectic phase parallel to the substrate, while the block copolymer lamellae have vertical orientation. The PEO crystallization proceeds with ***c***-axis oriented perpendicular to the substrate. The SFM phase images evidence the existence of microphase-separated regions disturbed by crystallization (cf. **Figure 6.7**a). The schematics of the hierarchical structure of the complex is given in **Scheme 6.2**.

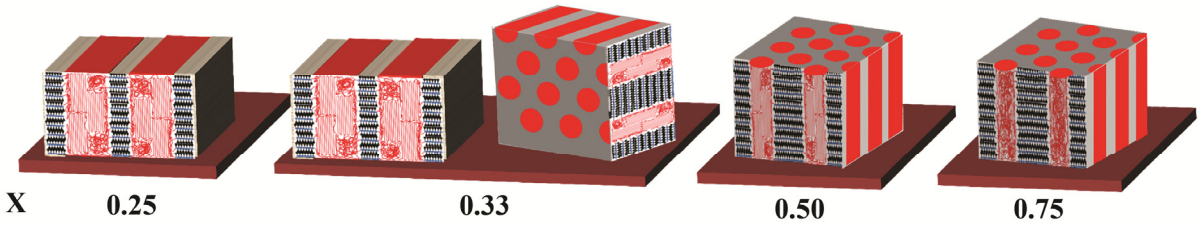

Scheme 6.2. Schematics of the crystal orientation and LC ordering in thin block copolymer films with different degrees of complexation (*x*).

Intermediate degrees of complexation. The increase of *x* to 0.33 results in improvement of the LC ordering. In the DSC curves, in additional to the crystallization peak at ΔT = 45.0 °C one observes another peak albeit small in the low-temperature region, at ΔT = 77.7 °C. This undercooling is very close to that of the PEO crystallization in 2D-confined cylinders (*e.g.*, PEO cylinders in PS matrix).[37] The co-existence of two types of morphologies, *i.e.* Lam/Cyl is supported by the GISAXS data. Moreover, the horizontal and vertical smectic layers of LC-phase observed in GIWAXS (cf. **Figure 6.8**c) can be pertinent to the vertically oriented copolymer lamellae and lying cylinders, respectively. In spite of the two morphologies, only one orientation of PEO crystals is observed for which the PEO stems are perpendicular to the film surface, as it is the case for the complex with *x*=0.25 having vertically standing copolymer lamellae. One could also expect to see another population of PEO crystals oriented parallel to the substrate, which are relevant to the structure of lying cylinders. However, no

such orientation is found. One possible reason can be that the fraction of cylinder domains is insufficient to be visible in the GIWAXS patterns. The structural model corresponding to the degree complexation of 0.33 is shown in **Scheme 6.2**.

High degrees of complexation. For $x \geq 0.5$, larger undercoolings ($\Delta T > 80°C$) are necessary for the PEO crystallization, suggesting the hard confinement conditions.[9] Already at $x = 0.50$, a hierarchical morphology of the 2D-confined PEO cylinders immersed in the smectic LC matrix is observed. Narrow azimuthal width of the GIWAXS peaks, which testifies high crystal orientation (**Figure 6.9**c) together with less crystalline PEO in comparison with complexes at lower *x*-values, confirms that crystallization is fully confined. Since the PEO crystalline lamella thickness is close to the diameter of the PEO domains (**Table 6.3**), the preferential crystal growth direction is along the cylinder axis. The schematic model of the cross section of the thin film is given in **Scheme 6.2**.

If even more ligand is added (x=0.75), the PEO crystallization in thin films becomes largely suppressed. A hierarchical morphology (PEO cylinders in LC matrix) similar to that of x=0.50 is observed, with the exception that in this case PEO remains amorphous. A possible explanation of this fact is the reduction of the PEO cylinder diameter (cf. **Table 6.3**). This effect is also confirmed by DSC showing large undercooling typical of homogeneously nucleated PEO (**Table 6.2**). **Scheme 6.2** shows the structural model for this composition.

To explain the inability of PEO to crystallize one could evoke the possibility of the free ligand to form a complex with oxygen of the PEO ether group thereby perturbing the PEO chain conformation. However, this possibility can be ruled out, since no evidence of hydrogen bonding between the ligand and ether[38] is detected in the FTIR spectra (**Figure 6.1**).

6.5. Conclusions

This work describes formation of a complex between a novel wedge-shaped molecule, 4′-(3′′,4′′,5′′-tris(octyloxy) benzamido) propanoic acid and a PEO-P2VP block copolymer. Despite the absence of LC-phase for the pure ligand, the complex with P2VP homopolymer or with PEO-P2VP diblock copolymer exhibit a smectic phase, the ordering degree of which depends on the ligand content. For the block copolymer, the ligand induces a microphase separation between the blocks controlled by the degree of complexation. A transition from the disrupted BCP lamellae through coexistence of lamellae/cylinders to cylinders is consistently observed.

It is found that the LC ordering can confine the PEO crystallization. Different confinement environments can be generated as a function of the degree of complexation, *x*. At low values of *x* (e.g., *x*=0.25), the lamellar block copolymer morphology and insufficient segregation strength result in soft confinement for the PEO crystallization, which occurs at normal undercooling. Increasing the *x*-value leads to more enhanced LC ordering. This provides hard confinement for crystallization, similar to the glassy polymer matrices. Thus at *x*=0.33, two nanoconfinement environments co-exist such as the PEO lamellae and PEO cylinders in the LC matrix. Accordingly, two undercooling conditions are observed for the PEO crystallization: the "normal" undercooling values for the PEO lamellae (1D) and larger values for the PEO cylinders (2D). The pure 2D confinement is observed when the degree of complexation is further increased to 0.5. In this case, large undercooling is required for the PEO crystal nucleation since it occurs homogeneously, within isolated cylindrical domains. At the same time, this confinement decreases the maximum degree of crystallinity attainable in thin films, while crystallization becomes fully depressed at *x*=0.75.

During crystallization in the cylindrical phase at room temperature only the PEO crystals with the stems parallel to the cylinder axis survive as the pore diameter imposes a strong geometrical constraint on the growing crystals.

6.6. Supporting information

***Phase behaviors of the wedge-shaped ligand* L**

DSC. Ligand melts at ca. 114 °C and recrystallizes around 69 °C with transition enthalpies of 54 and 47 $J \cdot g^{-1}$, respectively. When the sample is quenched from the isotropic state to room temperature and heated back, the melting peak is shifted to 105 °C.

X-ray fiber diffraction. The sample shows two distinctly different X-ray patterns suggesting two crystalline polymorphs. The occurrence of each of the polymorphs depends on the sample thermal history (**Figure S6.1**). Both X-ray patterns demonstrate that the ligand **L** can be well oriented.

The as-extruded fiber (**Figure S6.1**a) shows three equatorial reflections at low angles positioned at 3.3, 1.9 and 1.65nm. The corresponding *d*-spacings have the ratio of $1:\sqrt{3}:\sqrt{4}$. This allows to assign the ligand structure to a hexagonal phase with the following lattice parameters: **a** = **b** = 3.80 nm, **c** = 0.81 nm, $\gamma = 120°$. The details of the peak indexation are given in **Table S6.1**.

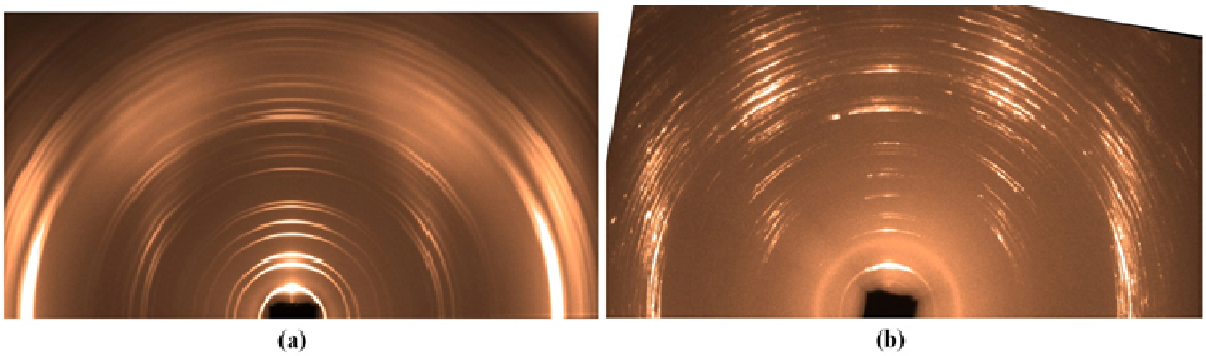

Figure S6.1. WAXS pattern of a ligand fiber annealed at 100°C for 24h (a) and quenched to room temperature from the melt (b). Fiber axis is horizontal.

Figure S6.1b displays the diffraction pattern recorded upon annealing the fiber close to the melting temperature and subsequent quenching to ambient temperature. The analysis of reflections allows to identify the structure as a monoclinic phase, having the lattice parameters **a** = 4.98 nm, **b** = 4.83 nm, **c** = 0.99 nm, $\gamma = 107°$. The peak positions and Miller indices are reported in **Table S6.1**. Both crystalline phases are stable, however melting of the monoclinic phase occurs before that of the hexagonal phase. This suggests that the crystallization into the monoclinic phase is favored upon quenching from the melt. However, we found that upon a long-time annealing, the monoclinic phase transforms in the hexagonal one.

SFM. SFM investigation of morphology of thin films cast on silicon wafers shows that **L** self-assembles in two distinct structures: an in-plane featureless layer-like structure (cf. the boxed region in **Figure S6.2**a) and a strip-like structure (arrowed in **Figure S6.2**a; **Figure S6.2**b). The height distribution computed from the layer-like structure displays a step-height of 2.5nm (cf. **Figure S6.2**a), which is very close to the half of *a*-parameter of the monoclinic phase (**Figure S6.1**b). High-resolution SFM images show that the strip-like structure has an in-plane periodicity of 3.9nm (**Figure S6.2**b). This morphology is typical of a columnar phase lying parallel to the substrate.[28] The data is consistent with hexagonal phase revealed with the fiber X-ray diffraction (**Figure S6.1**a). The GIWAXS results prove the coexistence of the monoclinic phase and hexagonal phases in the as-cast films (**Figure S6.2**c), which agrees with the two morphological features observed by SFM in the as-cast films.

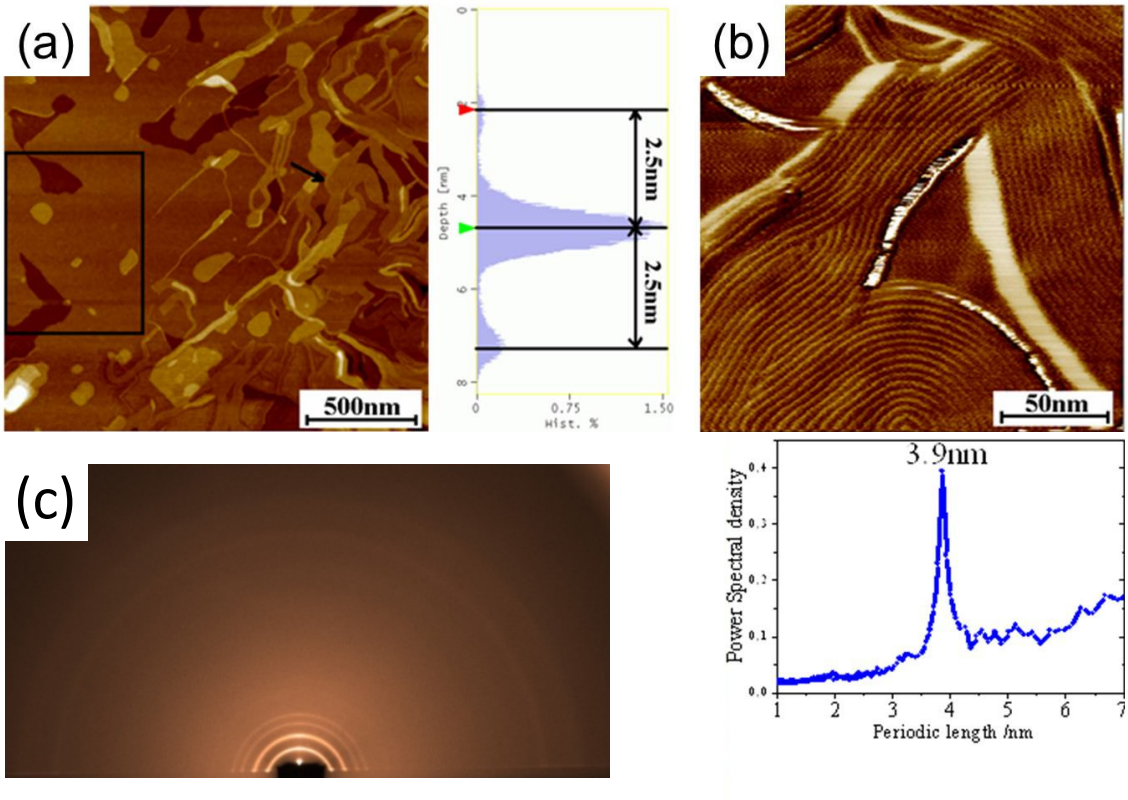

Figure S6.2. (a) Topography image and the height distribution computed from the boxed region; (b) high resolution phase image of the area indicated with black arrow together with the power spectral density function; (c) 2D GIWAXS pattern of the as-cast film.

Table S6.1. X-ray Fiber Diffraction Data Corresponding to the Crystalline Phases of the Ligand.

Hexagonal Phase					Monoclinic Phase				
h	k	l	d_{exp}, Å	d_{calc}, Å	h	k	l	d_{exp}, Å	d_{calc}, Å
1	0	0	33.20	33.09	2	0	0	23.86	23.80
1	1	0	19.05	19.10	0	2	0	23.14	23.08
2	0	0	16.50	16.54	1	3	0	13.53	13.53
2	1	0	12.47	12.51	4	0	0	11.85	11.90
3	0	0	11.00	11.03	0	4	0	11.46	11.54
2	2	0	9.53	9.55	-1	5	0	9.62	9.60
3	1	0	9.16	9.18	5	0	0	9.47	9.52
3	2	0	7.57	7.59	4	3	0	8.35	8.31
4	1	0	7.20	7.22	3	4	0	8.20	8.26
5	0	0	6.60	6.62	6	0	0	7.90	7.93
3	3	0	6.35	6.37	3	5	0	7.13	7.13
4	2	0	6.24	6.25	6	2	0	6.94	6.91
5	1	0	5.92	5.94	2	6	0	6.75	6.77
6	0	0	5.50	5.51	8	0	0	5.93	5.95
4	3	0	5.42	5.44	8	1	0	5.70	5.70
5	2	0	5.28	5.30	7	3	0	5.64	5.64
6	1	0	5.03	5.05	3	7	0	5.58	5.54
4	4	0	4.76	4.78	8	2	0	5.41	5.39
7	0	0	4.71	4.73	3	0	1	8.34	8.38
6	2	0	4.58	4.59	2	2	1	8.23	8.17
7	1	0	4.36	4.38	3	-3	1	7.83	7.89
5	4	0	4.22	4.24	4	0	1	7.55	7.60
6	3	0	4.15	4.17	2	3	1	7.42	7.49
8	0	0	4.13	4.14	1	4	1	7.10	7.20
7	2	0	4.03	4.04	4	3	1	6.40	6.36
8	1	0	3.86	3.87	6	-3	1	6.26	6.25
5	5	0	3.80	3.82	4	4	1	5.91	5.86
7	3	0	3.71	3.72	0	7	1	5.45	5.48
1	0	1	7.83	7.83	6	3	1	5.35	5.33
1	1	1	7.43	7.42	3	6	1	5.28	5.28
2	0	1	7.25	7.24	0	0	2	4.96	4.93
2	1	1	6.78	6.77	1	1	2	4.88	4.87
3	0	1	6.51	6.51	0	2	2	4.83	4.83
2	2	1	6.17	6.16	1	2	2	4.77	4.77
3	1	1	6.08	6.05	-3	1	2	4.75	4.73
4	0	1	5.75	5.77	2	2	2	4.68	4.67
3	2	1	5.52	5.52	3	1	2	4.64	4.65
4	1	1	5.37	5.38	4	-1	2	4.59	4.59
3	3	1	5.01	5.00	3	2	2	4.54	4.54
6	0	1	4.52	4.55	1	4	2	4.47	4.47
6	1	1	4.27	4.28	0	0	3	3.31	3.29
4	4	1	4.11	4.11	1	0	3	3.26	3.28
6	2	1	3.96	3.99	4	3	3	3.06	3.06
7	1	1	3.86	3.85	0	6	3	3.02	3.02

5	4	1	3.72	3.75	8	-1	3	2.90	2.90
7	2	1	3.58	3.61	3	7	3	2.83	2.83
8	1	1	3.45	3.49	1	9	3	2.73	2.74
7	3	1	3.37	3.38	10	2	3	2.63	2.64
0	0	3	2.66	2.69	4	9	3	2.60	2.61
0	0	4	2.01	2.01	3	10	3	2.57	2.57
					0	0	4	2.48	2.47
					0	5	4	2.38	2.38
					3	4	4	2.36	2.36
					7	0	4	2.32	2.32
					0	7	4	2.31	2.31
					0	8	4	2.27	2.27
					1	8	4	2.25	2.25
					0	9	4	2.22	2.22
					0	10	4	2.17	2.18
					0	11	4	2.12	2.13
					13	0	4	2.05	2.05
					1	13	4	2.01	2.01
					0	0	5	1.98	1.97
					1	4	5	1.94	1.94
					8	0	5	1.87	1.87
					12	0	5	1.77	1.77
					0	14	5	1.69	1.69
					0	17	5	1.60	1.60

6.7. References

(1) Kim, H.-C.; Park, S.-M.; Hinsberg, W. D. *Chemical reviews* **2010**, *110*, 146–77.

(2) Zhu, L.; Cheng, S. Z. D.; Calhoun, B. H.; Ge, Q.; Quirk, R. P.; Thomas, E. L.; Hsiao, B. S.; Yeh, F.; Lotz, B. *Journal of the American Chemical Society* **2000**, *122*, 5957–5967.

(3) Huang, P.; Zhu, L.; Guo, Y.; Ge, Q.; Jing, A. J.; Chen, W. Y.; Quirk, R. P.; Cheng, S. Z. D.; Thomas, E. L.; Lotz, B.; Hsiao, B. S.; Avila-Orta, C. a.; Sics, I. *Macromolecules* **2004**, *37*, 3689–3698.

(4) Zhu, L.; Mimnaugh, B. R.; Ge, Q.; Quirk, R. P.; Cheng, S. Z. D.; Thomas, E. L.; Lotz, B.; Hsiao, B. S.; Yeh, F.; Liu, L. *Polymer* **2001**, *42*, 9121–9131.

(5) Sun, Y.-S.; Chung, T.-M.; Li, Y.-J.; Ho, R.-M.; Ko, B.-T.; Jeng, U.-S.; Lotz, B. *Macromolecules* **2006**, *39*, 5782–5788.

(6) Chung, T.-M.; Wang, T.-C.; Ho, R.-M.; Sun, Y.-S.; Ko, B.-T. *Macromolecules* **2010**, *43*, 6237–6240.

(7) Huang, P.; Guo, Y.; Quirk, R. P.; Ruan, J.; Lotz, B.; Thomas, E. L.; Hsiao, B. S.; Avila-Orta, C. a.; Sics, I.; Cheng, S. Z. D. *Polymer* **2006**, *47*, 5457–5466.

(8) Chen, H.; Wu, J.; Lin, T.; Lin, J. S. **2001**, 6936–6944.

(9) Zhou, Y.; Ahn, S.; Lakhman, R. K.; Gopinadhan, M.; Osuji, C. O.; Kasi, R. M. *Macromolecules* **2011**, *44*, 3924–3934.

(10) Nandan, B.; Hsu, J.; Chen, H. Journal of Macromolecular Science, Part C: Polymer Reviews **2006**, 46, 143–172.

(11) Xu, J.-T.; Fairclough, J. P. a.; Mai, S.-M.; Ryan, A. J.; Chaibundit, C. *Macromolecules* **2002**, *35*, 6937–6945.

(12) van Zoelen, W.; Asumaa, T.; Ruokolainen, J.; Ikkala, O.; Ten Brinke, G. *Macromolecules* **2008**, *41*, 3199–3208.

(13) van Zoelen, W.; Polushkin, E.; ten Brinke, G. *Macromolecules* **2008**, *41*, 8807–8814.

(14) Tenneti, K. K.; Chen, X.; Li, C. Y.; Shen, Z.; Wan, X.; Fan, X.; Zhou, Q.-F.; Rong, L.; Hsiao, B. S. *Macromolecules* **2009**, *42*, 3510–3517.

(15) Ruokolainen, J.; Makinen, R.; Torkkeli, M.; Makela, T.; Serimaa, R.; Ten Brinke, G.; Ikkala, O. *Science* **1998**, *280*, 557–560.

(16) Ikkala, O.; Brinke, G. ten; ten Brinke, G. *Science* **2002**, *295*, 2407–9.

(17) Valkama, S.; Ruotsalainen, T.; Nykänen, A.; Laiho, A.; Kosonen, H.; ten Brinke, G.; Ikkala, O.; Ruokolainen, J. *Macromolecules* **2006**, *39*, 9327–9336.

(18) Chao, C.; Li, X.; Ober, C. *Pure and applied chemistry* **2004**, *76*, 1337–1343.

(19) Chen, H.-L.; Lu, J.-S.; Yu, C.-H.; Yeh, C.-L.; Jeng, U.-S.; Chen, W.-C. *Macromolecules* **2007**, *40*, 3271–3276.

(20) Chuang, W.-T. W.; Sheu, H. H.-S.; Jeng, U.-S.; Wu, H.-H.; Hong, P.-D.; Lee, J.-J. *Chemistry of Materials* **2009**, *21*, 975–978.

(21) Gopinadhan, M.; Beach, E. S.; Anastas, P. T.; Osuji, C. O. *Macromolecules* **2010**, *43*, 6646–6654.

(22) Zhu, X.; Beginn, U.; Möller, M.; Gearba, R. I.; Anokhin, D. V.; Ivanov, D. A. *Journal of the American Chemical Society* **2006**, *128*, 16928–37.

(23) Ikkala, O.; Ruokolainen, J.; ten Brinke, G.; Torkkeli, M.; Serimaa, R. *Macromolecules* **1995**, *28*, 7088–7094.

(24) Zhu, X.; Tartsch, B.; Beginn, U.; Möller, M. *Chemistry - A European Journal* **2004**, *10*, 3871–8.

(25) Zhu, X.; Beginn, U.; Möller, M.; Gearba, R. I.; Anokhin, D. V. D. V.; Ivanov, D. A. *Journal of the American Chemical Society* **2006**, *128*, 16928–37.

(26) Yeh, C.-L.; Hou, T.; Chen, H.-L.; Yeh, L.-Y.; Chiu, F.-C.; Müller, A. J.; Hadjichristidis, N. *Macromolecules* **2011**, *44*, 440–443.

(27) Albrecht, K.; Mourran, A.; Zhu, X.; Markkula, T.; Groll, J.; Beginn, U.; de Jeu, W. H.; Moeller, M. *Macromolecules* **2008**, *41*, 1728–1738.

(28) Anokhin, D. V.; Lejnieks, J.; Mourran, A.; Zhu, X.; Keul, H.; Möller, M.; Konovalov, O.; Erina, N.; Ivanov, D. A. *Chemphyschem : A European journal of chemical physics and physical chemistry* **2012**, *13*, 1470–8.

(29) Staunton, E.; Andreev, Y. G.; Bruce, P. G. *Faraday Discussions* **2007**, *134*, 143.

(30) Martuscelli, E.; Silvestre, C.; Addonizio, M. L.; Amelino, L. *Die Makromolekulare Chemie* **1986**, *187*, 1557–1571.

(31) Arnett, E. M.; Ahsan, T.; Amarnath, K. *Journal of the American Chemical Society* **1991**, *113*, 6858–6861.

(32) Lee, J. Y.; Painter, P. C.; Coleman, M. M. *Macromolecules* **1988**, *21*, 954–960.

(33) Korhonen, J. T.; Verho, T.; Rannou, P.; Ikkala, O. *Macromolecules* **2010**, *43*, 1507–1514.

(34) Córdova, M.; Lorenzo, A. T.; Müller, A. J.; Fragouli, P.; Iatrou, H.; Hadjichristidis, N. *Macromolecular Symposia* **2010**, *287*, 101–106.

(35) Luyten, M. C.; Alberda van Ekenstein, G. O. R.; Ten Brinke, G.; Ruokolainen, J.; Ikkala, O.; Torkkeli, M.; Serimaa, R. *Macromolecules* **1999**, *32*, 4404–4410.

(36) Osuji, C. O.; Chao, C.-Y.; Ober, C. K.; Thomas, E. L. *Macromolecules* **2006**, *39*, 3114–3117.

(37) Huang, P.; Zhu, L.; Cheng, S. Z. D.; Ge, Q.; Quirk, R. P.; Thomas, E. L.; Lotz, B.; Hsiao, B. S.; Liu, L.; Yeh, F. *Macromolecules* **2001**, *34*, 6649–6657.

(38) Lee, J. W.; Lee, C.; Choi, S. Y.; Kim, S. H. *Macromolecules* **2010**, *43*, 442–447.

SUMMARY

Controlling the micro-structure of organic materials is crucial for a variety of practical applications such as photonics, biomedicine or the rapidly growing field of organic electronics. Recent studies have shown a possibility of tailoring the polymer structure on the nanoscale using supramolecular self-assembly under spatial confinement. Despite extensive studies already performed in this field, many questions remain open. In particular, it will be important to understand how different structure formation processes such as crystallization, LC-phase formation, microphase separation, and others occur under confinement.

In the present work, we address the effect of 1D- and 2D-confinement on the structure formation for a variety of systems including segmented poly(ether-ester-amide) (PEEA) copolymers, main-chain liquid-crystalline (LC) polymers belonging to the family of poly(di-*n*-alkylsiloxane)s and liquid-crystalline/semicrystalline block copolymers formed through complexation of poly (2-vinylpyridine-b-ethylene oxide) (P2VP-PEO) with a wedge-shaped ligand, 4′-(3′′,4′′,5′′-tris(octyloxy) benzamido) propanoic acid.

In order to reveal the morphological diversity of the studied systems under confinement, the work was carried out on bulk materials and on thin films employing a battery of experimental methods. The main experimental techniques operational in direct and reciprocal space applied in my work are described in **chapter 2**.

In **chapter 3**, the 1D-confined crystallization process of the hard segments covalently bonded to the soft PTHF block was studied for segmented poly(ether-ester-amide)s. The PEEAs comprising glycine or β-alanine bisoxalamide units are highly phase-separated materials with fibril-like nano-crystals dispersed in the amorphous soft block matrix. The crystals have monodisperse thickness, which is close to the contour length of the hard segment. This is reflected in the fact that crystal thickness is independent from the sample thermal history. Therefore, one can conclude that the semicrystalline morphology of PEEAs is encoded in the primary chemical structure.

Upon deformation the soft block starts to crystallize resulting in formation of two types of crystalline domains. The structure formation in PEEAs was addressed during simultaneous time-resolved X-ray scattering and mechanical stretching experiments **in chapter 4**. Two main morphologies were revealed: at low strains the hard segments in fibril-like crystals become oriented perpendicular to the flow direction due to the high aspect ratio of the crystals, whereas at higher strains the crystal fragmentation sets in resulting in a change of the preferential crystalline stems direction to the one parallel to the drawing direction. The

difference in the thermal and mechanical properties of different PEEAs can be related to crystalline packing of their hard segments.

Chapter 5 deals with the spatial confinement of the polymers obtained either by impregnation of materials in porous nano-templates or by depositing thin polymer layers on specially prepared nanostructured substrates. In the case of poly(di-*n*-alkylsiloxane)s exhibiting both LC- and crystalline phases, we show that one CH_2 group can switch the in-plane orientation of the backbone polymer chains by 90 degrees, which is explained in terms of molecular- or grapho-epitaxy on the PTFE substrate. Also grapho-epitaxy takes place in the templates with 35 nm pore size where the mesomorphic lamellae grow exclusively parallel to the pore axis.

A possibility to create various microdomain morphologies, where the confined crystallization occurs was shown for diblock copolymer complex in **chapter 6**. The introduction of a ligand induces a microphase separation in P2VP-PEO copolymer by selective complexation with pyridine moiety. A transition from disrupted lamellae through coexistence of lamellae/cylinders to cylinders as a function of complexation degree is observed. By combining GIWAXS/GISAXS and SFM techniques the hierarchical multi-scale morphology of LC/semicrystalline block copolymer films was explored. Both the LC ordering (3-4 nm) and PEO crystallization (*ca.* 0.1-1 nm) simultaneously occur in block copolymer microdomains having the typical size of 30-40 nm. It is found that the LC ordering can efficiently confine the PEO crystallization. Increasing the amount of ligand leads to better LC ordering.

RÉSUMÉ

Le contrôle de la microstructure des matériaux organiques est crucial pour des applications pratiques telles que la photonique, la biomédecine ou encore le domaine très dynamique de l'électronique organique. Les études récentes ont montré une possibilité de contrôler la structure des polymères à l'échelle nanométrique en utilisant l'auto-assemblage supramoléculaire sous confinement spatial. Bien que de nombreuses études ont déjà été effectuées dans ce domaine, plusieurs questions essentielles restent ouvertes. En particulier, il est important de comprendre comment les différents processus de formation structurale tels que la cristallisation, la formation d`une phase cristal liquide et la séparation de phases se déroulent sous confinement.

Dans le présent travail, nous abordons l'effet du confinement à 1D et à 2D sur la formation de la structure pour une variété de systèmes, y compris les copolymères segmentés de poly(éther-ester-amide) (PEEA), les polymères cristaux liquides (CL) dont la chaîne principale appartient à la famille des poly(di-*n*-alkylsiloxane)s et des copolymères à bloc cristaux-liquides /semicristallins formés par complexation de poly(2-vinylpyridine-*b*-oxyde d'éthylène) (P2VP-PEO) avec un ligand cunéiforme, l`acide 4′-(3′′,4′′,5′′-tris(octyloxy) benzamido) propanoïque.

Pour être capable de traiter de façon adéquate la morphologie complexe de ces systèmes sous confinement, le travail a été effectué en utilisant une batterie de méthodes expérimentales. Les techniques principales opérationnelles dans l'espace direct et réciproque que nous avons employées sont décrites dans le **chapitre 2**.

Dans le **chapitre 3**, le processus de cristallisation des blocs rigides liés de façon covalente avec des chaînes flexibles a été étudié pour des poly(éther-ester-amide)s (PEEA) segmentés. Les PEEAs comprenant des groupements bisoxalamides de glycine ou de β-alanine sont les matériaux hétérogènes composés de nano-cristaux fibrillaires (confinement à 1D) dispersés dans la matrice formée par le bloc flexible amorphe. Nous avons trouvé que tous les cristaux sont caractérisés par une épaisseur monodisperse qui est proche de la longueur du contour du segment rigide. Ceci explique que l'épaisseur cristalline soit complètement indépendante de l'histoire thermique de l'échantillon. Par conséquent, on peut conclure que la morphologie semicristalline de PEEA est largement encodée dans sa structure chimique primaire.

Lors d`une expérience de traction des PEEAs, le bloc mou commence à cristalliser, ce qui donne lieu au deuxième type de cristaux présents dans le système. Les détails de la cristallisation des PEEAs sont discutés dans le **chapitre 4**. Les études structurales de ces

systèmes ont été réalisées par la diffusion des rayons-X résolue en temps et en température combinée avec des essais mécaniques simultanés. Deux morphologies distinctes ont été identifiées au cours de l'étirement: à taux de déformation faible, les segments rigides s'orientent perpendiculairement à la direction d'étirement. Par contre, pour les déformations élevées la fragmentation des cristaux se produit de plus en plus, ce qui induit une réorientation des segments rigides parallèlement à la direction d'étirement. A part ce comportement général propre à toute la famille des PEEAs, nous avons constaté que les propriétés thermiques et mécaniques varient en fonction de différents groupements terminaux des segments rigides.

Le **chapitre 5** concerne l'étude de la structure polymère formée sous confinement spatial. Plus particulièrement, nous considérons le cas d'imprégnation des polymères dans des matrices nanoporeuses, ainsi que le cas de couches minces déposées sur des substrats nanostructurés (e.g., des substrats préparés par frottement de PTFE à haute température). Pour la famille des poly(di-*n*-alkylsiloxane)s présentant à la fois des phases cristal liquides et cristallines, nous montrons que, dans certaines conditions, l`ajout d'un groupement CH_2 dans la chaîne latérale peut changer l'angle entre la chaîne principale de poly(di-*n*-alkylsiloxane) et celle de PTFE de 90 degrés. Nous supposons que l'orientation des chaînes des poly(di-*n*-alkylsiloxane)s est fortement corrélée avec la nature de l'interaction épitaxiale, à savoir soit l'épitaxie moléculaire soit la grapho-épitaxie. Le phénomène de la grapho-épitaxie est également observé pour des matrices nano-poreuses imprégnées par des poly(di-*n*-alkylsiloxane)s et présentant une taille de pores de 35 nm. Il a été mis en évidence que dans des pores nanoscopiques les lamelles mésomorphes polymères croissent exclusivement parallèlement à l'axe des pores.

Une possibilité de confiner le processus de cristallisation a été explorée dans le **chapitre 6** pour un copolymère à bloc, le P2VP-PEO, ayant un bloc amorphe (P2VP) et un bloc cristallisable (PEO). L'introduction d'un ligand mésogène induit la séparation de phases dans ce système miscible suite à la complexation sélective avec les groupements pyridiniques de la chaîne de P2VP. Une transition d'une morphologie lamellaire vers une structure composée des lamelles et des cylindres coexistants, puis éventuellement vers une morphologie cylindrique est observée en fonction du degré de complexation. En combinant les techniques de GIWAXS/GISAXS et SFM, la structure hiérarchique des films minces a été étudiée. Dans ce cas, la structure présente trois niveaux d`organisation: l`échelle d`organisation du copolymère à bloc composée de domaines microphasiques (30 – 40 nm), celle de la phase cristal liquide du complexe (3 – 4 nm) et celle du bloc cristallisable (de 0.1 à 20 nm). Nous

avons démontré que la transformation du bloc P2VP d'un matériau complètement amorphe en une phase cristal liquide permet de confiner efficacement la cristallisation de PEO.